ASTROPHYSICAL APPLICATIONS OF GAMOW-TELLER STRENGTHS IN THE $A = 78 - 100$ REGION

By

Rachel Charlotte Taverner Titus

A DISSERTATION

Submitted to
Michigan State University
in partial fulfillment of the requirements
for the degree of

Physics - Doctor of Philosophy

2019

ABSTRACT

ASTROPHYSICAL APPLICATIONS OF GAMOW-TELLER STRENGTHS IN THE $A = 78 - 100$ REGION

By

Rachel Charlotte Taverner Titus

Electron-captures on medium-heavy nuclei play an important role in the late evolution of core-collapse supernovae. Sensitivity studies of simulations of these supernovae indicate a region of nuclei near the $N = 50$ shell closure, just above doubly magic ^{78}Ni, that have a significant effect on key characteristics of the evolution, such as the lepton fraction, electron fraction, entropy, stellar density and in-fall velocity. However, the vast majority of the nuclei in this region do not have dedicated weak-rate calculations; instead their rates are approximated via a method known for its overestimation of rates in heavy, neutron-rich nuclei. In order to guide the development of microphysical theoretical models, which yield Gamow-Teller strength distributions, from which more accurate electron-capture rates can be deduced, experimental data is needed to verify the validity of current models and to guide the development of improved models. Charge-exchange reactions at intermediate energies are an excellent tool with which to extract Gamow-Teller strength distributions model-independently, because of the well-established proportionality between the reaction cross section and the Gamow-Teller strength. In an attempt to obtain more accurate nuclear physics inputs for astrophysical simulations, an experimental campaign was performed at the National Superconducting Cyclotron Laboratory to study nuclei near the $N = 50$ shell closure. ^{86}Kr lies immediately adjacent to the region of interest for core-collapse supernovae; it was probed using the (t,^{3}He+γ) with the S800 magnetic spectrometer and the γ-detection array, GRETINA. The Gamow-Teller strength distribution, and the associated electron-

capture rates, were extracted from the experimental data, to compare with theoretical models and to determine the validity of the current nuclear physics inputs for core-collapse supernova simulations.

This thesis is dedicated to Guinevere and Daiba-Washi: you light up my life.

ACKNOWLEDGMENTS

The work presented in this thesis was made possible by many people, too many to properly name in this limited space. However, there are several people, without whom, I would have crashed and burned long ago.

First and foremost, I would like to thank Remco for all of the guidance and support for the past five years. Your endless patience and humor in the face of my constant questions and background subtraction agonies has been greatly appreciated.

To my committee members: Alex Brown, Sean Couch, Morten Hjorth-Jensen and Artemis Spyrou. Thank you for your helpful discussions and suggestions during our yearly meetings.

To all of the operators and staff of the NSCL. Thank you for all of the hard work making e16006 possible. Special thanks to Jorge Periera, for the assistance in setting up our krypton target system; Daniel Bazin, for being the S800 expert; Elaine Kwan, for all of the support during the beam time; and Peter Bender and Dirk Weisshaar, for explaining all things GRETINA-related.

To the postdocs of the Charge-Exchange Club: Shumpei, Ken, Juan and Bingshui. Thank you for showing me the ropes and allowing me to learn by following your example.

To my groupmates: Sam, Chris and Jaclyn. I could not have asked for better colleagues and I genuinely enjoyed learning alongside you. Thank you for all of the laughs.

To my mom and dad: Thank you for all of your support over the years. You always pushed me to follow my dreams, and gave me every opportunity for success.

And finally, to Ben: You have been with me every step of the way and I never would have made it this far without you. Thank you for your constant support and encouragement.

TABLE OF CONTENTS

LIST OF TABLES

LIST OF FIGURES

Chapter 1

Introduction

1.1 Motivation

Although they are separated by many orders of magnitude, astrophysics and nuclear physics are inextricably linked. Astrophysics is the study of phenomena on a cosmic scale, including the life cycle of stars and their catastrophic deaths. Nuclear physics, conversely, is concerned with nuclei on a microscopic scale; however, the interactions between these nuclei determine the observed characteristics of supernovae and other astronomical phenomena.

Nuclear physics combines theoretical and experimental work to draw conclusions about the structure of nuclei and their interactions with each other. Theoretical models are developed in conjunction with experimental data, and make predictions that are further tested by an array of experiments. Those theories that are supported by nuclear physics data are used to provide numerical inputs, such as reaction rates (the rate at which a reaction occurs, commonly dependent on the density and temperature of the stellar environment) [1, 2] or spectroscopic factors (which provide information about the occupancy of relevant orbitals, and its effect on the reaction rate of interest) [3], to astrophysical models, yielding predictions about the behavior of the universe on a much larger scale.

There are many types of reactions in the nuclear physics repertoire, all of which have their uses, depending on the topic and conditions of interest. To examine a reaction, a beam of

nuclei (projectile) is impinged on a target and the reaction products (ejectiles and residuals) are measured in detectors in order to evaluate the energy and trajectory of the particles. Selecting a reaction to study, in a particular energy regime, can yield information about the mass, shape, size or structure of a nucleus; such results increase the body of nuclear physics knowledge, but can also be applied to other, related fields. For example, transfer reactions transfer nucleons between the target and projectile, and are often used to examine the outer shell structure of nuclei, especially when performed at moderate energies [4]. In addition, these reactions are a popular tool for nuclear spectroscopy, the results of which have direct applications to astrophysics [5]. Another type of reaction, which provides both nuclear physics information and an astrophysical connection, is the charge-exchange reaction. Such reactions, performed at intermediate energies, are the main focus of this work.

Charge-exchange reactions are characterized by the exchange of a proton and a neutron between the target nucleus and the projectile nucleus, yielding a change in isospin ($\Delta T = 1$) [6]. Such reactions are able to excite a number of transitions, including Gamow-Teller and Fermi transitions (angular momentum transfer (ΔL)$= 0$), dipole transitions ($\Delta L = 1$) and quadrupole transitions ($\Delta L = 2$), and have been used as successful probes of nuclear structure for almost 40 years [7, 8]. Of particular interest to nuclear astrophysics are Gamow-Teller transitions, which are characterized by a spin transfer, an isospin transfer and zero angular momentum transfer. Such transitions are closely related to β-decay and electron-capture reactions, which are essential inputs to astrophysical simulations, because the initial and final nuclear states of these reactions are the same. Therefore, obtaining the strengths of these important astrophysical reactions is possible when the Gamow-Teller strength is known via charge-exchange reaction measurements.

Core-collapse supernova simulations make use of weak rates, including electron-capture

and β-decay rates, in order to determine the process by which a massive star collapses and explodes, ending its life [9]. β^--decay reactions occur when a nucleus emits an electron and an anti-neutrino, and converting the parent nucleus into a nucleus with the atomic number increased by 1. Electron-capture (or β^+-decay) reactions occur when the parent nucleus absorbs an electron (or emits a positron), and converting the parent nucleus into a nucleus with the atomic number reduced by 1. Many of the nuclei that participate in these processes have not been studied experimentally. Therefore, it falls to theoretical models to provide an alternative source for nuclear physics inputs. Because good experimental data for the heavy mass region of the chart of nuclides is sparse, theoretical models often extrapolate predictions from more well-studied regions, and lack the benchmarking necessary to ensure that the results provided are accurate for more exotic nuclei. Therefore, in an effort to study heavy, neutron-rich nuclei and their associated electron-capture rates in more depth, the nucleus ^{86}Kr ($Z = 36, N = 50$) was chosen for experimental study. This nucleus lies on the edge of a region of nuclei found to be important to the behavior of core-collapse supernovae (see chapter 2 for details) [9, 10, 11], and also lies on the $N = 50$ shell closure, which provides insight into the effect of orbital filling on electron-capture rates.

Experimentally, there are a number of charge-exchange probes that can be used, depending on the goal of the experiment. (p,n) and (n,p) reactions are indirect probes of β-decay and electron-capture reactions. There are also composite probes available, including (d,^{2}He), (^{3}He,t), (t,^{3}He) and heavy ion charge-exchange reactions, depending on the energy resolution needs of the experiment [12, 13]. The A1900 Fragment Separator [14], in conjunction with the Coupled Cyclotron Facility, at the National Superconducting Cyclotron Laboratory (NSCL) produces a secondary triton beam at intermediate energies, which is ideally suited to performing (t,^{3}He) experiments on a wide range of targets [15]. Utilizing both the capabilities

of the cyclotron facility and the S800 magnetic spectrometer [16], the conditions are excellent for measuring charge-exchange reactions on ^{86}Kr, and using those data to extract the desired Gamow-Teller strength. The gains from this experiment are two-fold: yielding information on the structure of the nucleus and providing the opportunity to calculate the associated electron-capture rates, which are of interest to the astrophysics community[17, 18, 19].

The goal of this and future experimental work will be to validate and benchmark current theoretical models that are used in astrophysical simulations. Determining which nuclear physics inputs are accurate, and where improvements can be made, will lead to the development of more robust models, facilitating a better understanding of galaxies, stellar evolution and the energetic phenomena that occur throughout the cosmos.

1.2 Organization

This work is divided into 5 chapters. Chapter 2 presents the astrophysical motivation for the ^{86}Kr charge-exchange experiment. Chapter 3 discusses charge-exchange reaction theory and calculation framework. Chapter 4 describes the experimental set-up and analysis process of the ^{86}Kr(t,^{3}He+γ) experiment. Chapter 5 re-visits the astrophysical motivation and examines the experimental results in the context of weak reaction rates. Finally, Chapter 6 discusses the significance of both the experimental and astrophysical work, and the outlook for future nuclear physics and astrophysics projects.

Chapter 2

Astrophysics

2.1 Core-Collapse Supernovae

2.1.1 Evolution

Core-collapse supernovae occur at the end of the life cycle of massive stars, typically in those between 8 and 40 solar masses. For the vast majority of a star's life, it is in the hydrogen burning stage, in which hydrogen nuclei in the core are fused, predominantly via the CNO cycle for massive stars, into helium [20]. After the hydrogen fuel is spent, helium burning begins, converting helium nuclei into carbon nuclei. For the most massive stars, further burning stages can be ignited, beginning with carbon burning, and then continuing through neon, oxygen and silicon burning phases. The internal structure of the star in the end is concentric layers of ashes from each of the burning stages surrounding an iron core [21]. Throughout these main burning stages, the gravitational pull of the star's mass, attempting to collapse it into a smaller volume, is balanced by the thermal pressure produced by the fusion of nuclei during the burning stages. Once the iron core of the star becomes degenerate, electron degeneracy pressure also contributes to the outward pressure, supporting the outer layers of the star.

The balance between the gravitational force pulling inward and radiation pressure pushing outward is maintained for the entirety of the star's lifetime. Although some stars experience

thermal pulsing [22], the general equilibrium is preserved such that the star neither collapses to a point, nor flies apart; the mass limit for this state is the Chandrasekhar mass [23], and is equal to approximately 1.4 solar masses. For massive stars, the iron core gains mass as the silicon burning phase progresses. As the mass of the core increases, the free electrons within the star exert additional outward pressure because they cannot be compressed further, as they are fermions and subject to the Pauli exclusion principle [24]. In order to remain non-degenerate, the electrons in the core become more and more energetic, eventually reaching relativistic velocities, allowing the progressively more massive iron core to be supported against collapse. However, once the mass of the core surpasses the Chandrasekhar mass, the fusion energy combined with the degeneracy pressure is no longer sufficient to balance the gravitational force inward [20, 24].

Matter from the outer layers of the star and the core press inward, causing the core of the star to begin to collapse [21]. The core of the star becomes extremely dense as the collapse continues, reaching the point at which further compression is not possible in its current composition, as this would cause electrons to occupy the same energy states, and would violate the Pauli exclusion principle. Instead the free electrons fuse with protons or capture onto heavy nuclei, reducing the lepton fraction in the core. Because free electrons are being removed from the nuclear matter, this causes a decrease in the degeneracy pressure, further exacerbating the imbalance with the inward gravitational force. Additionally, when an electron captures onto a nucleus, a neutrino is released; these neutrinos are able to escape the star easily, and carry away energy that was otherwise working against the gravitational pressure inward [21]. Hence, as the energy streams away with the neutrinos, the outward pressure is further decreased, leading to less resistance to gravitation collapse [20]. Then, as the rate of collapse increases, the rate at which electrons are captured increases, releasing

more neutrinos and causing more energy loss in the core of the star.

The cycle of electron capture and neutrino energy loss, along with the energy loss associated with the photodisintegration of iron nuclei, leads to a run-away process, causing the collapse of the star to happen faster and faster until the density of the matter reaches 10^{12} g/cm^3. At that point, the opacity of the matter increases to such a point that neutrinos can no longer escape from the center of the star and are trapped [21, 25]. After neutrino trapping, the star continues to collapse until the density reaches approximately 10^{14} g/cm^3, at which point the nuclear matter of the inner core, which is now classified as a proto-neutron star, is saturated and cannot be compressed further. The outer layers of the core decelerate and bounce off of the inner core, sending a shock wave moving outward through the layers of the star.

The general mechanics of the core-collapse are known [1, 24, 26], however, understanding the explosion mechanism, which ultimately destroys the star, is a work in progress. There are a number of theories available [21, 27, 28], but the exact process and details are still being determined through simulations and observations. For this work, the main period of interest is during the late stages of core-collapse, from the beginning of the period of deleptonization until core bounce. It is then that electron-capture rates play a significant role in the hydrodynamic evolution of the supernova, a facet about which nuclear experiments can provide more information in order to improve the understanding of the mechanisms at work.

Core-collapse supernovae, in addition to releasing energy in the form of visible light, also produce large quantities of neutrinos, as mentioned previously. Additionally, these events are predicted to be the origin of gravitational waves that can be measured [29, 30]. Through all of these signals, core-collapse supernovae appear to be excellent candidates for multi-messenger

studies, coordinating the observation and interpretation of various messenger signals from a single astrophysical event [31]. By combining the information obtained from a variety of sources, it is possible to gain a better understanding of these, and other, astrophysical processes. However, accurate and detailed knowledge of nuclear physics processes is needed in order to interpret the astrophysical observations and to draw robust conclusions that can be applied to our understanding of the universe as a whole.

2.1.2 Electron-Capture Rates

Electron-captures on nuclei play an important role in astrophysical phenomena, such as during carbon burning and later stages in massive stars [32, 33], especially the growth of the iron core [34, 35] and the subsequent collapse of the iron core leading to a core-collapse supernova [1, 9, 21, 26, 30, 36], thermonuclear supernovae [37, 38, 39, 40], neutron stars and their crusts, [41, 42] and neutron-star mergers [43]. Because of their diverse applications, it is important to obtain accurate nuclear-physics inputs that can be used in astrophysical simulations, including sets of electron-capture and β-decay rates across a range of stellar temperatures and densities for a large number of nuclei.

Electron-capture rates depend sensitively on the Gamow-Teller transition ($\Delta L = 0$, $\Delta S = 1$, $\Delta J = 1$) strength distribution in the β^+ direction [17, 44, 45, 46, 47]:

$$\lambda_{EC} = \ln(2) \sum_{ij} f_{ij}(T, \rho, U_F) B(GT)_{ij}. \tag{2.1}$$

The rate is obtained by summing over the Gamow-Teller strength distribution, $B(GT)$, and is weighted by the phase-space factor, $f(T, \rho, U_F)$, which depends on the stellar density, ρ, temperature, T, and chemical potential, U_F. β^+ and electron-capture decay experiments

yield the Gamow-Teller strength distributions necessary to calculate electron-capture rates [17, 48, 49, 50]. However, these experiments are energetically limited to states within a specific Q-value window, if energetically possible at all. On the neutron-rich side of the valley of stability, decay proceeds in the β^- direction and the Gamow-Teller transitions required to calculate electron-capture rates cannot be measured at all, unless they are ground-state to ground-state transitions.

Charge-exchange experiments, which provide an indirect method for the extraction of Gamow-Teller strengths, are not limited by this Q-value window, thus yielding information about transitions to higher excitation energies. Because of the known proportionality between Gamow-Teller strength and charge-exchange reaction cross section [12, 51, 52], Gamow-Teller strengths can be extracted model-independently. Therefore, charge-exchange experiments in the β^+ direction have become an important tool for extracting Gamow-Teller strengths of relevance for the determination of astrophysical electron-capture rates.

Unfortunately, it is not possible to measure Gamow-Teller strength distributions on all nuclei that play a role in the aforementioned astrophysical phenomena. In addition, in high-temperature stellar environments, low-lying states in parent nuclei can be thermally populated, and electron-captures can take place on these excited states [53]. Moreover, at high temperatures, shell orbits that would be Pauli-blocked at $T = 0$, can become partially unblocked [54], which changes the Gamow-Teller strength distribution. Because these effects are difficult to study in the laboratory, electron-capture rate calculations and astrophysical simulations can use rates determined on the basis of experiment, where available and appropriate, but in general must rely on theoretical estimates. An important role of the experiments is then to guide and benchmark the theoretical calculations and to provide measures for uncertainties in the theories.

The earliest set of theoretical weak-rates, based on a single-particle estimate, were provided by Fuller, Fowler and Newman (FFN) [44, 45, 46, 47]. With the advent of increased computational power, electron-capture rate sets based on shell-model calculations became feasible, starting with nuclei in the *sd*-shell ($N, Z = 8-20$; see section 3.1.1 for an explanation of the shell structure) [55]; these rate calculations were recently updated [33]. Weak-rate sets for nuclei in the pf-shell ($N, Z = 20 - 40$) were generated [39, 53, 56] based on the KB3G interaction [57] and, recently, the GXPF1 family of interactions [58, 59, 60]. For heavier nuclei, shell-model calculations are computationally challenging, although calculations with severely constrained model spaces, such as the ^{78}Ni or ^{88}Sr core, used in reference [61], have been used to estimate weak rates for astrophysical purposes. Consequently, other theoretical techniques, such as QRPA [62, 63, 64, 65, 66] or shell-model Monte-Carlo [67, 68], are used. Such calculations cannot reproduce the details of the Gamow-Teller strength distributions as well as shell-model calculations can; the relationship between stellar density and the importance of the details of the Gamow-Teller strength distribution will be discussed further in section 2.2.3.

In order to consolidate all available tables of weak rates for use in astrophysical simulations, a weak-rate library was developed by Sullivan *et al* [9]. As shown in figure 2.1, weak rates based on microscopic calculations of varying origin cover low- and medium-mass nuclei primarily around the valley of stability. For the vast majority of nuclei, especially those far from stability, an approximate method is used to generate these electron-capture rates for use in simulations [1, 2]. The weak rate library and this approximate method will be discussed in section 2.2.1.

Sensitivity studies, in which electron-capture rates are varied within uncertainties, are helpful for gaining a better understanding of the impact of these rates on the evolution of the

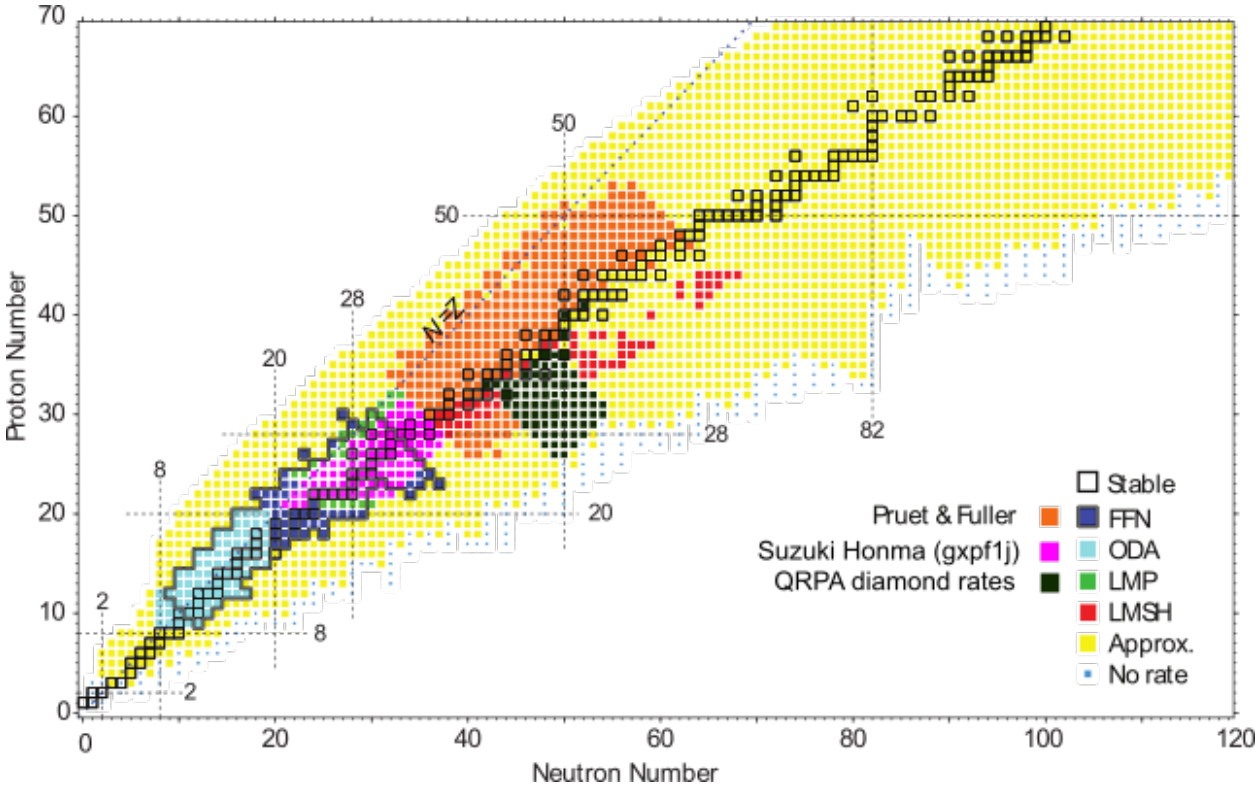

Figure 2.1: Nuclear species currently included in the weak-rate library. The original tables included in the library by Sullivan *et al.* were FFN [45], ODA [55], LMP [69, 56] and LMSH [26, 54]. The Pruet and Fuller tables [70], the QRPA diamond rate table, and the Suzuki table [33], as an update to the Oda rates, were added to the library most recently. This figure was adapted from [10].

late stages of stellar core-collapse [9, 11, 33]. Additionally, these studies assist in identifying the rates that have a significant impact on the astrophysical model. In the work by Sullivan *et al.*, it was shown that nuclei in the upper pf- and pfg/sdg-shells, particularly in the region around $N = 50$ at and above ^{78}Ni (see figure 2.2), have the largest impact on the change in electron density (Y_e) and, thus, on the dynamical evolution of the collapse. This region, marked in dark green in figure 2.1, was denoted the *high-sensitivity region* or the *high-sensitivity diamond*, and it is upon this group of nuclei that effort is focused in order to demonstrate the importance of constraining the electron-capture rates in this region.

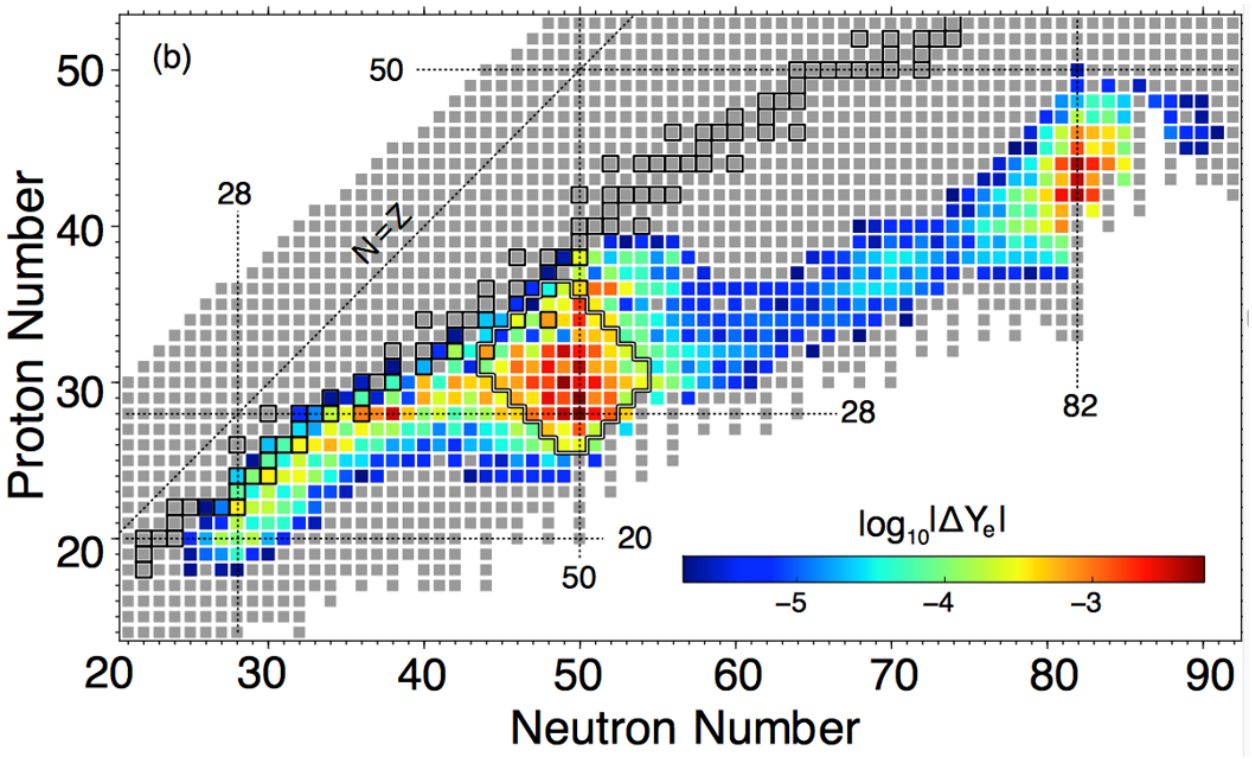

Figure 2.2: Contributions to the change in electron fraction (Y_e), as a function of neutron and proton number, in late stages of stellar core-collapse, based on the work by Sullivan *et al.* Nuclei in this *high-sensitivity region* around $N = 50$ (diamond outlined region), at and above ^{78}Ni, and $N = 82$ region, are particularly important contributors to the change in Y_e and strongly affect the dynamical evolution of the supernova. This figure was taken from [9].

2.2 Weak-Rate Library

2.2.1 Approximate Method

The weak-rate library [9, 71], mentioned previously, includes several tables of electron-capture and β-decay rates (see figure 2.1) over a large density and temperature grid. It can be used independently for calculations or used in conjunction with the neutrino-interaction library, NuLib [72]. NuLib uses the electron-capture rates in the library to calculate neutrino/antineutrino charged-current absorption opacities for use in astrophysical simulations. The simulations of core-collapse supernovae described here are performed using the general

relativistic, spherically-symmetric stellar collapse code, GR1D [72, 73], but the library has also been used in two-dimensional simulations of core-collapse supernovae [30].

Many of the neutron-rich nuclei in the high-sensitivity region do not yet have an electron-capture rate based on a microscopic model calculation included in the weak-rate library and, consequently, an approximate method is used to calculate the electron-capture rate at the appropriate density and temperature. The approximate electron-capture rate is given by [47, 69]:

$$\lambda_{EC} = \frac{\ln(2) \cdot B}{K} \left(\frac{T}{m_e c^2} \right)^5 \left[F_4(\eta) - 2\chi F_3(\eta) + \chi^2 F_2(\eta) \right], \tag{2.2}$$

where m_e is the electron mass, $K = 6146$ s, F_k are Fermi integrals of rank k and degeneracy η, $\chi = (Q - \Delta E)/T$, $\eta = \chi + \mu_e/T$, and T and μ_e are the temperature and electron chemical potential, respectively. B, the effective Gamow-Teller transition strength, is fixed for all isotopes to 4.6. ΔE, the effective excitation energy, is fixed for all isotopes to 2.5 MeV. These values were determined in a fit to shell-model calculations for nuclei in the pf-shell [1] relatively close to the valley of stability. There is also a new version of this approximate method implemented in the library, which improves the accuracy of the rates by adjusting the effective excitation energy based on neutron and proton numbers [2] (while leaving the effective transition strength fixed).

2.2.2 Comparison to Theoretical Calculations

For neutron-rich nuclei, including those in the high-sensitivity region, the use of the approximation with parameters fit to microscopic calculations for nuclei close to stability constitutes an extrapolation to a region of the chart of nuclei in which different shells play a role. Hence, the uncertainties when applying the approximation can be large, as first detailed in refer-

ence [68], in which occupation numbers were estimated based on predictions in shell-model Monte-Carlo calculations. At and above the $N = 50$ shell closure, Gamow-Teller transitions are associated with transitions in which the added neutron occupies an orbital above $\nu g_{9/2}$ [74]. Therefore, the strongest transition is $\pi g_{9/2} \rightarrow \nu g_{7/2}$ [75, 76]; this conclusion will be discussed in greater detail in section 3.1.1. If protons are present in the $\pi g_{9/2}$ orbital, the Gamow-Teller transition strength is significant; however, with increasing neutron number beyond $N = 50$, the $\nu g_{7/2}$ orbital becomes Pauli-blocked and the transition strength decreases. Similarly, as the nucleus becomes less proton-rich and the occupancy of $\pi g_{9/2}$ is lowered, the transition strength will decrease. For $N < 50$, $\pi g_{9/2} \rightarrow \nu g_{9/2}$ transitions also contribute to the Gamow-Teller transition strength.

In order to examine the effect of filling these orbitals on the Gamow-Teller strength, it is beneficial to employ a simple model, using the occupancies of the $\pi g_{9/2}$, $\nu g_{7/2}$ and $\nu g_{9/2}$ orbitals. Following the work of Macfarlane [77], the Gamow-Teller strength in the β^+ direction can be estimated using:

$$S^+ = 3 \sum_{nljj'} \left(C_{nl}^{jj'}\right)^2 \left(1 - n_{nlj}^N\right) n_{nlj'}^P, \tag{2.3}$$

where n_{nlj}^N is the average occupancy of the initial neutron orbital, $n_{nlj'}^P$ is the average occupancy of the final proton orbital, and

$$C_{nl}^{jj'} = [2(2j+1)(2j'+1)]^{1/2} W(l\tfrac{1}{2}j1; j'\tfrac{1}{2}), \tag{2.4}$$

in which j is the total orbital angular momentum quantum number for the initial state, j' is the total orbital angular momentum for the final state and W is the Racah W-coefficient.

Here, the jj44pna interaction [78] is used in the SNE model space in which protons can populate the $0f_{5/2}$, $1p_{3/2}$, $1p_{1/2}$, and $0g_{9/2}$ orbitals, and neutrons can populate the $0g_{7/2}$, $1d_{5/2}$, $1d_{3/2}$, $2s_{1/2}$ and $0h_{11/2}$ orbitals, to estimate the filling of the neutron and proton orbitals.

Figure 2.3 shows that the Gamow-Teller strength increases with proton number along the $N = 50$ line (blue triangles). For $Z \leq 30$ ($A \leq 80$), protons do not populate the $\pi g_{9/2}$ orbital and Gamow-Teller transitions are completely blocked. The opposite trend is seen when increasing the neutron number (shown in red squares in figure 2.3 for the case of krypton ($Z = 36$) isotopes). Below $N = 50$ ($A = 86$), both $\pi g_{9/2} \rightarrow \nu g_{7/2}$ and $\pi g_{9/2} \rightarrow \nu g_{9/2}$ transitions can contribute. Above $N = 50$ ($A = 86$), $\pi g_{9/2} \rightarrow \nu g_{9/2}$ transitions are completely blocked, and $\pi g_{9/2} \rightarrow \nu g_{7/2}$ transitions increasingly so. Hence, the Gamow-Teller strength decreases, until it is completely blocked at $N = 58$ ($A = 94$) when the neutrons completely fill the $g_{7/2}$ orbital.

Figure 2.3 also shows the strength used in the approximate method [1, 2], which is higher than the estimates based on the orbital fillings in this region of the chart of nuclides by at least an order of magnitude. It is important to note that at high stellar temperatures, thermally-driven Pauli-unblocking effects will increase the electron-capture rates beyond the value calculated at $T = 0$. For nuclei in which the Pauli-blocking effects are strong, the unblocking can lead to a significant increase of the electron-capture rates [1, 54, 65]. However, for nuclei in which the Pauli-blocking is incomplete, the effects of the increased temperatures and additional unblocking are relatively small [54], which is the likely scenario for nuclei in the high-sensitivity region.

Ultimately, it is preferable to generate electron-capture rates using microscopic calculations based on realistic strength distributions that are benchmarked against data. In the

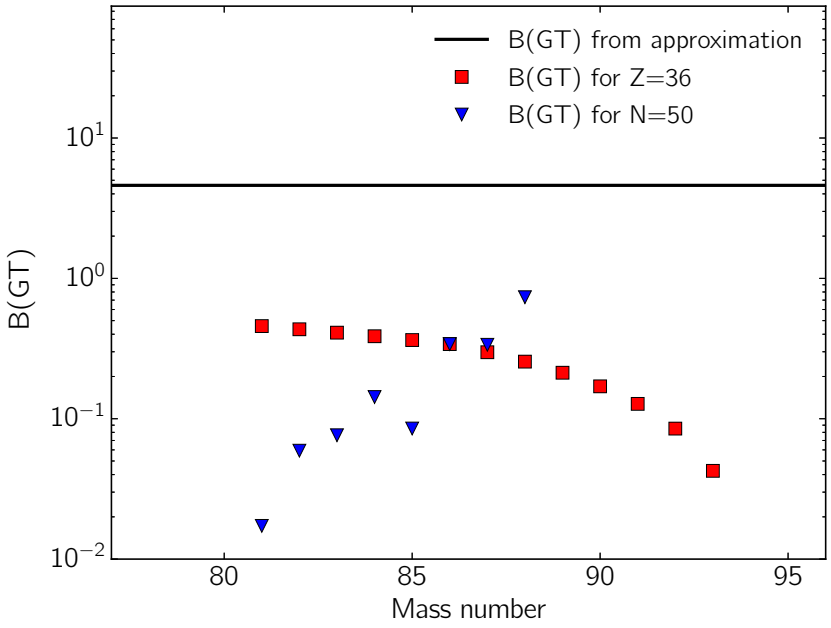

Figure 2.3: A comparison of Gamow-Teller strengths calculated following equation (2.3) and (2.4) [77] for nuclei on the $N = 50$ line (blue triangles), for nuclei on the $Z = 38$ line (red squares) and for the approximate method, which uses a fixed value of $B(GT) = 4.6$ (black line). This figure was taken from [10].

pf-shell, rates calculated by using shell-model results are the most accurate based on a comparison with charge-exchange data [17]. Although shell-model calculations near $N = 50$ are a challenge, initial calculations were performed using NUSHELLX [79] using the jj44pna interaction [78]; an example of such a calculation, for the case of ^{86}Kr, is shown in figure 2.4. The excitation energy of the first transition in the shell-model calculation was chosen to match the first known 1^+ state in ^{86}Br (at 2.45 MeV), because the energy of the 1^- ground state in ^{86}Br cannot be calculated within the chosen model space.

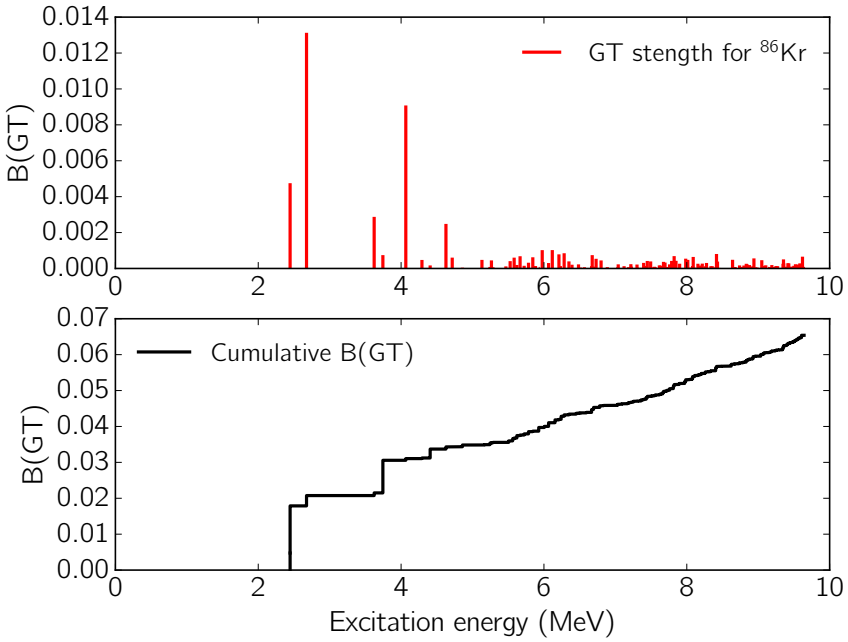

Figure 2.4: Gamow-Teller strength distribution for ^{86}Kr, calculated using the jj44pna interaction [78] in the SNE model space [76, 75]. The cumulative Gamow-Teller strength calculated from the shell-model, shown in the bottom panel, is comparable to the value obtained from occupancy approximation of the Gamow-Teller strength, shown in figure 2.3. Therefore, this simple model is reasonable estimate of the total Gamow-Teller strength around the $N = 50$ shell closure.

2.2.3 Contributions to Electron-Capture Rates

It is found that the shell-occupancy approximation, discussed above, estimates a similar total strength to the shell-model calculation for ^{86}Kr, indicating that the $\nu g_{7/2}$ and $\pi g_{9/2}$ orbitals are dominant in the shell-model calculations as well. However, in the shell-model calculations, about half of the total strength is distributed over many states at higher excitation energies, which results in a reduction of the electron-capture rates compared to the assumption that all strength is contained in a single state at 2.5 MeV, as in the rate approximation (equation 2.2). This reduction is in addition to that which is caused by the overestimated total transition strength, due to the lack of Pauli-blocking included in the ap-

proximation model. Finally, it is well-known that Gamow-Teller strengths calculated in the shell-model must be quenched by factors of 0.5-0.6 to account for effects not included in the calculation [80, 81, 82, 83], which reduce the total strengths and, thus, the electron-capture rates further. The quenching applied to the strength takes the form of a hindrance factor, $1/h$, which accounts for the mixing of two-particle two-hole states with oscillator energies of $2\hbar\omega$ and greater.

The dependence of the electron-capture rate on stellar density is explained by the phase space energy equation [17, 44]:

$$U_F = 0.511 \times \left[\left(1.018 \big(\rho_6 Y_e\big)^{2/3} + 1 \right)^{1/2} - 1 \right], \tag{2.5}$$

where ρ_6 is the stellar density divided by 10^6 gm/cm^3 and Y_e is the electron fraction. The Fermi energy, ϵ_F, is related to the phase space energy by the following expression: $\epsilon_F = U_F + m_e c^2$. For reactions in which the Fermi energy far exceeds the Q-value of the reaction, electron-capture rates will be relatively constant with respect to changes in stellar density. However, when the Q-value of the reaction is close in magnitude to the Fermi energy, as is the case for ^{86}Kr, with $Q = -7.607$ MeV and $U_F = 10.6$ MeV at $\rho Y_e = 10^6$ g/cm^3, the electron-capture rates are sensitive to changes in the stellar density, ρ, and electron fraction, Y_e. This behavior occurs because, as the density increases, more excited states in the nucleus become available to contribute to the overall electron-capture rate.

By examining the two components of the electron-capture calculation (strength distribution and phase space factor), it is possible to visualize the relationship between the Gamow-Teller strength distribution and the electron-capture rates. Shown in the top plot of figure 2.5 is the phase space factor, f, as a function of Q-value and normalized to the phase space

factor at $Q = 0$ MeV, for a variety of stellar densities. This factor, as defined in equation 2.1, weights each of the Gamow-Teller states in the sum that is used to calculate the electron-capture rate. For relatively low stellar densities ($\rho < 10^{10}$ g/cm^3), the phase space factor drops off quickly as a function of Q-value, meaning that only the lowest-lying Gamow-Teller states will contribute significantly to the electron-capture rate calculations. However, as the stellar density increases to 10^{11} g/cm^3 (red line) or 10^{12} g/cm^3 (green line), the phase space curve decreases less sharply, indicating that Gamow-Teller states with higher excitation energies begin to contribute more strongly to the electron-capture rate.

The center plot of figure 2.5 shows the Gamow-Teller strength distribution for ^{86}Kr as obtained from the QRPA calculation that will be discussed in section 5.1 [84]. Now plotted as a function of Q-value, it is clear that the majority of the strength sits at or above a Q-value of 10 MeV. For the other nuclei in the high-sensitivity region, the Gamow-Teller strength distributions have a similar form. Finally, the bottom plot in figure 2.5 illustrates the relationship between the electron-capture rates, the Gamow-Teller strength distribution and the stellar density. The electron-capture rates were calculated by multiplying the Gamow-Teller strength by the phase space factor, following equation 2.1. Then, the running sum of electron-capture rates, normalized to the total rate, as a function of Q-value, was plotted, illustrating the relative contribution of each Gamow-Teller transition to the total, for each of the stellar densities.

For lower stellar densities (black and blue curves), the first peak in the strength distribution contributes significantly to the overall electron-capture rate, while all of the successive states contribute very little. However, with increasing density, as in the cases of 10^{11} g/cm^3 (red line) and 10^{12} g/cm^3 (green line), the higher-lying states begin to contribute more to the overall electron-capture rate. Because ^{86}Kr has a large, negative Q-value for electron-capture

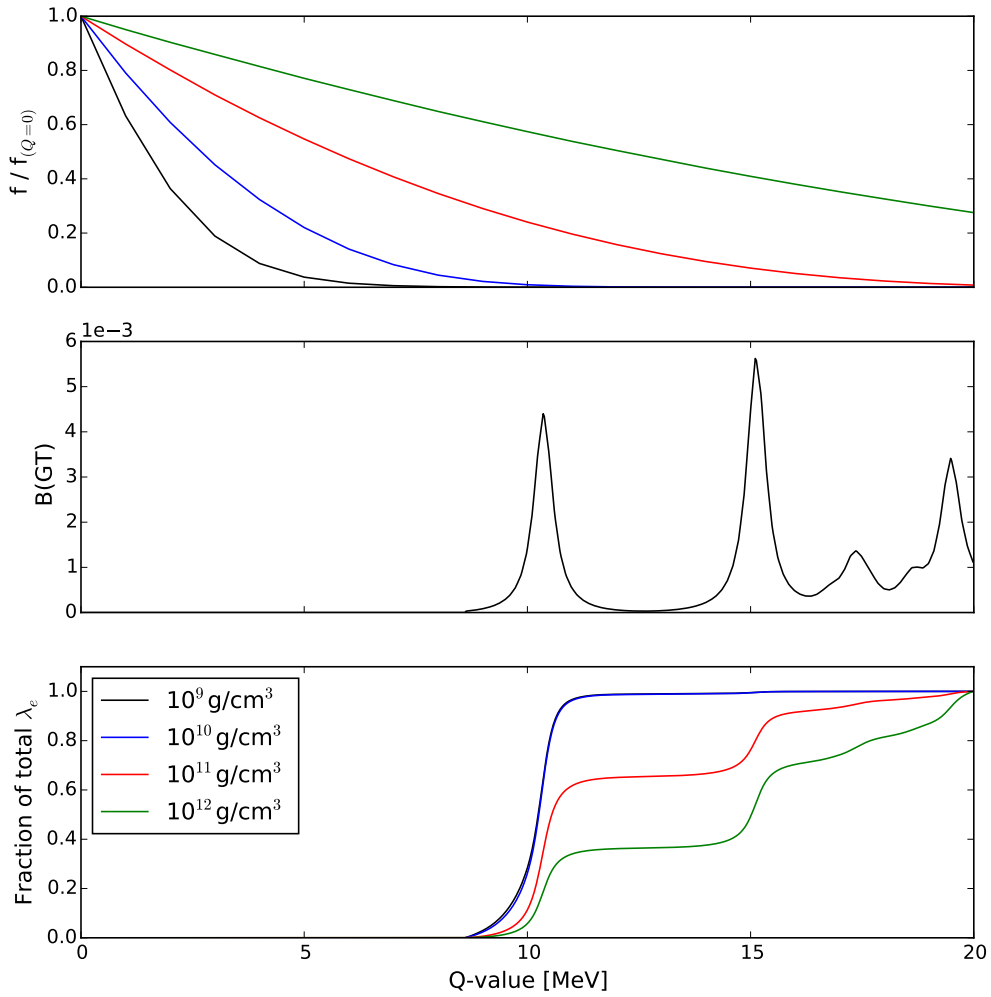

Figure 2.5: (top) Phase-space factors as a function of electron-capture Q-value at stellar electron densities. (middle) Plot of a sample Gamow-Teller strength distribution for ^{86}Kr. (bottom) The resulting electron-capture rates obtained by multiplying the top and middle curves. At low densities, the electron-capture rate calculation is extremely sensitive to the low-lying Gamow-Teller states (black line), but as the density increases, the total strength becomes more important to the calculation, as opposed to the details of the strength distribution (green line).

reactions, the details of the strength distribution play an important role in the calculation of electron-capture rates at high densities. Such a conclusion differs from previous assumptions that, at high stellar densities, it is only the cumulative Gamow-Teller strength that affects

the electron-capture rate [17]. It is clear from this result that the electron-capture rates for nuclei with large, negative Q-values are predominantly dependent on the details of the Gamow-Teller strength distribution.

When the densities are in excess of 10^{11} g/cm^3, forbidden transitions begin to contribute to the rate as well [68, 69, 85], but they are not explicitly included in this work. At densities of 10^{12} g/cm^3, the electron-capture rate could double due to contributions from forbidden transitions [68]. Although charge-exchange experiments provide information on the strength distributions for forbidden transitions, a proportional relationship between forbidden transition strengths and charge-exchange cross sections has not been established, making it difficult to extract strengths and to quantify the uncertainties in the associated electron-capture rates.

For some of the nuclei in the high-sensitivity region, electron-capture rates have been estimated by considering thermally-driven Pauli-unblocking effects in a hybrid shell-model RPA calculation [26, 54]. These rates are included in the weak-rate library in the form of the LMSH table in figure 2.1. A comparison between the LMSH rates and the rates based on approximate method for nuclei in the high-sensitivity region is shown in figure 2.6. Because these rate calculations do consider the effects of Pauli-blocking and have more accurate estimates for the Gamow-Teller strengths, the electron-capture rates are generally less than the estimates based on the approximation, with deviations between the two methods reaching two orders of magnitude in some cases. Still, this is not uniformly the case, because the electron-capture rate Q-values used in the two methods can be different and may change the estimated rates significantly. Clearly, guidance from charge-exchange experiments, similar to the case for nuclei in the pf-shell, is required to constrain the rates, to estimate the uncertainties in the theory, and to provide data on the basis of which theoretical estimates can be improved.

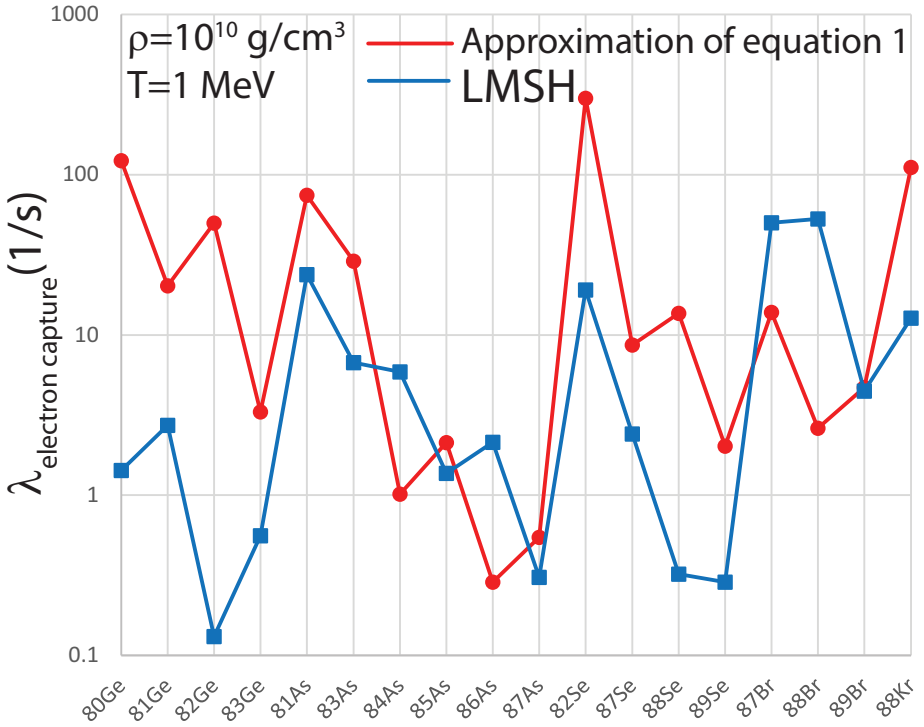

Figure 2.6: Comparison between electron-capture rates estimated in a hybrid shell-model RPA calculation (LMSH) [26, 54] and based on the approximation of equation (2.2) for nuclei in the high-sensitivity region near $N = 50$. A density of 10^{10} g/cm^3 and a temperature of 1 MeV was used in the rate calculations. This figure was taken from [10].

2.3 Study of the High-Sensitivity Region

As illustrated in figure 2.2, there exists a cluster of nuclei around the $N = 50$ shell closure at and above ^{78}Ni that has a large impact on the change in electron fraction in the core-collapse supernova simulations. In order to determine the sensitivity of the simulation to this region in more detail, a set of 74 nuclei was chosen, covering both sides of the $N = 50$ line from the valley of stability to the neutron drip line. In this sensitivity study, the electron-capture rates were systematically scaled in two parts. The first was the case in which the rates for all nuclei were scaled; the second was the case in which which only the rates for nuclei in the high-sensitivity region were scaled. The scaling factors (x10, x1, x0.1, x0.01) were chosen

to represent the uncertainty in the electron-capture rates based on the comparison between different models, as discussed above, and the models and experimental data for nuclei in the pf-shell.

The simulation framework used for the sensitivity study is similar to the work performed by Sullivan *et al.* [9]. The open-source spherically symmetric, general-relativistic neutrino-transport and hydrodynamics code, GR1D, was used to simulate the late stages of core-collapse [72, 73]. In these simulations, all of the tables included in the weak-rate library, except for the Suzuki-Honma and QRPA rate tables, were used, with the hope that a larger set of nuclei would have microphysically-accurate rates available. The electron-capture rates from the library were integrated into NuLib [72], the open-source neutrino-interaction library discussed in section 2.2. A well-known 15 solar-mass, solar-metallicity progenitor (s15WW95) [86] was used in the simulations with the SFHo equation of state and nuclear statistical equilibrium distributions from reference [87]. It has been shown previously that variations in the electron-capture rates play a more important role in the simulation than variations in the progenitor or equation of state [9] therefore, only the electron-capture rates that were input to the simulations were changed in the sensitivity studies discussed here.

A comparison of the lepton fraction (Y_l) as a function of central density (ρ_c) for simulations in which the electron-capture rates are scaled by various factors is shown in figure 2.7. The black solid line represents the base calculation, in which the electron-capture rates have not been scaled. At low densities ($\rho_c \sim 10^{10}\mathrm{g/cm}^3$), electron-captures are responsible for the deleptonization of the matter in the core of the star. The opacity of the matter is low, allowing electron neutrinos to escape the star freely, causing the lepton fraction to decrease. When the central density reaches $\rho_c \approx 2 \times 10^{12}$ g/cm^3, the lepton fraction saturates (at a value of $Y_l = 0.292$ in the base calculation) as neutrino trapping prevents further deleptonization. If

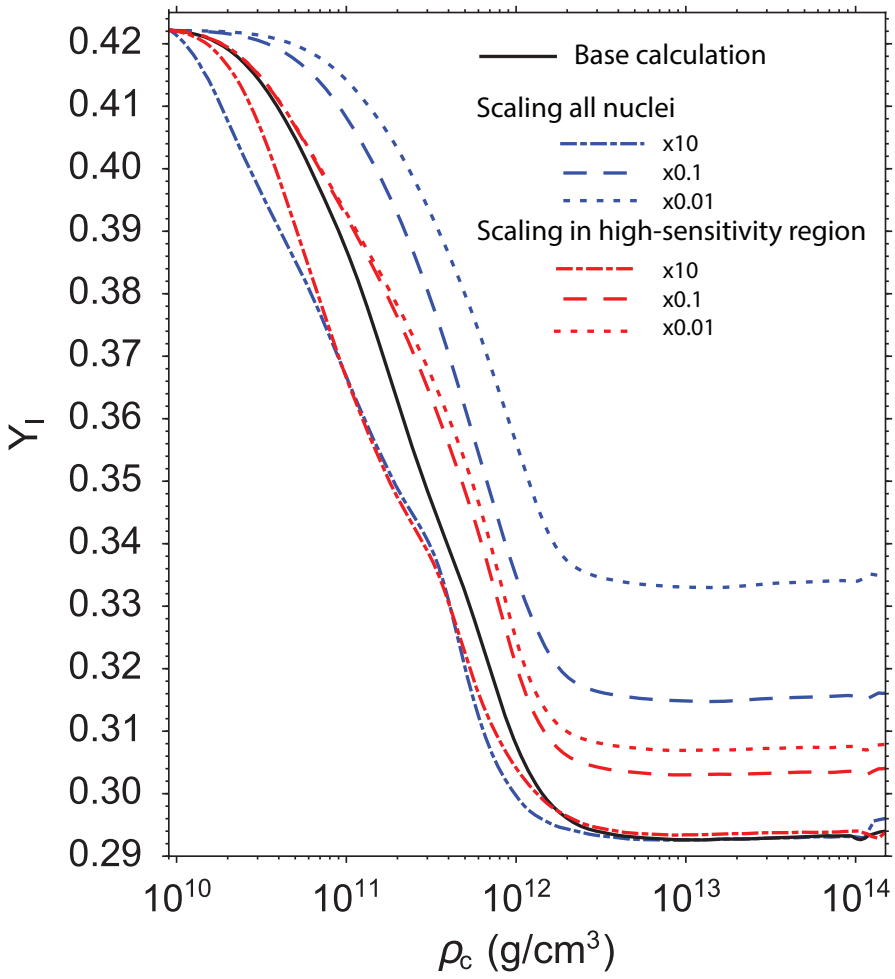

Figure 2.7: Diagrams of lepton fraction versus central density during the core-collapse process for different scalings of electron-capture rates for all nuclei (in red) and for nuclei in the high-sensitivity region (in blue). Scaling factors of 10, 0.1 and 0.01 are applied. The base simulation in which no rates are scaled is represented by the black line. This figure was taken from [10].

the electron-capture rates in the library are increased (dashed-dotted lines in figure 2.7), simulating the situation in which the electron-capture rates in the library are underestimated, a similar or slightly higher final lepton fraction is attained. This is because the opacity related to electron-neutrino captures on heavy nuclei becomes stronger than opacities related to the electron-neutrino scattering, reducing the window for deleptonization [9].

For reasons discussed in previous sections, the scenario in which the electron-capture

rates in the library are overestimated is more likely. In the simulations in which the electron-capture rates are reduced (dashed (x0.1) and dotted (x0.01) in figure 2.7) the final lepton fraction significantly increases compared to the base calculation. The blue curves in figure 2.7 represent scenarios in which the electron-capture rates for all nuclei in the library are scaled, whereas the red curves denote the results in which only the 74 nuclei in the high-sensitivity region are scaled. Scaling all electron-capture rates in the simulation by a factor of 0.1 (blue dashed line) produces a final lepton fraction of $\sim$0.314, an increase of 7.5% compared to the base simulation. By scaling the electron-capture rates only in the high-sensitivity region (red dashed line), the final lepton fraction is $\sim$0.303, a 3.8% increase from the base simulation.

The relatively strong effect of scaling the electron-capture rates in the high-sensitivity region is also apparent in the simulation results for the electron fraction, entropy, stellar density and in-fall velocity at core bounce, as a function of enclosed mass, as shown in figure 2.8. Here, the definition of t_{bounce} by the authors of GR1D, namely that it occurs when the entropy reaches a value of 3.0 [72], is followed. The variation in simulated characteristics of these parameters, resulting from applying scaling factors of 10, 1, 0.1, and 0.01 to the electron-capture rates on the nuclei in the high-sensitivity region only is indicated by the red bands. The variation by scaling the electron-capture rates on all nuclei is indicated by the black lines. As in the case of the lepton fraction, the effect of only changing the rates for the nuclei in the high-sensitivity region accounts for about half of the changes observed when scaling the electron-capture rates on all nuclei. It is likely that the nuclei in the pf-shell and nuclei $N = 82$ region account for much of the additional variation observed for the simulation in which the rates of all nuclei are scaled. Of the 8140 nuclei included in the core-collapse supernova simulations, fewer than half play a role [88] and, of these, the 74 nuclei in the high-sensitivity region are most important during the core-collapse and early post-bounce

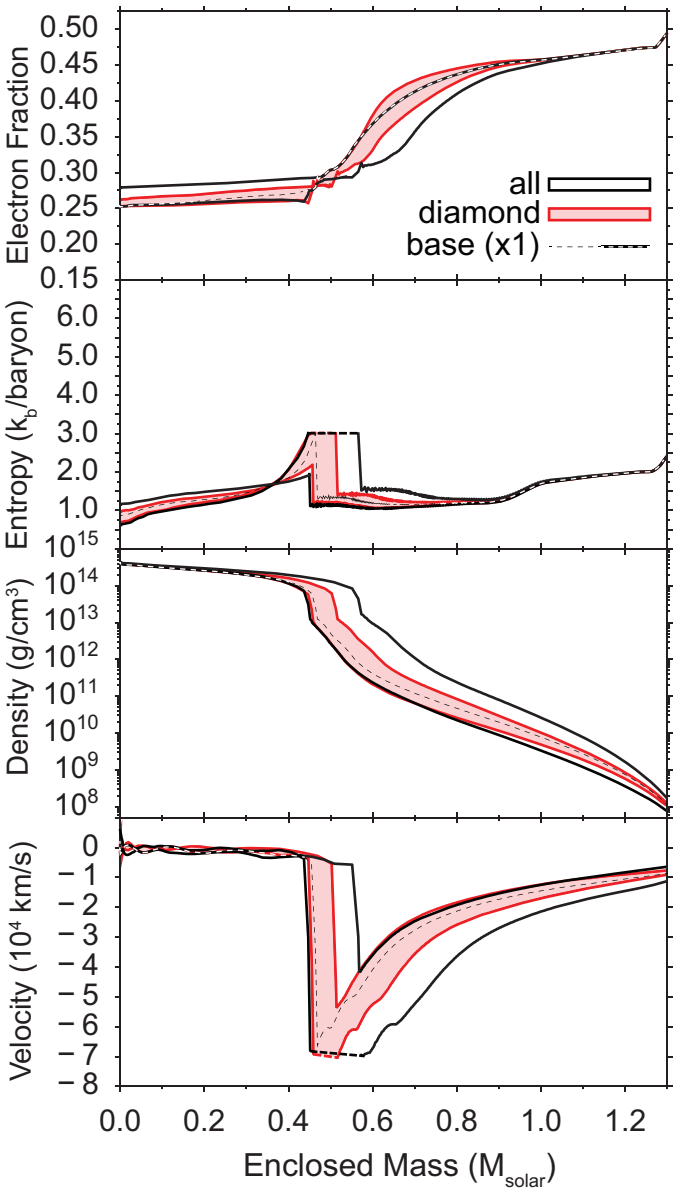

Figure 2.8: Electron fraction, entropy, density and matter velocity at $t = t_{\text{bounce}}$ (defined when the entropy reaches 3.0) for two sets of simulations. The bands indicate the range of values obtained when the electron-capture rates are scaled in the high-sensitivity region (red) or across the entire chart of nuclides (black). This figure was taken from [10].

phases.

It is important to note that figure 2.2 highlights two groups of nuclei that contribute significantly to the change in electron fraction: those in the regions around $N = 50$ and $N = 82$. While this is true, electron-captures on the nuclei near $N = 50$ are much more important

for the evolution of core-collapse supernovae. Simulations indicate that the nuclei at the $N = 82$ shell closure do not contribute significantly until just before core-bounce when the density is extremely high and neutrino trapping has already occurred. Therefore, it can be concluded that experimental and theoretical studies of Gamow-Teller strength distributions in the high-sensitivity region around $N = 50$ are the most important objective for constraining the weak-interaction inputs for simulations and for understanding the evolution of core-collapse supernovae.

2.4 Sensitivity Study Conclusions

From the simulations of core-collapse supernovae performed here and in previous work, it is clear that accurate electron-capture rates are important for understanding the dynamical evolution of these cataclysmic events. Electron-captures on the 74 nuclei in the high-sensitivity region around $N = 50$ just above doubly-magic ^{78}Ni affect key characteristics, such as the lepton fraction, electron fraction, entropy, stellar density, and in-fall velocity, by as much as the other thousands of isotopes included in the simulation combined.

The electron-capture rates on nuclei in the high-sensitivity region that are currently used in the weak-rate library are likely too high because the approximate method used to estimate such rates is based on microscopically calculated rates for nuclei close to stability, where Pauli-blocking effects are much weaker. Although Pauli-unblocking occurs at finite stellar temperatures due to thermally-driven excitations of nuclei present in the star [65, 69], the overestimation of the electron-capture rates could amount to an order of magnitude or more. To reduce such large uncertainties, it is important to develop better estimates which requires a combination of improved theoretical approaches and high-quality data to

benchmark new models as they become available. Charge-exchange experiments are used to test theoretical predictions, but, as mentioned previously, only provide information about transitions from the ground state of the parent nucleus. Significant uncertainties related to the effects of finite temperature corrections on electron-capture rates still exist [65], but this is not a facet that charge-exchange experiments are able to examine.

Because of the astrophysical motivation presented here, an experimental program focused on using charge-exchange reactions at intermediate energies to measure Gamow-Teller strength distributions for the nuclei of primary interest is underway at the National Superconducting Cyclotron Laboratory. Experiments have been performed on several nuclei on and around the $N = 50$ shell closure, including ^{96}Mo(d,^{2}He) [89], ^{90}Zr(n,p) [90, 91, 92], ^{100}Mo(t,^{3}He) [93], and most recently, ^{88}Sr(t,^{3}He) [94] and ^{93}Nb(t,^{3}He) [95]. This thesis presents the results of the ^{86}Kr(t,^{3}He) experiment, which rounds out the chosen group of nuclei for this campaign. The experimental Gamow-Teller strength distributions will be compared with theoretical calculations, such as shell-model and QRPA calculations, in order to determine the validity of the current electron-capture rate sets, and to benchmark current and future theoretical developments.

Chapter 3

Theory

3.1 Introduction to Charge-Exchange Reactions

Charge-exchange reactions are used to examine a wide variety of phenomena, encompassing both nuclear structure and astrophysics. In a hadronic model, a charge-exchange reaction occurs when a neutron in the target nucleus is exchanged with a proton in the projectile nucleus, or vice versa. This process is mediated by the exchange of pions, or other mesons, between the projectile and the target when the reaction occurs at intermediate energies [7]. Experimentally, the projectile may be either a single nucleon, as in the case of an (n,p) or (p,n) reaction, or a composite probe, as in the case of $(t,{}^3\mathrm{He})$, $({}^3\mathrm{He},t)$ or $(d,{}^2\mathrm{He})$.

Because they are mediated by pion-exchange, the strong nuclear force governs the mechanics of this reaction. However, such a probe also provides information about reactions mediated by the weak nuclear force, namely β-decay, because both reactions populate the same initial and final states. In β-decay experiments, states can be measured from 0 MeV of excitation energy up to the Q-value of the reaction, and states with higher excitation energy cannot be observed via this reaction. In contrast, charge-exchange reactions are not limited in their scope by the reaction Q-value and can provide a complete spectrum up to high excitation energies.

Charge-exchange reactions are characterized by an isospin transfer ($\Delta T = 1$), and are

divided into two groups, based on their spin transfer. Fermi transitions are identified by no spin transfer ($\Delta S = 0$), while Gamow-Teller transitions are denoted by $\Delta S = 1$. Both of these types of transitions connect orbitals with the same principal quantum number, meaning that they produce no change in orbital angular momentum ($\Delta L = 0$). Therefore, describing these transitions in terms of the total angular momentum, J, Fermi transitions are denoted by $\Delta J = 0$ and Gamow-Teller transitions are denoted by $\Delta J = 1$.

The Fermi transition strength is almost completely exhausted by the excitation of the isobaric analog state (the state in the daughter nucleus with the same structure and isospin as the ground state of the parent nucleus, but with a different isospin projection). However, for neutron-rich systems, there is no isobaric analog state because the initial isospin is greater than 0. Therefore, Gamow-Teller transitions are of most interest in this work because of the associated spin transfer, which parallels that of β-decay reactions. The total amount of Gamow-Teller strength, $B(GT)$, including both the β^+ and β^- directions, for a particular nucleus is determined by the Ikeda sum rule [96]:

$$S(\beta^-) - S(\beta^+) = 3(N - Z), \tag{3.1}$$

where N is the number of neutrons present in the nucleus, Z is the number of protons, $S(\beta^-)$ is the Gamow-Teller strength in the β^- direction and $S(\beta^+)$ is the strength in the β^+ direction. Typically, only about 60% of the Gamow-Teller strength is measured experimentally because of quenching effects [97].

The operator that describes Gamow-Teller transitions is:

$$G_A \sum_j \overrightarrow{\sigma_j} \tau_{\pm j}, \tag{3.2}$$

in which G_A is the axial-vector coupling constant for the weak interaction, σ are the Pauli spin matrices, and τ is the isospin transition matrix [8]. The relationship between this operator and $B(GT)$ is given by the following equation:

$$B(GT)_{\pm} = \frac{1}{2J+1}\Big|\sum_j \langle\psi_F\|\sigma_j\tau_j^{\pm}\|\psi_I\rangle\Big|^2. \tag{3.3}$$

Here, ψ_I and ψ_F are the initial and final nuclear states, respectively, and J is the total angular momentum of the initial state.

As mentioned previously, charge-exchange reactions are characterized by an isospin transfer ($\Delta T = 1$), meaning that ΔT_z is $+1$ or -1. The case in which $\Delta T_z = -1$ corresponds to a (p,n)-type reaction, causing the residual nucleus to become more proton-rich. Conversely, the case in which $\Delta T_z = +1$ corresponds to an (n,p)-type reaction, in which the residual nucleus becomes more neutron-rich. A diagram of the directions of these reactions in the region around ^{86}Kr is shown in figure 3.1. In terms of astrophysical reactions, (n,p) reactions are in the same direction as electron-capture reactions (β^+-decay), shown by the red arrow in figure 3.1, and (p,n) reactions are in the same direction as β^--decay reactions on the chart of nuclides, shown by the green arrow.

The isospin of the target nucleus is given by the expression $T_z = (N - Z)/2$; this value determines the states that can be populated in the daughter nucleus, as shown in figure 3.2. If the isospin of the ground state of the target nucleus is T_0, then reactions in the (n,p) direction will populate only states in the residual nucleus with $T = T_0 + 1$; this occurs because the minimum isospin in the residual nucleus is equal to T_z. In the opposite direction, (p,n)-type reactions can populate states with $T = T_0 - 1$, T_0 or $T_0 + 1$.

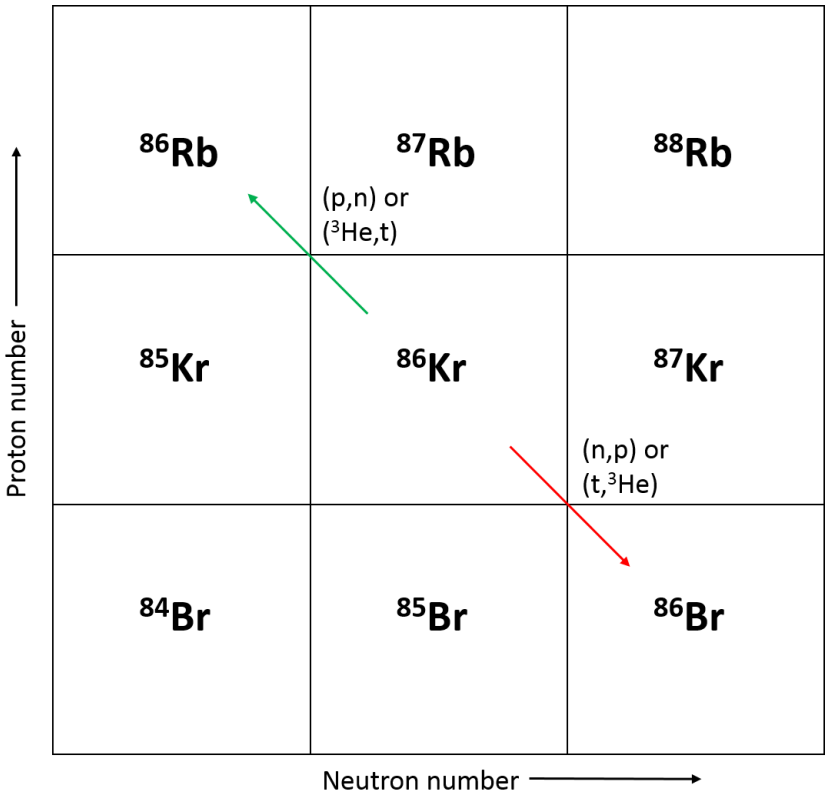

Figure 3.1: Diagram of charge exchange reactions involving ^{86}Kr. (n,p)- or $(t,^3\mathrm{He})$-type reactions involve an isospin change of $\Delta T_z = +1$ and yield a daughter nucleus that is more neutron-rich than the parent nucleus. (p,n)- or $(^3\mathrm{He},t)$-type reactions involve an isospin change of $\Delta T_z = -1$ and yield a daughter nucleus that is less neutron-rich than the parent nucleus.

3.1.1 *pf/sdg*-shell Interactions

Charge-exchange reactions change a neutron into a proton, or a proton into a neutron, depending on the direction of the reaction. Macroscopically, this is likened to exciting a proton-hole/neutron-particle, in the case of a (p,n) reaction, or exciting a neutron-hole/proton-particle, in the case on an (n,p) reaction. For stable, heavy nuclei the proton-neutron asymmetry is high, typically with a large excess of neutrons. Because of this configuration, excitations in the (n,p) direction within the same oscillator shell are impeded due to the Pauli-blocking effect; this phenomenon is illustrated in the simplified diagram of a nu-

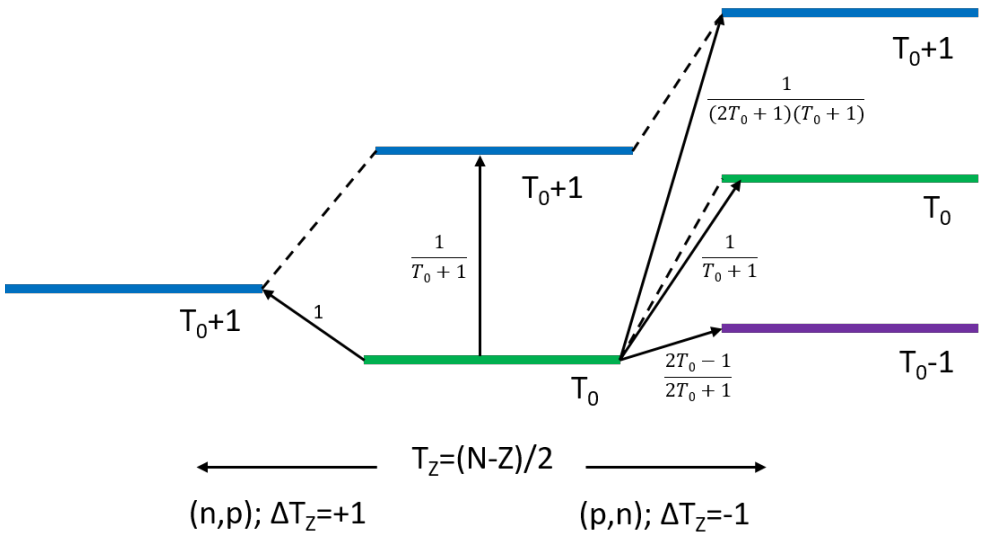

Figure 3.2: Isospin in charge-exchange reactions. The isospin of the ground state of the parent nucleus is equal to $(N-Z)/2$. In the (n,p) direction, only transitions from T_0 to T_0+1 states are available. Also shown in the figure are the Clebsch-Gordan coefficients corresponding to each transition; in the (p,n) direction, transitions to states with increasing isospin are suppressed compared to transitions to states with the same isospin. Figure adapted from [98, 99].

cleus above ^{78}Ni in figure 3.3. Protons are unable to transition to the low-lying neutron orbitals, and, as such, the only available transitions have a higher excitation energy. Because the overlap between the initial proton orbital and final, higher-lying neutron orbital is small, the Gamow-Teller strength in the β^+ direction is reduced. For the same nucleus, the Gamow-Teller strength in the β^- direction is unaffected, because excitations of a neutron-hole/proton-particle are available for all orbitals.

Nuclei in the pf/sdg-shell are an excellent example of the effect of such Pauli-blocking on the Gamow-Teller strength in the (n,p) direction. ^{86}Kr (Z=36) is a stable isotope, and is singly-magic with 50 neutrons. For nuclei that lie on the $N=50$ shell closure, the neutron shells are filled up to the $0g_{9/2}$ orbital (a diagram of the ordering of the orbitals is shown in figure 3.4). The protons, depending on the excitation of the nucleus, are distributed among

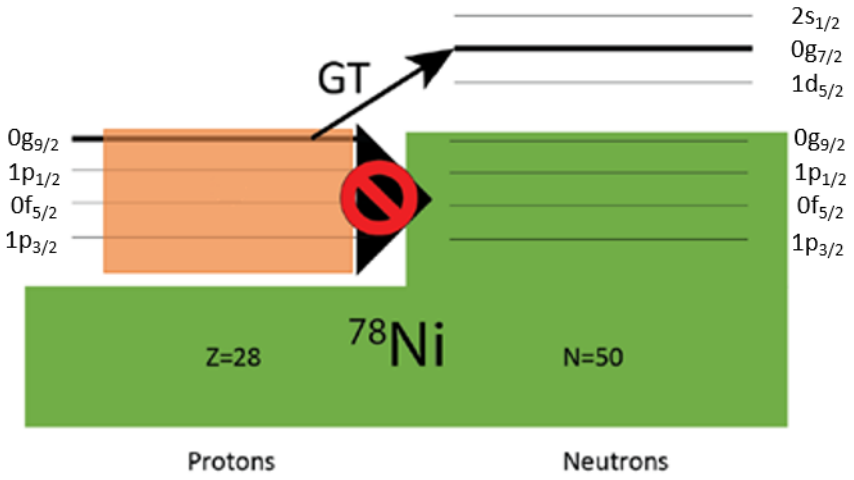

Figure 3.3: A representation of Pauli-blocking for heavy nuclei. Transitions with low excitation energy are blocked because the necessary orbitals are filled; therefore, the available transitions are required to have higher excitation energy. Because transitions with higher excitation energy are energetically unfavorable and, therefore, less likely to occur, the Gamow-Teller strength is subsequently diminished.

the $1p_{3/2}$, $0f_{5/2}$, $1p_{1/2}$, and $0g_{9/2}$ orbitals, when a ^{78}Ni core (Z=28) is assumed. Then, Gamow-Teller transitions cause a spin-transfer of $\Delta L = 0$ and $\Delta S = 1$, moving the valence protons from their original orbital in the target nucleus to a neutron orbital above $0g_{9/2}$ in the residual nucleus.

In the shell-model, this configuration is achieved by using the SNE model space [75, 76], which includes the orbitals of both the *pf*- and *sdg*-shells. The ordering of the levels is shown in figure 3.4. For calculations in this region, an inert core of ^{78}Ni ($Z = 28$, $N = 50$) is assumed: all of the protons and neutrons in this core are fixed and cannot participate in any transitions. Instead, a mean field for the core is taken into account to define the potential well of the nucleus. Using ^{78}Ni as an inert core is a reasonable assumption because the Gamow-Teller strength for the nucleus is extremely small [101]. The jj44pna interaction [78] is used for these calculations within the shell-model calculation framework, NUSHELLX

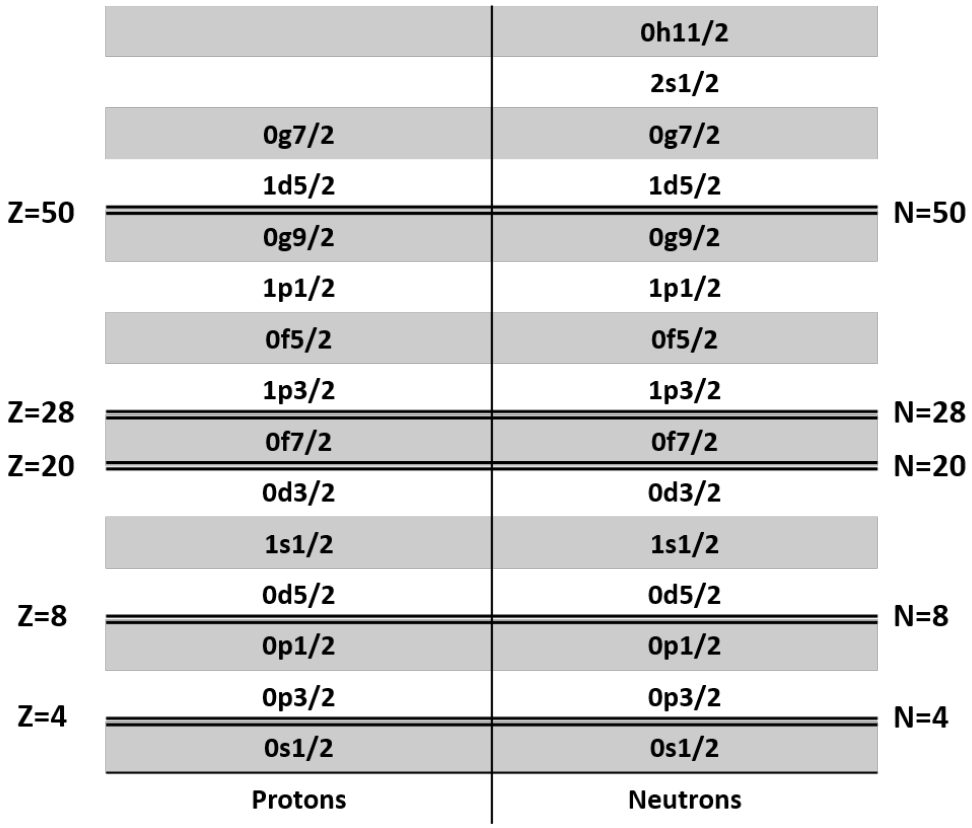

Figure 3.4: Configuration of orbitals in the nuclear shell-model up to the *sdg* shell. Figure adapted from [100].

[79].

Because the nuclei in the *pf*- and *sdg*-shells have a large number of valence particles and possible transitions, it is necessary to make truncations to the model space, otherwise the calculations become too computationally intensive. These constraints and their effect on the available Gamow-Teller transitions are shown in figure 3.5. The left-hand panel of the figure shows all available Gamow-Teller transitions in the *pf/sdg*-shell. The first model space simplification is in the form of the core used in the calculation, as discussed previously. In the case of ^{86}Kr, the assumption of the ^{78}Ni core leaves 8 valence protons that are distributed in orbitals up to the $0g_{9/2}$, and are available to participate in Gamow-Teller transitions. There are no valence neutrons because both ^{86}Kr and ^{78}Ni are $N = 50$ nuclei; therefore, all of

the neutrons are fixed in place by the core in this example. The center panel of figure 3.5 illustrates the reduction in the number of possible transitions when the core of the nucleus is fixed.

The other truncation concerns orbitals above the *sdg*-shell; because transitions to higher-lying orbitals are extremely unlikely, protons are prohibited from occupying them. For these calculations, proton orbitals above $0g_{9/2}$ and neutron orbitals above $1d_{3/2}$ are omitted. The right-hand panel of figure 3.5 shows this final model space truncation, and the further reduction in available Gamow-Teller transitions in this model space. After all of these restrictions, only one Gamow-Teller transition is available in the calculations: $\pi 0g_{9/2} \rightarrow \nu 0g_{7/2}$.

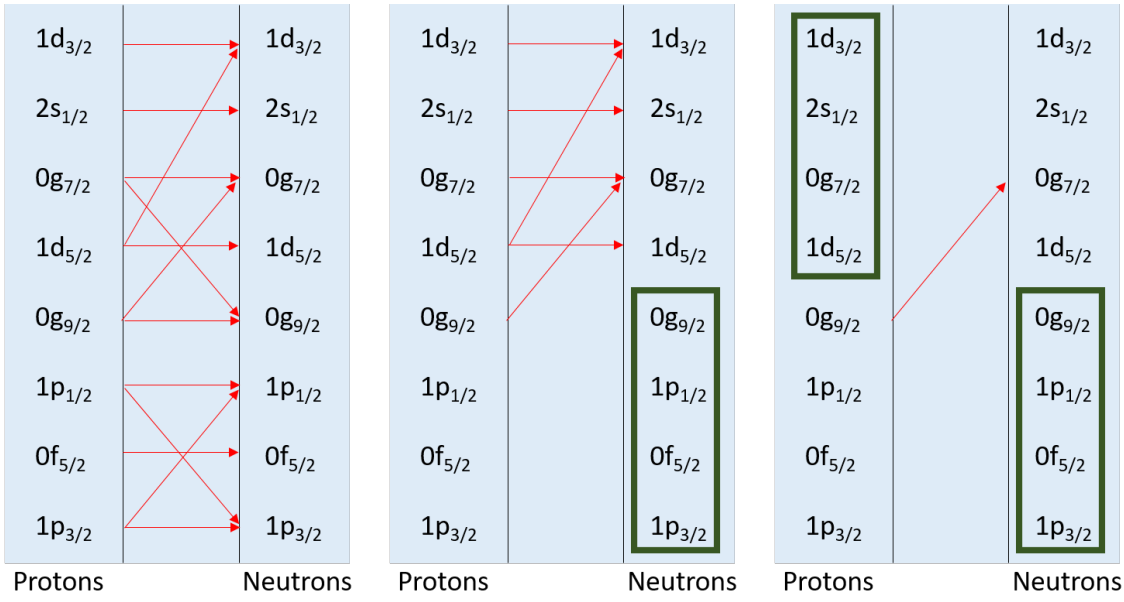

Figure 3.5: Simple explanation of the model space truncations used in OXBASH calculations. The panel on the left shows all possible Gamow-Teller transitions, assuming nucleons are free to move to any orbitals. The middle panel shows the application of a ^{78}Ni core, filling all of the neutron orbitals up to the $g_{9/2}$ orbital, and then eliminating those particles from the set that are available to participate in transitions. The panel on the right forces the proton orbitals above the $g_{9/2}$ to remain empty, because it is unlikely for protons to exist there. Both of these restrictions lead to a single remaining transition: $\pi 0g_{9/2}$ to $\nu 0g_{7/2}$.

In order to determine whether these shell-model restrictions are acceptable, it is necessary to compare the Gamow-Teller transition strength distribution obtained from shell-model calculations to the strength distribution extracted from a charge-exchange experiment [93]. Then, discrepancies between the experimental and theoretical strength distributions, either in the details of the distribution or the cumulative strength, indicate ways in which theoretical models can be improved. Attributes, such as the deformation of the nucleus or the accuracy of the single-particle energies, incorporated into the theory yield a more robust the theoretical framework, leading, in turn, to more accurate experimental Gamow-Teller strength distributions.

3.2 Reaction Theory

Cross section calculations for $(t,^3\mathrm{He})$ experiments are performed with the double-folding code, FOLD [102, 103]. FOLD uses Distorted Wave Born Approximation (DWBA) methods, in which both the incoming and outgoing waves are distorted by the mean field of the target nucleus. Inputs to the calculation include single-particle wavefunctions and one-body transition densities for the reaction in question, a nucleon-nucleon interaction and an optical potential. The code uses a three step process to calculate the incoming and outgoing distorted waves, the transition matrix and the cross section.

3.2.1 DWBA

In the DWBA method, the scattering potential is divided into two parts: one with a known solution, typically an elastic scattering potential, and one that contains any residual inter-

actions. Here, the residual interaction is the charge-exchange interaction:

$$V = U_{\text{elastic}} + W_{\text{charge-exchange}} \tag{3.4}$$

A T-matrix is used to describe the transition between the initial and final states in the reaction. When the potential is substituted into the T-matrix it is similarly split into two parts [104, 105]:

$$T_{fi} = \langle \phi | T^{+} | \phi \rangle = \langle \phi | U_{\text{elastic}} + W_{\text{charge-exchange}} | \psi^{+} \rangle \tag{3.5}$$

$$T_{fi} = \langle \phi | U_{\text{elastic}} | \chi^{+} \rangle + \langle \chi^{-} | W_{\text{charge-exchange}} | \psi^{+} \rangle \tag{3.6}$$

where $|\chi^{+}\rangle$ and $|\chi^{-}\rangle$ are the incoming and outgoing distorted waves.

The first term in equation 3.6, containing the elastic scattering potential, is neglected, because the operator is isoscalar and is unable to connect the initial and final states of such a reaction. Therefore, only the term containing the charge-exchange interaction remains to be evaluated. The elastic potential is still used, however, to generate the distorted waves. Including the distorted waves, the simplified transition matrix is now written as [104, 105]:

$$T_{fi} = \langle \chi_f^{+}(\vec{k}_f, \vec{R}') | F(\vec{R}') | \chi_i^{-}(\vec{k}_i, \vec{R}') \rangle. \tag{3.7}$$

Here, $F(\vec{R}')$ is the form factor, which provides information about the interaction between the nucleons in the projectile and the nucleons in the target. It is a folded transition density, in which the overlap between the initial and final states is calculated, while taking into account the projectile-nucleus interaction [104, 105]. The first step of the FOLD code, called WSAW,

calculates the radial part of the single particle wavefunctions, using the nucleus charge, core mass and binding energies of the protons and neutrons in valence orbitals that participate in the reaction. Then, the second part of the FOLD code, called FOLD, calculates the form factor, $F(\vec{R}')$ from equation 3.7, using these wavefunctions, along with the energy of the incoming particle, an effective interaction and one-body transition densities. Double-folding, or integrating over the nucleons in both the target and projectile, is necessary because the probe (a triton, in this case) is not a point particle.

The form factor, when written in its entirety, can be reduced to two parts: one that depends only on the spin and isospin coordinates ($\vec{\sigma}$ and $\vec{t}$), and another that depends only on the spatial coordinates ($\vec{r}$). The spatial coordinates used here are defined in figure 3.6. The potential contained within the form factor, $F(\vec{R}')$, is equal to the charge-exchange portion, as defined in equation 3.4: $W_{\text{charge-exchange}} = V - U_{\text{elastic}}$. As stated previously, because the interaction of interest is isovector, the elastic term, U_{elastic}, is neglected, as it is isoscalar. This leaves only the term that depends on V, the sum of all two-body interactions between the target and projectile, given by:

$$V = \sum_{i,j} V(|\vec{r_i}' - \overrightarrow{r_j}|, \vec{\sigma_i}', \vec{\sigma_j}, \vec{t_i}', \vec{t_j}), \tag{3.8}$$

where i and j refer to the particles in the target and projectile that are being summed over, σ is the spin and t is the isospin of the particle in question, and the spatial coordinates are defined in figure 3.6.

If the projectile is assumed to carry no orbital angular momentum, then the two portions of the wavefunctions (spatial and spin/isospin) can be completely separated by re-writing the form factor using an effective potential, V_{eff}, which characterizes the interaction between a

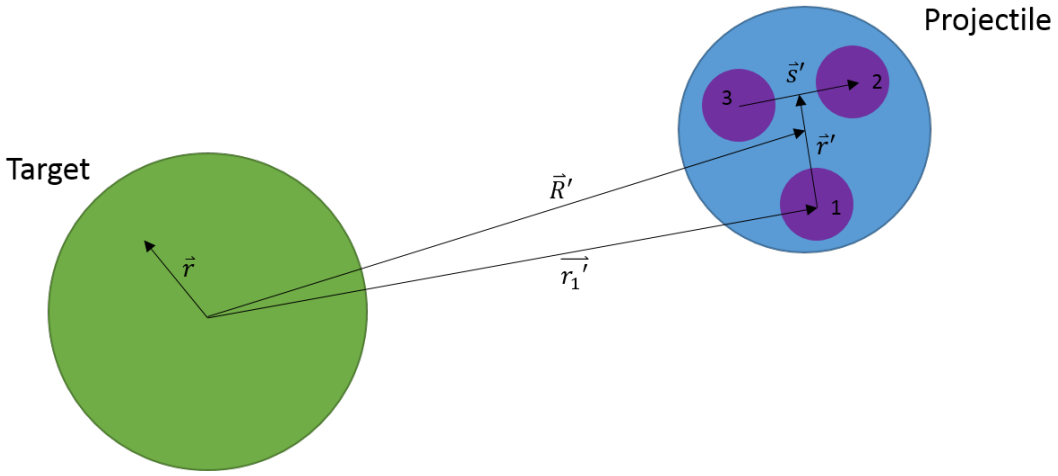

Figure 3.6: Definition of the spatial coordinate system used in the DWBA formalism. This figure was adapted from [105].

nucleon in the target and a nucleon in the projectile at $\vec{r}'$ and $\vec{r_j}'$, respectively [104, 105]:

$$V_{eff}(\vec{R}', \vec{r}, \vec{\sigma}, \vec{t}, \vec{\sigma_j}', \vec{t_j}') = \int d\vec{r}' d\vec{s}' f_f(\vec{r}', \vec{s}') f_i(\vec{r}', \vec{s}') V(|\vec{r_j}' - \vec{r}|, \vec{\sigma_i}', \vec{\sigma_j}, \vec{t_i}', \vec{t_j}), \tag{3.9}$$

where V is the sum of the two-body interactions, as defined in equation 3.8, and f_i and f_f are the components of the internal wave function of the projectile and ejectile, respectively, that depend only on the spatial coordinates. With the effective interaction, defined in equation 3.9, the form factor can be re-written using the following expression:

$$F(\vec{R}') = \langle \alpha_e \alpha_r | V_{eff} | \alpha_t \alpha_p \rangle, \tag{3.10}$$

where $\alpha_{e,r,t,p}$ are the wavefunctions of the ejectile, residual, target and projectile, respectively, and V_{eff} is the effective interaction between nucleons in the target and projectile.

Combining all of this information for the target and projectile of interest, the transition matrix element, T_{fi}, is generated, and is used to calculate the differential cross section for

the reaction:

$$\frac{d\sigma}{d\Omega} = \Big(\frac{\mu}{2\pi\hbar^2}\Big)^2 \frac{k_f}{k_i} |T_{fi}|^2, \tag{3.11}$$

where μ is the reduced mass of the system, and k_i and k_f are the incoming and outgoing wave numbers. The final part of the FOLD code, called DWHI, calculates the transition matrix elements, T_{fi} from equation 3.7, using the previously-calculated form factor (equation 3.10), along with a suitable optical potential, which is used to generate the distorted wavefunctions. Finally, with the matrix elements, DWHI calculates the cross section for the reaction, after equation 3.11.

3.2.2 Calculation inputs

Several inputs are needed to perform DWBA calculations for the ^{86}Kr(t,^{3}He) reaction. First, an effective interaction is needed to calculate transition matrix elements; such calculations are complex and depend on a large number of parameters, including the energy of the projectile and the structure of the target nucleus. Charge-exchange experiments are performed at intermediate energies, typically greater than 100 MeV/u, and a free nucleon-nucleon interaction is a reasonable approximation. In this assumption, all of the nucleons in the target and projectile may be distinguished from one another, and non-locality effects are neglected.

The interaction typically used to calculate (t,^{3}He) reaction cross sections is the Love-Franey interaction at 140 MeV/u [106, 107, 108]. Consisting of three components, the potential used in this framework contains central, spin-orbit and tensor terms:

$$V_{12} = V^c(r_{12}) + V^{LS}(r_{12})\,\overrightarrow{L}\cdot\overrightarrow{S} + V^T(r_{12})S_{12}. \tag{3.12}$$

Each of the components is decomposed in terms of Yukawa potentials, $Y(x) = \frac{e^{-x}}{x}$, which are similar to the one-pion exchange potential (OPEP):

$$\begin{aligned} V^C(r) &= \sum_{i=1}^{N_C} V_i^C Y(r/R_i) \\ V^{LS}(r) &= \sum_{i=1}^{N_{LS}} V_i^{LS} Y(r/R_i) \\ V^T(r) &= \sum_{i=1}^{N_T} V_i^T Y(r/R_i) \end{aligned} \tag{3.13}$$

where the sums run over the ranges of the π, ρ and 2-π meson exchanges, respectively. The range of the π meson exchange at 140 MeV/u is known to be 1.4 fm, while the ranges of the ρ and 2-π meson exchanges are assigned a value based on fits to nucleon-nucleon scattering data [106].

Each of the components in the NN-interaction are represented by two terms: *direct* and *exchange*. The direct term describes the case in which a neutron is turned into a proton, or vice versa, via meson exchange. The exchange term describes the case in which the target neutron (proton) is struck and ejected from the nucleus, and the projectile proton (neutron) is captured and replaces it [8]. While the direct terms can be calculated without the need for simplifications or approximations, the exchange terms are less straightforward. These terms contain non-local effects, which are not calculated exactly in FOLD; instead, a short-range approximation is used [106]. While this approximation is acceptable for simple charge-exchange probes, such as (n,p) reactions, for more complex probes, such as (t,^{3}He) reactions, the exchange term is known to be too weak [109, 110, 111]. Because the direct and exchange components interfere destructively, this leads to an overestimation in the calculated cross section, typically on the order of 30% [12, 110]. However, because the experimental

analysis, discussed in sections 4.5 and 4.6, only uses the shape of the calculated DWBA cross section, not its magnitude, the validity of the short-range approximation and the effect on the magnitude of the cross section are not considered in great detail here.

The next nuclear physics input to the DWBA calculation is the optical potential, which is used to determine the extent to which the incoming and outgoing waves are distorted by the mean field of the target nucleus. This mean field takes the form of a Woods-Saxon potential with both a real and an imaginary component, combined with the Coulomb interaction [112]:

$$V = V_C + U + iW. \tag{3.14}$$

The Coulomb term of the potential takes the following forms:

$$\begin{aligned} V_C(r) &= Z_p Z_T e^2/r \quad \text{for} \quad r > R_C \\ V_C(r) &= Z_p Z_T e^2(3 - r^2/R_C^2)/2R_C \quad \text{for} \quad r < R_C, \end{aligned} \tag{3.15}$$

where $R_C = r_C A^{1/3}$, and r_C is the reduced Coulomb radius. Each of the Woods-Saxon components describing the potential well depth takes the following form [105]:

$$V(r) = \frac{V_0}{1 + [\exp(r - r_n A^{1/3})/a_n]} \tag{3.16}$$

where V_0 is the depth, r_n is the radius and a_n is the diffuseness of the potential. To obtain values for these parameters, fits of elastic scattering data on the nucleus of interest are made, and the constants are extracted, based on the shape of the calculated angular distribution. Elastic scattering data is unavailable for every nucleus, and there is a dearth of available data in the middle- to heavy-mass region; therefore, at times, it is necessary to use the optical

potential for a nucleus that is merely close in mass to the target nucleus. For nuclei such as ^{86}Kr or ^{88}Sr, the optical potential for ^{90}Zr is used [113].

Elastic ^{3}He scattering data on ^{90}Zr at 443 MeV were used to obtain the optical potential parameters. The extracted values correspond to the ^{3}He channel, which, for a (t,^{3}He) reaction, is the outgoing channel. In order to obtain the distorted wave for the incoming triton, the real and imaginary potential depths from the ^{3}He reaction are scaled to 85% of the original value [114]; the other parameters remain the same. The optical potential values for both the incoming triton and outgoing ^{3}He waves are presented in table 3.1.

Table 3.1: Optical potential parameters used in the DWBA calculations for nuclei in the pf/sdg-shells. These values were determined from ^{3}He elastic scattering on ^{90}Zr at 443 MeV [113].

	V_R	r_R	a_R	W_I	r_I	a_I
Incoming triton	-26.5 MeV	1.363 fm	0.818 fm	-35.8 MeV	1.04 fm	1.06 fm
Outgoing ^{3}He	-32.1 MeV	1.363 fm	0.818 fm	-42.1 MeV	1.04 fm	1.06 fm

The final inputs to the FOLD code are one-body transition densities (OBTDs), typically from shell-model or other microscopic calculations, which provide structure information about the target and residual nuclei. Additionally, each 1p-1h amplitude that is included in the calculation is weighted depending on the OBTD used: smaller transition densities indicate a small overlap between the initial and final states, meaning that such a transition is less probable. As mentioned in section 3.1.1, for the middle-mass nuclei in the pf/sdg-shell, only one transition contributes to the Gamow-Teller distribution: $\pi 0g_{9/2}$ to $\nu 0g_{7/2}$. One-body transitions densities for ^{86}Kr and ^{88}Sr were calculated in OXBASH [115] in the SNE model space [75, 76] using the SNET interaction [76]. For the experimental analysis that uses the DWBA result, discussed in further detail in section 4.6, the interaction used to generate the one-body transition densities is less important. It is the shape of the angular distribution

that is critical, and can be obtained using one-body transitions densities from any reliable shell-model interaction.

OBTDs obtained from the shell-model calculation are converted from their original *pn*-formalism value to a format to follow the reduced matrix element convention [115]:

$$Z = \text{OBTD} \times \frac{\text{CG} \cdot \widehat{\text{dT}}}{\widehat{J_i} \cdot \widehat{T_f}} \tag{3.17}$$

where $\widehat{J_i}$ is equal to $\sqrt{2J_i + 1}$, where J_i is the spin of the initial state. $\widehat{\text{dT}}$ and $\widehat{T_f}$ are similarly defined for the change in isospin and isospin of the final state, respectively. CG refers to the Clebsch-Gordan coefficient for the transition, and is defined by the following expression:

$$CG = \langle T_i \Delta T; T_{im} \Delta T_m | T_i \Delta T; T_f T_{fm} \rangle, \tag{3.18}$$

where $T_{i,f}$ are the total isospins of the inital and final states, T_{im} and T_{fm} are the isospin projections of the initial and final states, and ΔT and ΔT_m are the changes in the total isospin and the isospin projection, respectively, for the reaction.

3.3 Gamow-Teller Strength Distribution

There is a well-known proportionality between the Gamow-Teller transition cross section and $B(GT)$ [12, 51, 52], given by the following equation:

$$\left[\frac{d\sigma}{d\Omega}(q = 0)\right]_{GT} = \widehat{\sigma} B(GT). \tag{3.19}$$

The left-hand side of the equation is the Gamow-Teller cross section at zero momentum transfer ($q = 0$), obtained in theoretical calculations by setting the Q-value of the reaction to 0 MeV and taking the cross section at zero degrees. Experimentally, the cross section that is measured is a combination of all possible charge-exchange transitions. In order to extract the $\Delta L = 0$ component, a multipole decomposition analysis is performed by fitting the experimental angular distribution with a linear combination of multipole curves, as derived from a DWBA calculation. The $\Delta L = 0$ component obtained from this fit is used to calculate the cross section at zero momentum transfer ($q = 0$), which appears on the left-hand side of equation 3.19.

The constant of proportionality is called the unit cross section and, for Gamow-Teller transitions, is approximately constant for all transitions. $\widehat{\sigma}$ is calculated using the following expression:

$$\widehat{\sigma} = KN^D|J_{\sigma\tau}|^2. \tag{3.20}$$

Here, K is a kinematic factor, depending on the energies of the incoming and outgoing channels, the incoming linear momentum of the projectile, and the outgoing linear momentum of the ejectile. N^D is a distortion factor, representing the effect of the mean field of the target nucleus on the scattering waves. At zero momentum transfer, the distortion factor is defined as the ratio of the DWBA cross section to the PWBA (partial-wave born approximation) cross section. Finally, $|J|$ is the integral of the $\sigma\tau$ component of the effective interaction between the projectile and target nucleons. For experimental data, the unit cross section can be calculated using an expression that is dependent only on the mass number of the target nucleus: $\widehat{\sigma} = 109/A^{0.65}$. This equation provides a reasonable value for $\widehat{\sigma}$ for nuclei with $A \geq 12$, as shown in previous studies [12, 51, 116, 117, 118].

The Gamow-Teller strength distribution is a useful result in its own right, yielding information about the structure and configuration of the nucleus. When obtained experimentally, it can be compared to theoretical models in order to discern which models replicate experimental results well, and where improvements can be made. Additionally, the strength distribution, obtained from theoretical calculations or experimental data, can be used to calculate weak-reaction rates, which are of great interest in this work, and are discussed in greater detail in chapter 5. Following the discussion in chapter 2, electron-capture rates for a nucleus are known to be sensitive to its Gamow-Teller strength distribution. Because so many nuclei participate in simulations of astrophysical phenomena, and because it is impossible to measure them all experimentally, being able to obtain Gamow-Teller strengths and electron-capture rates by other methods, while still retaining accuracy, is an invaluable tool.

Chapter 4

Experiment

The ^{86}Kr(t,^{3}He+γ) experiment was performed at the National Superconducting Cyclotron Laboratory at Michigan State University. Production of a triton beam by the facility has been used extensively by the charge exchange group for studying the Gamow-Teller strength distribution for nuclei in the β^+ direction [15, 48, 50].

4.1 Experimental Setup

4.1.1 Beam Production

The triton beam at the NSCL was produced by initially creating a primary beam of ^{16}O at 150 MeV/u using the K500 and K1200 coupled cyclotrons, and impinging it on a beryllium production target with a thickness of 3525 mg/cm^2. This method was determined to be optimal by Hitt *et al.* [15] to produce a secondary triton beam with an energy of approximately 115 MeV/u. To remove ^{6}He and ^{9}Li contaminants from the triton beam, an aluminum wedge with a thickness of 195 mg/cm^2 was inserted into the A1900 fragment separator [14]. The slits in the A1900 were set to obtain a momentum acceptance of $\pm$0.25% (0.5% total). After the beam was separated with the desired purity (>99%), it was transported to the target position and the S800 magnetic spectrometer [16], located in the S3 vault at the NSCL. The Coupled Cyclotron Facility, A1900 fragment separator, and beam line leading to the S800

spectrometer are shown in figure 4.1.

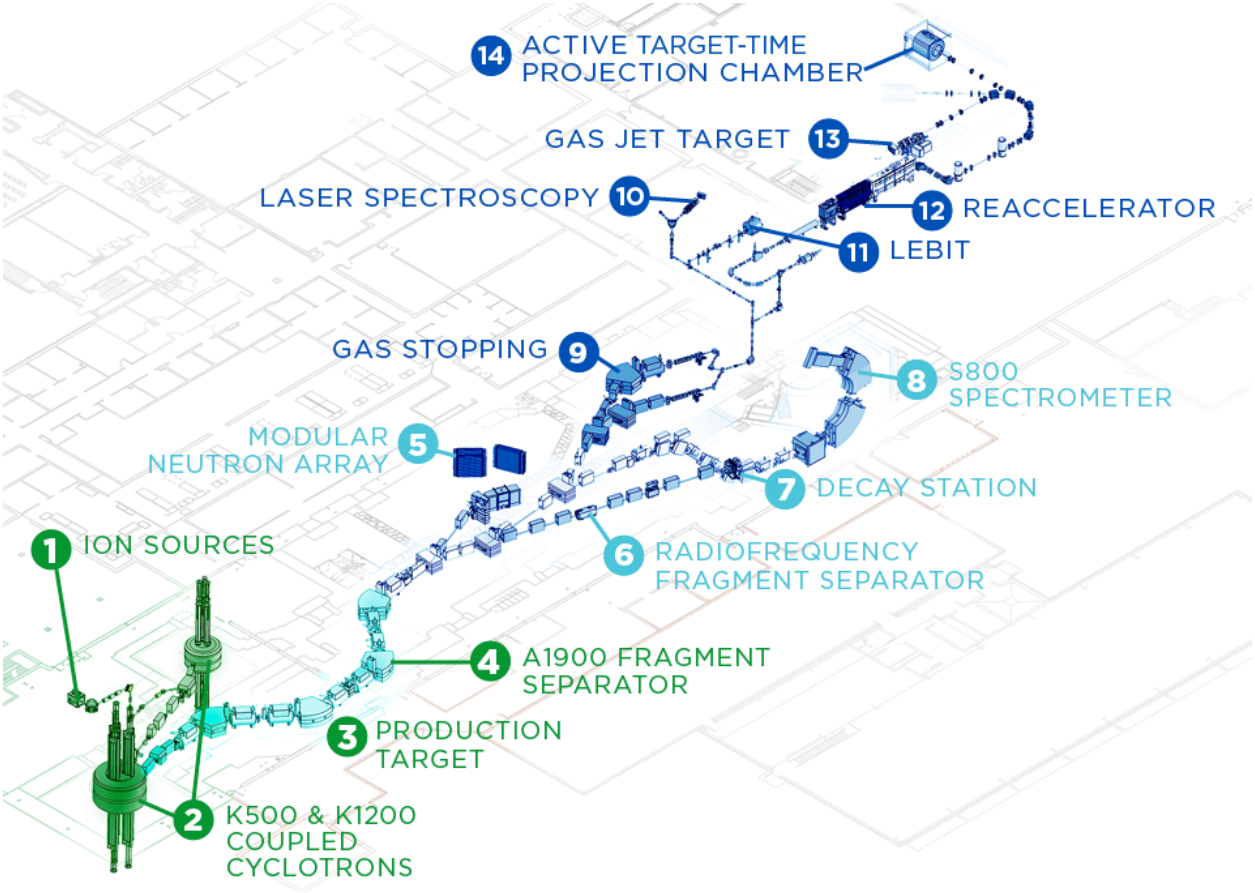

Figure 4.1: Schematic of the Coupled Cyclotron Facility, the A1900 fragment separator and the beamline to the S3 vault and the S800 magnetic spectrometer. Image credit to the NSCL.

For this experiment, the analysis beam line was operated in dispersion-matched mode to obtain the best possible resolution in the focal plane of the spectrometer. During dispersion-matching tuning, the beam was focused in the non-dispersive direction and momentum-dispersed along the dispersive axis, creating a tall, thin beam spot. The beam line was tuned to yield a beam that was momentum-distributed across the target with a dispersion equal to that of the S800 spectrometer ($D_S = -9.536$ cm/%). Then, when the beam particles passed through the spectrometer, its intrinsic dispersion compensated for the initial dispersion of

the beam, focusing all of the beam particles to a single point in the focal plane, as shown in figure 4.2b. The process of lateral dispersion-matching optimizes the measured energy resolution of the ejectile particles in the focal plane, improving the energy resolution that is calculated for the recoil particle.

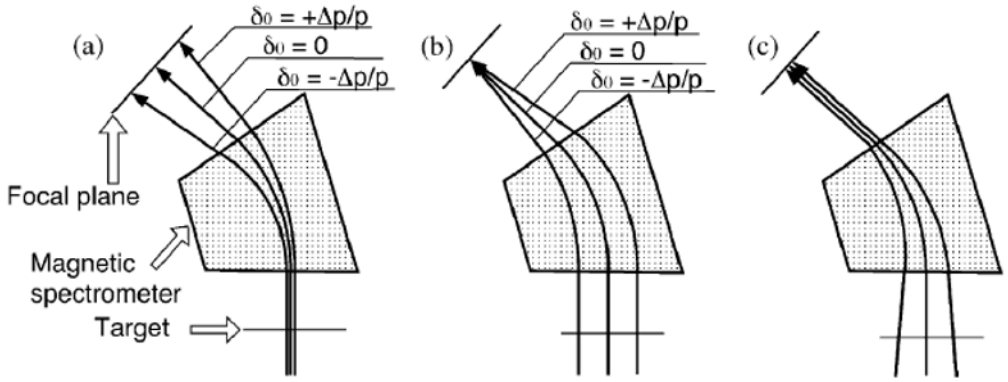

Figure 4.2: A visual explanation of dispersion matching within a high-resolution spectrometer. a) shows the focus mode, in which the beam is focused on the target, leading to a large dispersion of ejectiles in the focal plane. b) and c) show dispersion matching with only lateral, and both lateral and angular dispersion-matching, respectively. By tuning the beam to have a dispersion that is the same as that of the spectrometer, the energy resolution in the focal plane of the spectrometer is improved greatly. This figure was taken from reference [119].

With the ±0.25% momentum acceptance, which allowed for complete transmission of the beam through the beamline, a beam spot that was approximately 5 cm tall in the dispersive direction and approximately 0.5 cm wide in the non-dispersive direction was produced. In order to direct ^{3}He ejectiles into the focal plane of the S800, the rigidity of the spectrometer was set to 2.32 Tm. During beam tuning, a viewer, made of an aluminum plate coated in red phosphorus, which scintillates when the beam impinges upon it, was placed immediately in front of the target position to check the position of the beam and the shape of the beam spot. An image intensifying camera was used to see the shape of the beam spot on the viewer

during secondary tuning, as shown in figure 4.3.

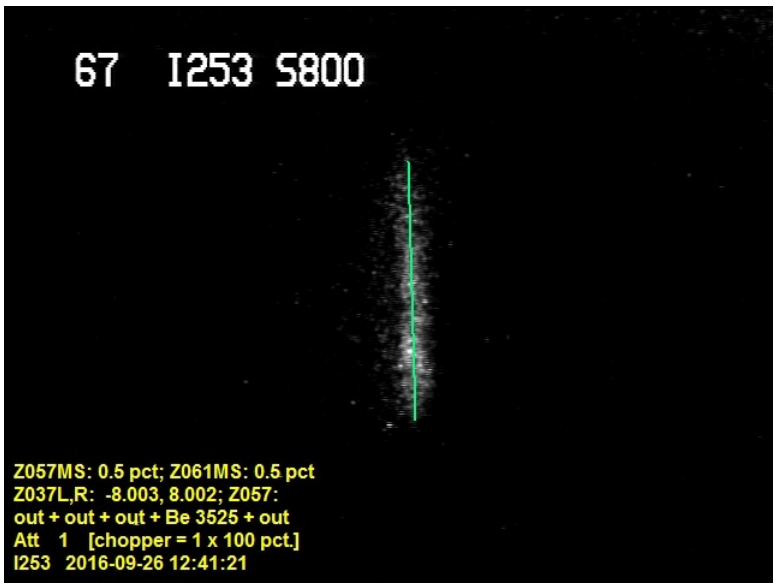

Figure 4.3: An image of the beam spot on the target viewer during dispersion-matched tuning. The dispersion of the tall beam matches that of the spectrometer, such that this beam will become focused to a single point in the focal plane of the S800. Photo courtesy of the NSCL A1900 group.

4.1.2 Krypton Target

The krypton gas cell was attached to a simplified version of the Ursinus College Liquid Hydrogen Target [120]. The cell had a diameter of 7 cm and a depth of 3 cm, and was fabricated specifically for the experiment to accommodate the dispersion-matched beam spot; it is shown in figure 4.4. For the krypton production runs, the target cell was filled with ^{86}Kr gas with a purity of 99.952%. The target windows were made of kapton foil ($C_{22}H_{10}N_2O_5$) with a thickness of 125 μm. In past charge-exchange experiments, a CH_2 target was used to assist in the calibration and normalization of the data [48, 116, 121, 122]. In this experiment, however, the kapton contained carbon in sufficient quantities that calibrations were able to be performed using the production run data sets.

During the beam time, it was found that, due to the wide spacing of the target windows, events from each foil produce distinct peaks in the spectra, as opposed to experiments that have thin target foils, in which all of the events from the target windows fall into a single peak. Such behavior was observed because of the uncertainty of the event locus. The ray-tracing routine used in the analysis, discussed further in section 4.2.4, assumed that all events originated in the center of the target; this assumption is typically valid for experiments with thin targets because the deviation between the actual event position and the assigned position are within the experimental position resolution. However, because of the thickness of the target in this experiment, the deviation between the actual event location and the calculated event location was greater, leading to the double peak in the spectrum, as events from the upstream foil were placed behind their actual locus, and events from the downstream foil were placed in front of their actual locus.

Because such a phenomenon complicates the extraction of the krypton signal (section 4.4), two additional sets of data were taken in order to have a better understanding of the contributions of the target windows to the total measured cross section. The first set had only the upstream foil of the gas cell present in the target position, and the second had only the downstream foil of the gas cell present. Because the total cross section from events on the target windows is the sum of the contributions of each foil with some additional energy loss corrections, these two additional data sets were used to develop a model of both the empty target cell (as proof that the subtraction method was reasonable) and of the krypton cell. The method of subtracting the target window events from the krypton data is discussed in detail in section 4.4.

It was originally proposed to fill the cell to a pressure of 760 Torr and then cool the cell to a temperature of 120 K, to increase the target thickness in order to obtain sufficient statistics.

However, while testing with the target system with neon gas, it was determined that the target windows would not hold against the gas pressure at low temperatures, because of the large surface area of the cell. Instead, the gas cell was kept at a temperature of 295 K, and then filled with ^{86}Kr gas to a pressure of approximately 1210 Torr. Although there were some small pressure fluctuations, it can be assumed that the density of the target remained effectively constant throughout the experiment with a thickness of 20 $\pm$ 0.5 mg/cm^3.

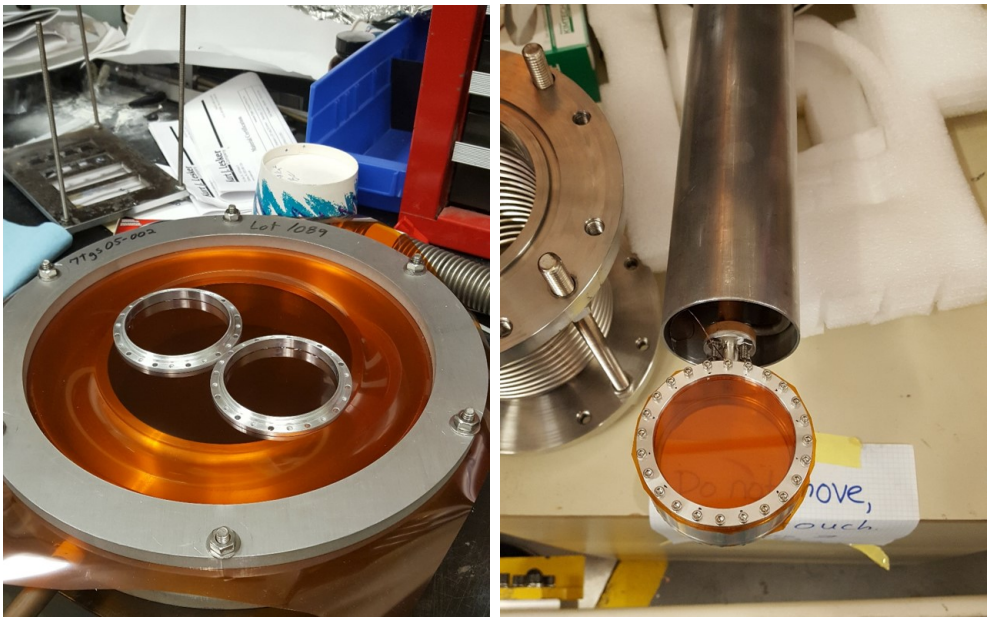

Figure 4.4: Left: The kapton foils curing on a vacuum ring to ensure the seal is strong. Right: The freshly-glued and assembled krypton gas cell attached to the gas handling and temperature regulation system.

4.1.3 S800 Magnetic Spectrometer

The S800 magnetic spectrometer consists of two dipole magnets and two quadrupole magnets that are used to direct ^{3}He ejectiles into the focal plane. Particles pass through two Cathode Readout Drift Chambers (CRDCs) providing information enabling the reconstruction of position and angle measurements for each event. The CRDCs have an active area of 56 cm

in the dispersive direction by 26 cm in the non-dispersive direction. CRDC1 is placed at the optical focal plane and CRDC2 is located 1 m downstream from the focal plane [123].

Each detector is filled with a gas mixture that is 80% CF_4 and 20% C_4H_{10}; this mixture is used because of its high drift velocity and low avalanche electron spread [123]. Particles entering the detectors ionize the gas and produce ion-electron pairs; the electrons drift toward the anodes in the CRDC, generating a current in the wires closest to the locus of the event. This current causes a charge to be induced on two sets of cathode pads, placed before and after the anode wires. The charge distribution is spread across approximately 8 pads, and a Gaussian fit to the distribution was used to determine the position of the event in the dispersive direction; the position in the non-dispersive direction was obtained from the drift time of the electron to the anode wire. In order to calculate the angle of each particle track through the CRDCs, the line connecting the position of the event in each CRDC was calculated and the angle at which the particle was traveling was extracted, as shown in figure 4.5.

A plastic scintillator was placed behind the CRDCs to measure the energy loss of the ejectile particle after it traveled through the spectrometer. Additionally, the signal in the scintillator provided a trigger for the S800 data acquisition system, and was used as the starting time for the time-of-flight measurement; the cyclotron RF signal yielded the stopping time. The difference between the start and stop times is a measure of the time-of-flight of the ejectile from the target position to the focal plane of the spectrometer. Both the energy loss measured in the plastic scintillator and the time-of-flight were used for particle identification, which will be discussed in more detail in section 4.2.1.

The CRDCs have inherent noise that must be eliminated so that the event amplitude, used during event fitting to determine the location of the event, is accurate. For this,

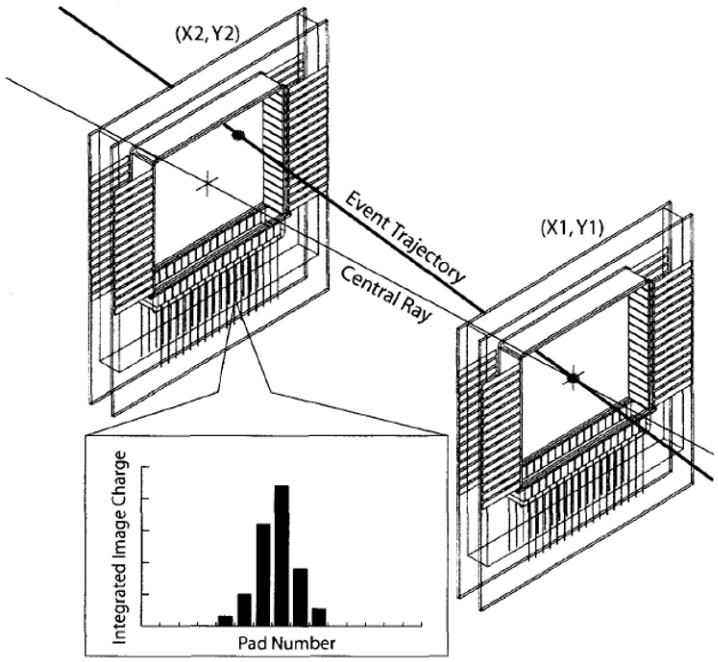

Figure 4.5: A diagram of the event tracking performed by the CRDCs in the focal plane of the S800. The horizontal position of the hit is determined by the pattern of pads that fire during the event; the vertical position is determined by the drift time of the electrons in the chamber. This figure was obtained from [123].

data were taken when there was no beam present in the spectrometer, and the spectra for the CRDCs were analyzed. Any peaks in the spectra (figure 4.6) were attributed to noise in the cathode pads. The pedestal for the spectrometer is a set of constant values, each corresponding to a pad in the CRDCs; the value indicates how much noise the pad typically measures. During event fitting, the pedestal value was subtracted from the recorded pad charge to provide the true energy measurement for the event.

4.1.4 GRETINA

GRETINA is the first stage of the Gamma-Ray Energy Tracking Array (GRETA), built at Lawrence Berkeley National Laboratory (LBNL) in 2011 and moved to different institutions (e.g. LBNL, NSCL and Argonne National Laboratory (ANL)) to complete a range of exper-

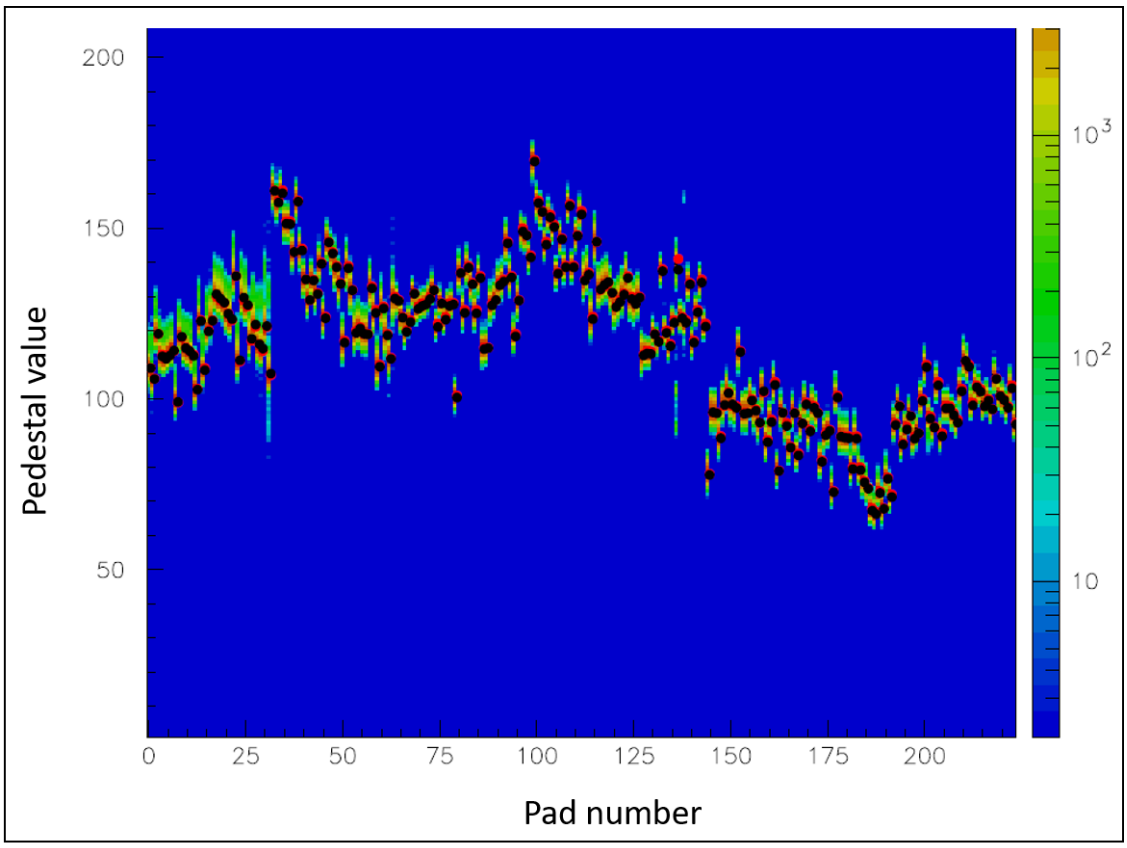

Figure 4.6: Diagram of the pedestal data for the first CRDC; these data were taken with no beam in the spectrometer. The peaks are characterized and a pedestal is extracted for each pad, in order to subtract the pad noise from the experimental data, yielding the most accurate energy measurement for each event.

imental campaigns. When it is complete, the array will cover nearly 4π solid angle with 20 detector modules.

During the experiment, GRETINA consisted of 8 detector modules, each containing four high-purity germanium crystals and a cryostat. The germanium crystals are segmented into 36 electrically-isolated elements, and are used because they provide a precise location of a photon interaction within the detector [124]. With the presently available modules, GRETINA covers one quarter of a sphere as a result of its closely-packed geometry. Figure 4.7 shows GRETINA installed in the S3 vault at the NSCL with the S800 spectrometer

during a previous experimental campaign.

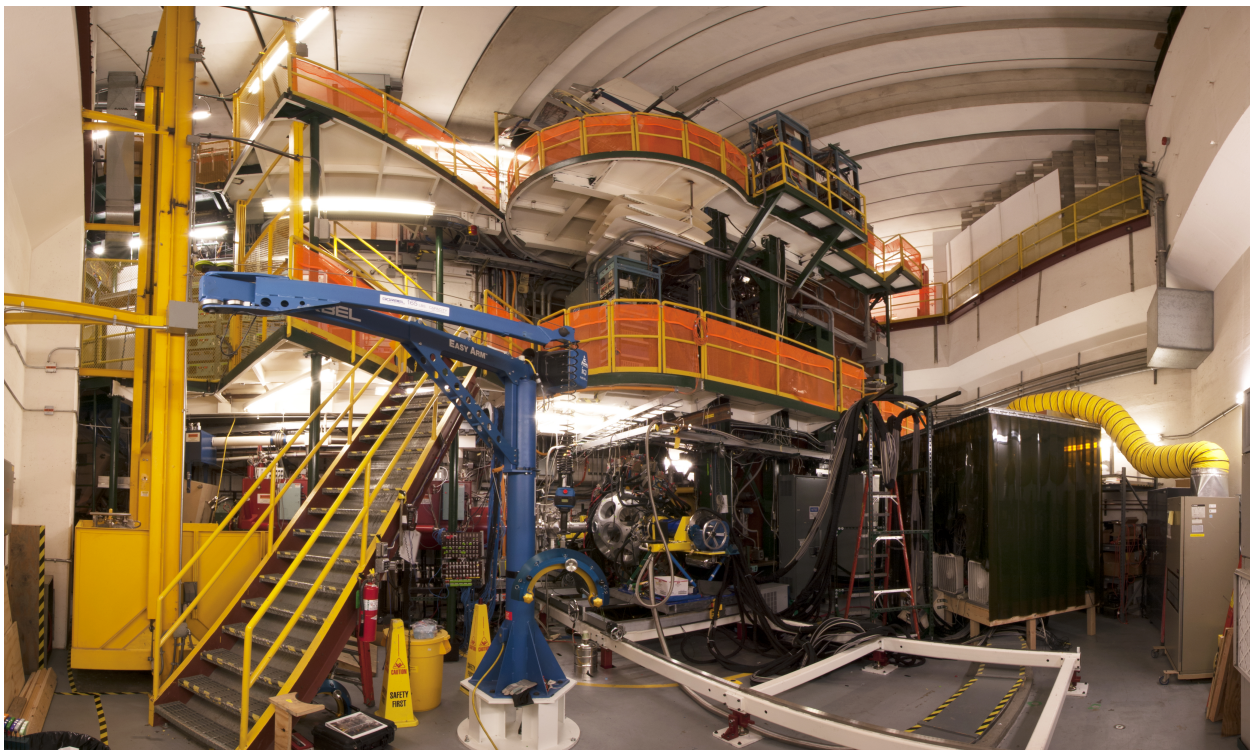

Figure 4.7: A photo of GRETINA set up with the S800 spectrometer. Photo credit to S. Noji from FRIB.

GRETINA is capable of detecting γ-rays with high resolution, and because of the segmented nature of the germanium detectors, doppler-reconstruction of events is available for in-beam spectroscopy experiments [125, 126]. In the ^{86}Kr(t,^{3}He+γ)^{86}Br experiment, no doppler-reconstruction was needed, because the interest was for γ-rays from stopped ^{86}Br or its decay products. It was expected that the Gamow-Teller strength associated with ^{86}Kr would be weak, based on the calculations presented in chapters 2 and 3. The array detects the γ-rays from the decay of the excited residual nucleus, in this case ^{86}Br, and by using these γ-rays to gate on the excitation energy spectrum, it became easier to differentiate the events from ^{86}Kr from the other events present in the spectrum. The efficiency of GRETINA was measured prior to the experiment using a ^{152}Eu source. Figure 4.8 shows the efficiency

curve obtained using these data. It is necessary to incorporate the efficiency of the detector array into the cross section for each γ-ray examined.

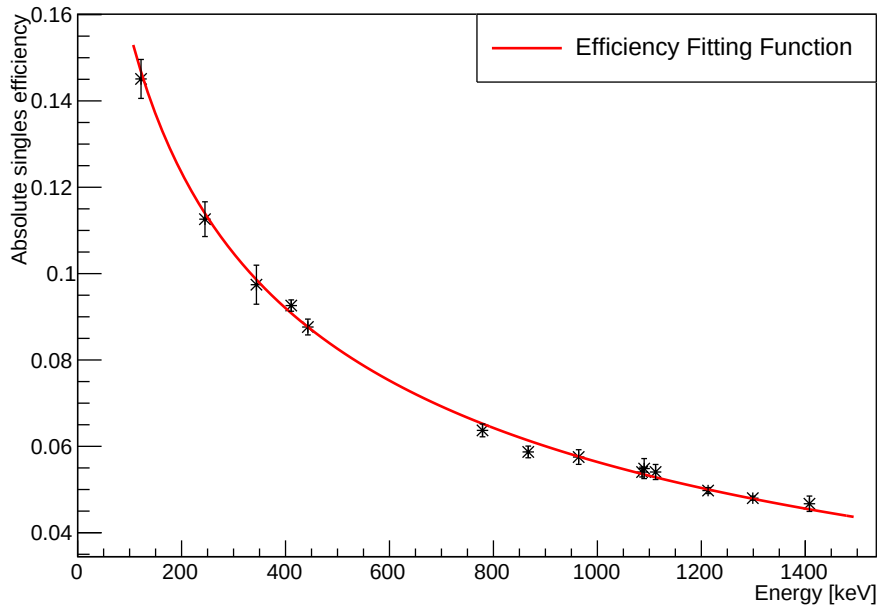

Figure 4.8: The efficiency curve of the GRETINA detector array. The ^{152}Eu data points, measured prior to the experiment, are fit with a curve so that the efficiency of the detector at all γ energies can be determined.

Using the gas target system and GRETINA in the same experiment presented a unique challenge because space around the target position is at a premium. All of the germanium crystal modules were placed in the northern hemisphere so that the southern side of the target would be clear for the gas target system, shown in the left-hand side of figure 4.9. Additionally, the target system was affixed to the beam pipe at an angle of 30 degrees from the vertical and supported by a chain hoist, shown in the left-hand picture in figure 4.9. A port was machined into the side of the beam pipe in the horizontal plane at an angle of 45 degrees from the beam axis to allow the image-intensifying camera to have a clear view of the target position. The camera was used during the secondary tuning process so that the

location and shape of the beam spot could be verified, as discussed in section 4.1.1.

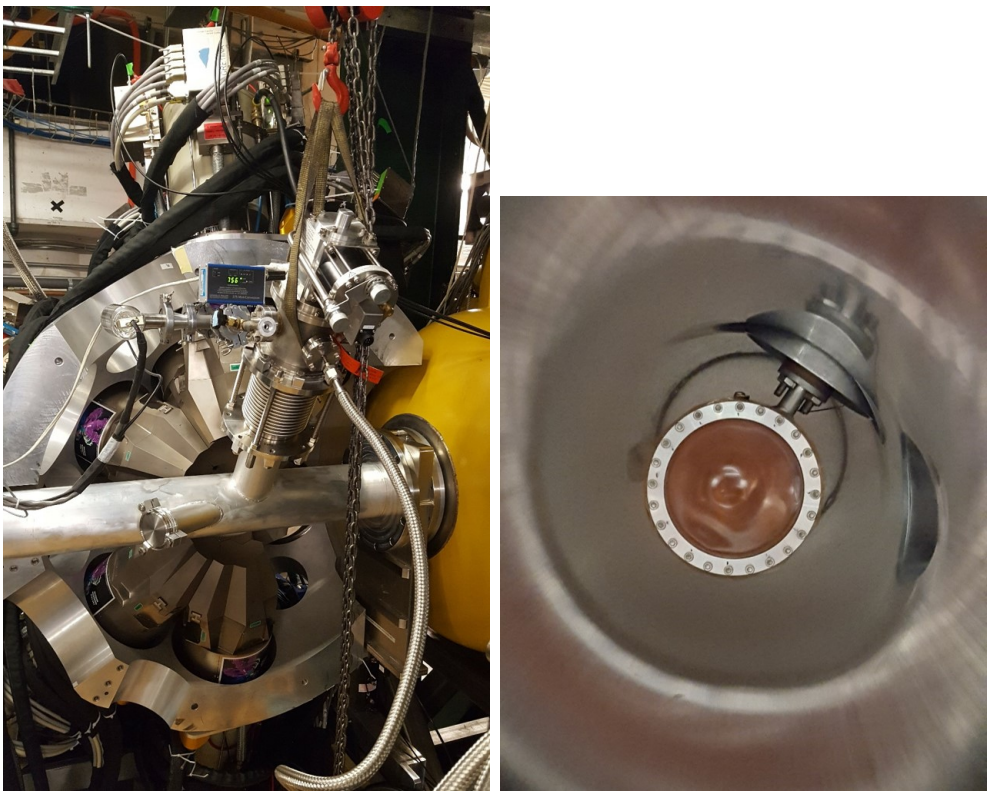

Figure 4.9: Left: Photo of the single-hemisphere GRETINA configuration with the custom beam pipe and krypton gas target system installed. Right: Photo of the krypton cell inside the beam pipe; the 30 degree angle of the target system, necessary in order to accommodate the germanium detectors, is evident.

4.2 Experimental Analysis

4.2.1 PID Calibration

The triton beam delivered to the target position could interact with several isotopes, including hydrogen, carbon, nitrogen and oxygen in the kapton target windows, and krypton when the target cell was filled. Additionally, although the experiment aimed to measure charge-exchange reactions, any type of reaction could occur between the beam and target particles,

producing many different ejectiles that traveled to the focal plane of the spectrometer. In order to select for the proper type of reaction in the analysis, the particle identification (PID) spectrum was examined. The PID was generated using the energy loss measured by the plastic scintillator in the focal plane of the S800, and the time-of-flight of the particles, calculated from the cyclotron RF and the time of a recorded hit in the spectrometer. The initial, uncorrected PID plot from this experiment is shown on the left in figure 4.10.

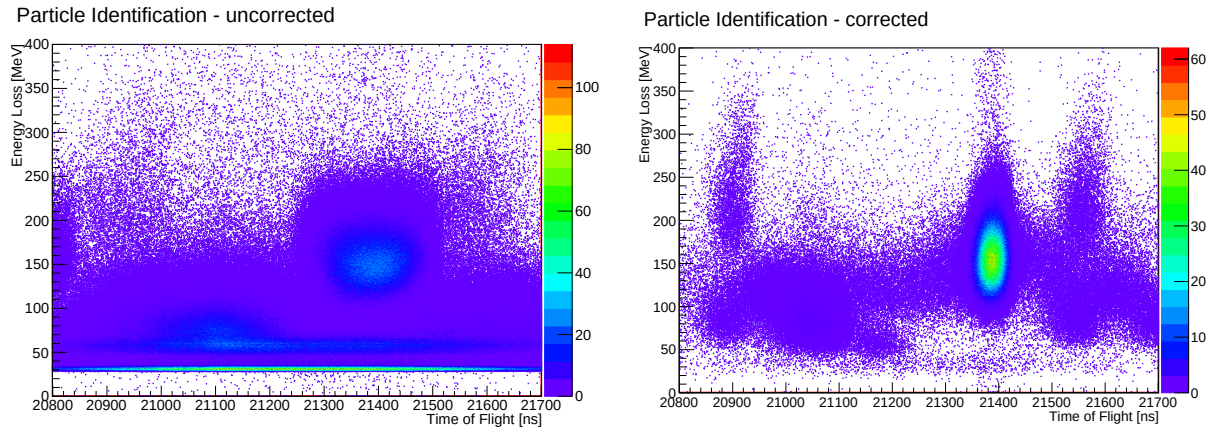

Figure 4.10: The Particle Identification plot shows the energy deposited in the plastic scintillator on the y-axis versus the time of flight of the particle on the x-axis. The large, bright spot consists of ^{3}He ejectiles from charge-exchange reactions. After applying corrections to the focal plane position, scattering angle and energy deposition, the ^{3}He spot in the PID plot is much sharper and easier to separate from the various background events.

To ensure that only the charge-exchange reactions were examined in the analysis, a gate was made on the ^{3}He ejectiles in the focal plane, shown by the bright spot in the right-hand spectrum in figure 4.10. Corrections, based on the dispersive position and angle of the particles in the focal plane, were applied to the energy loss and time-of-flight of the particles. These corrections sharpened the PID, as observed on the right in figure 4.10, improving the signal-to-noise ratio within the ^{3}He gate and reducing the number of background events present in the analysis. The gate only separated the charge-exchange reactions from the

background events, including unreacted tritons that scattered off of the S800 dipole magnets, or ejectiles from other triton reactions, such as (t,d) or (t,p), present in the spectrum [127]. A full background subtraction, to separate the ^{86}Kr charge-exchange events from the charge-exchange events on the target window nuclei, will be discussed in section 4.4.

For this analysis, the exact size and shape of the ^{3}He gate is not of great importance because of the way in which the data are normalized. Charge-exchange reactions on ^{12}C are present across all of the data, due to the kapton target windows. Because the cross section for ^{12}C(t,^{3}He) reactions is well-known, the current ^{12}C data were normalized to previous experimental data so that all of the information about the ^{3}He gate and the detector efficiency was already included in the normalization factor. Then, when the ^{86}Kr events were examined, the normalization factor was based on the previously-determined ^{12}C normalization and, therefore, included the efficiency information without requiring further analysis.

4.2.2 Mask Calibration

In order to obtain an acceptable position resolution, the position of the CRDCs in the focal plane of the S800 needed to be calibrated, because the exact location of the focal plane with respect to the rest of the experimental setup is not known. For this calibration a tungsten mask with precisely positioned holes and slits was placed in front of each CRDC in turn, while the empty target cell and viewer were situated at the target position. The mask was not thick enough to prevent ^{3}He particles from passing through. However, punching through the mask caused significant energy loss, compared to the particles that passed through one of the holes in the mask. Ejectiles continued through the focal plane to the hodoscope, placed downstream of the plastic scintillator, which measured the total remaining kinetic energy of the implanted nuclei using 32 sodium-doped cesium iodide crystals [128].

A gate was made on the hodoscope energy spectrum corresponding to the high-energy ^{3}He particles, neglecting those particles with reduced energy from passing through the mask. With this method, only the particles that passed through a hole in the mask were included in the spectrum, and the mask pattern could be seen clearly, as shown in figure 4.11. The known locations of the holes and slits in the mask were matched to the position in the CRDC spectrum, yielding calibration parameters to obtain the precise position of the ejectiles in the focal plane.

The mask runs, one each for the upstream and downstream CRDCs, were taken at the beginning of the experiment, and provided an initial calibration of the CRDC x- and y-position offsets. The non-dispersive slopes, as mentioned in section 4.1.3, were determined from the drift velocity of the electrons in the CRDCs, and could change over time. A drift velocity correction was applied on a run-by-run basis to account for these fluctuations, and will be discussed further in the next section.

4.2.3 Drift Velocity Correction

The drift velocity in the CRDCs is the speed at which free electrons travel from their point of origin to the anode wire. Because the drift velocity changed over time during the experiment, it was necessary to correct for these changes in each production run. Without these corrections, the position resolution in the focal plane is decreased and larger uncertainties would be introduced into subsequent steps of the analysis. The correction took the form of a change in the drift velocity in the non-dispersive direction; the correct velocity was determined by finding the value that placed the peak of the hydrogen kinematic curve in each spectrum at the same y-position as the first production run after the mask calibration. After these corrections were applied to each run, the peaks of the hydrogen curve are aligned, as

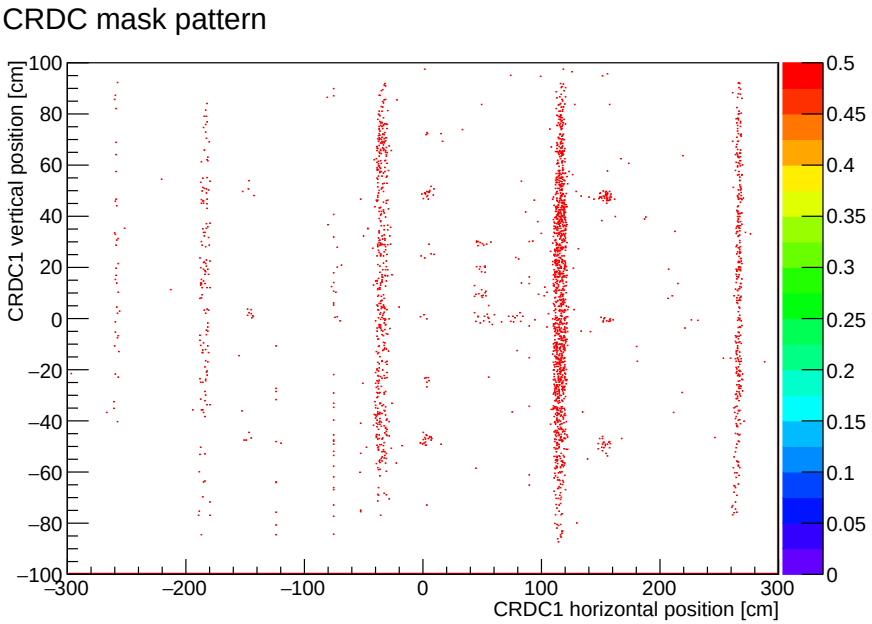

Figure 4.11: The image of the mask in the first CRDC. The positions of the holes and slits are calibrated in order to determine the exact position of the CRDC in space.

shown in figure 4.12.

4.2.4 Scattering Angle Correction

A map of the magnetic field of the S800 spectrometer was used to track particles from their position in the focal plane back to their initial location at the target position. This inverse map was generated using the ion-optical code, COSY Infinity [129]. Inputs to this code include the currents in the quadrupole and dipole magnets, the rigidity of the spectrometer, and the mass and charge of the ejectile of interest; an inversion matrix up to the fifth order was produced. Initially, the ^{3}He ejectile had an associated dispersive position (xfp), non-dispersive position (yfp), dispersive angle (afp) and non-dispersive angle (bfp) in the focal plane of the S800. A ray-tracing calculation implemented in the analysis code used these parameters, along with the magnetic field map, to determine the non-dispersive position

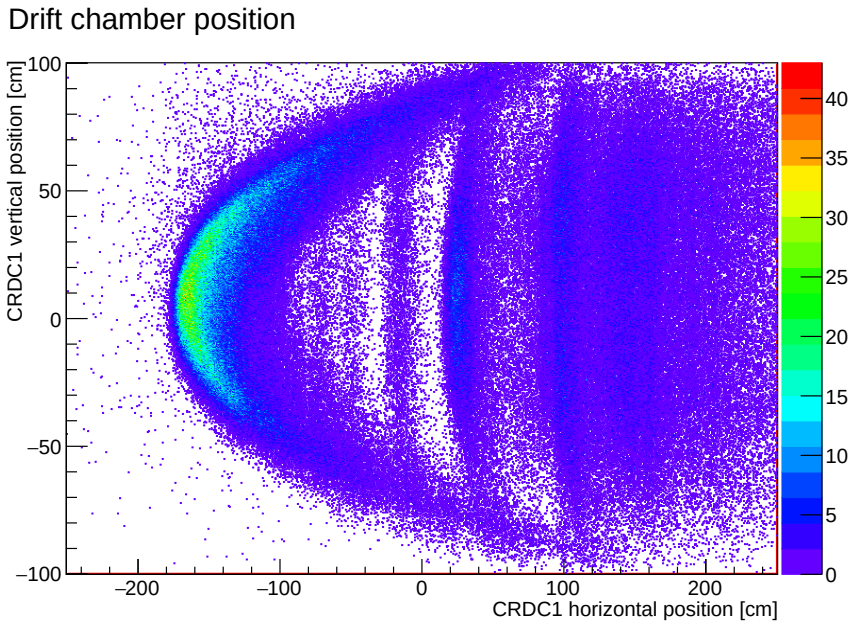

Figure 4.12: This plot shows the x- versus y-position of the ejectiles in the focal plane of the spectrometer. Because of differences in scattering energy, the ejectiles are separated by the spectrometer into a number of bands. The curved line on the left represents reactions on hydrogen nuclei; the straight lines in the middle are from reactions on carbon, oxygen and nitrogen nuclei. Any ejectiles from reactions on krypton are lost in the background at this point.

(yta), dispersive scattering angle (ata), non-dispersive scattering angle (bta) and momentum of the scattered particle (dta) at the locus of the scattering event.

Due to the size of the ^{86}Kr cell, with the target windows separated by at least 3 cm, the exact location of the scattering event, calculated via the inverse map, was impossible to resolve. The target windows were far apart and events could occur in either of them, so determining which window from which an event originated was not feasible. Instead, the inverse map was calculated using the approximate position of the center of the target cell. Because of imperfections in the ray tracing, a noticeable curve was present in the hydrogen kinematic line, shown on the left in figure 4.13. Hydrogen kinematics are shown, in this case, because the reconstruction of the excitation energy depends most sensitively on the

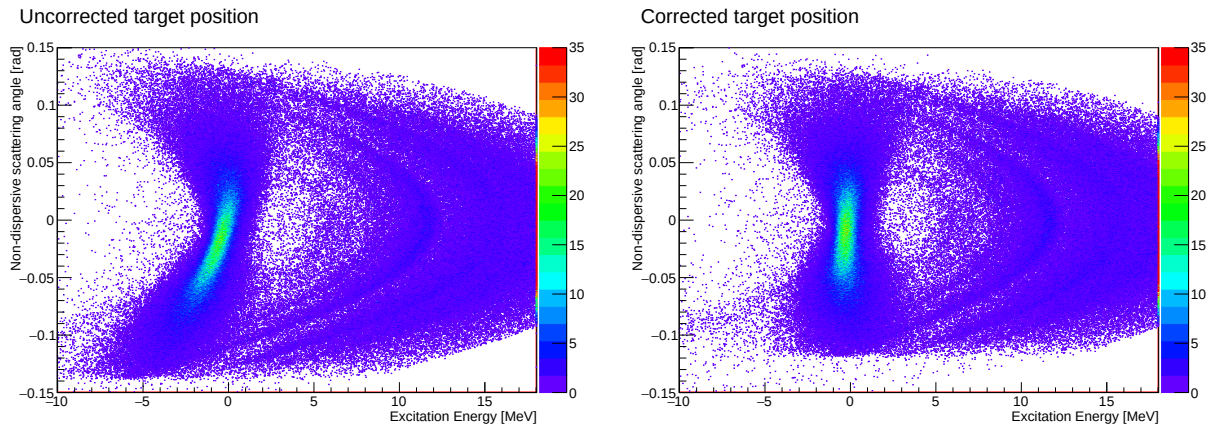

Figure 4.13: Non-dispersive scattering angle versus excitation energy. Before any scattering angle corrections are applied, as shown on the left, the hydrogen kinematic line is notably curved and offset from zero. After the angular offset was applied, along with a scaling factor, the hydrogen line is now vertical and centered on zero on the y-axis.

scattering angle, and small imperfections in the angular reconstruction strongly distort the correlation. For heavier target nuclei, such effects are less pronounced.

In these experimental data, a slight rotation was present in the non-dispersive scattering angle spectrum, which was corrected with an angular offset to the non-dispersive scattering angle to center the spectrum at 0 degrees. Then, in order to correct the curvature of the hydrogen line, a scaling factor of 0.9 was applied to the non-dispersive scattering angle. The corrected scattering angle versus excitation energy spectrum is shown on the right in figure 4.13, illustrating that the rotation in the spectrum has been corrected, and that the bright hydrogen kinematic line at 0 MeV is now centered around zero for all angles. The angular resolution of the data, with all corrections implemented, was 12 mrad (FWHM) over the range $0^{\text{o}} \leq \theta \leq 3^{\text{o}}$.

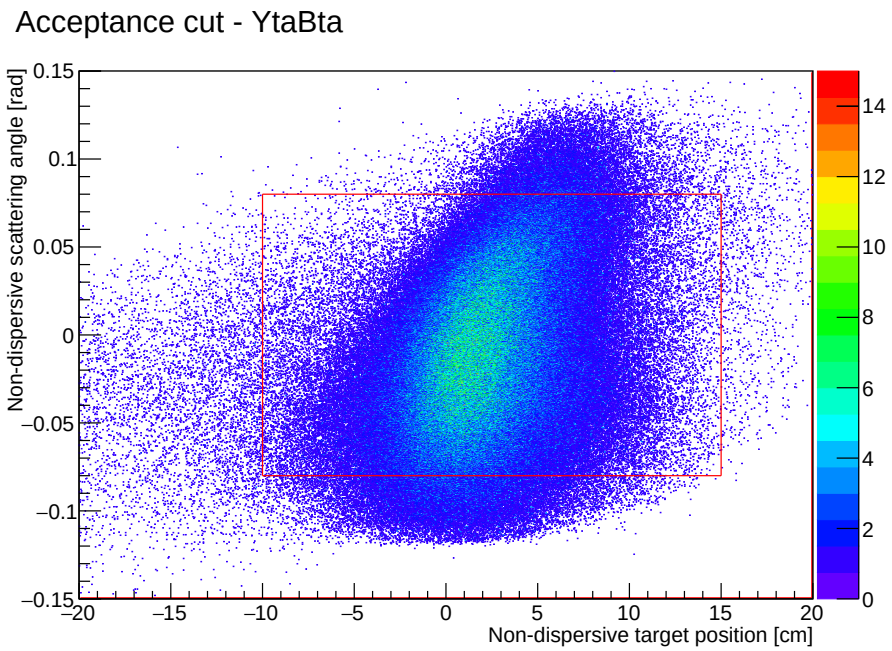

Figure 4.14: Acceptance cut in YtaBta. Non-dispersive scattering angles greater than 0.08 radians and less than -0.08 radians are excluded; beyond these angles the acceptance of the events falls off rapidly. Additionally, based on the size of the target cell, the non-dispersive target position can be restricted to a range of -10.0 mm to 15.0 mm.

4.2.5 Acceptance Correction

The acceptance of the S800 must be accounted for in the data analysis because of charge-exchange events that had large scattering angles, but that were blocked from entering the spectrometer. These events could be accounted for by weighting the data with an acceptance matrix. Figure 4.14 shows the non-dispersive scattering angle versus yta; the trend that appears between these parameters comes from correlations in the beam, as well as possible imperfections in the ray-tracing calculation. Figure 4.15 shows the dispersive scattering angle versus dta; hard cut-offs appear in this spectrum, illustrating the limits of the acceptance of the spectrometer.

The limits chosen for the acceptance (red boxes) were more restrictive than the actual cut-off of the spectrometer; this way, it was ensured that only the regions with reasonably

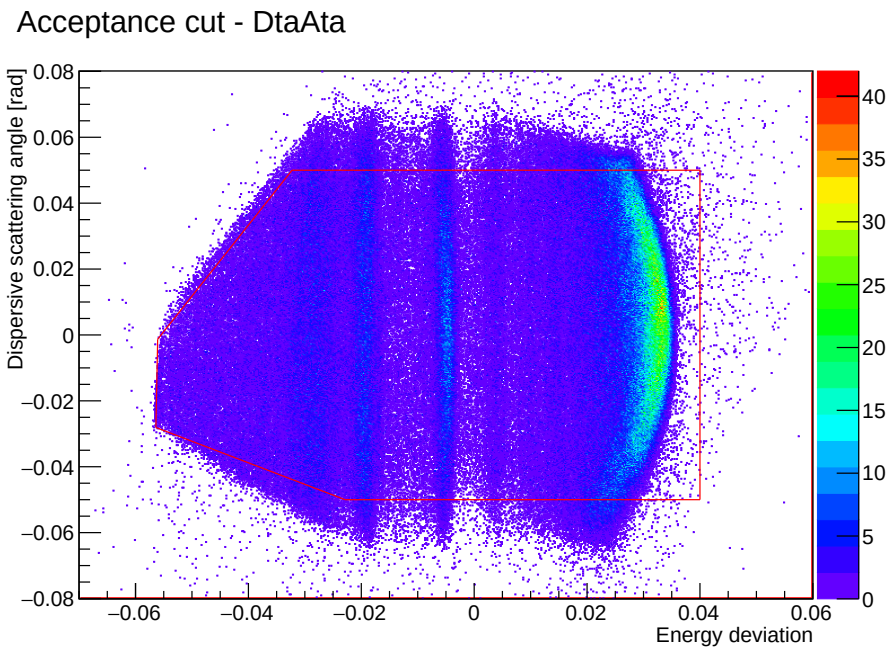

Figure 4.15: Acceptance cut in DtaAta. Dispersive scattering angles greater than 0.05 radians and less than -0.05 radians are excluded; beyond these angles the acceptance of the events falls off rapidly. The acceptance cuts are more restrictive than the shape yielded by the spectrometer because the fringe events typically require large acceptance corrections and introduce unnecessary uncertainties into the calculated cross section.

high acceptance were used in the calculation of the acceptance matrix, and included in the final analysis. While it may have been possible to loosen the restrictions on the kinematic parameters and obtain more statistics, the correction factors in the remote regions of the spectra would become large and introduce greater uncertainties into the final cross section calculation. A simple Monte Carlo simulation was used to generate the acceptance matrix, based on the presented figures. The correction factors in the matrix weight each event, taking into account the probability of that event being accepted into the spectrometer. With this method, the usable angular range was extended from 3.5 degrees to approximately 6 degrees in the laboratory frame.

Upon application of the acceptance correction to the data, it was found that there was

an asymmetry in the non-dispersive scattering angle when comparing the data from the upstream and downstream target windows, shown in figure 4.16. Such an effect was due to the acceptance being slightly different for each end of the target, meaning that events from the upstream foil had a greater acceptance than the downstream foil. The asymmetry appeared as a loss of events at large scattering angles (∼4 degrees in the center of mass frame). It was hypothesized that the asymmetry appeared because the beam was slightly offset, leading to more events from the downstream target window being cut off. Because it was not possible to correct such an effect on an event-by-event basis, it was decided that consideration of the asymmetry would be postponed until later in the analysis, where it would be negated during the target window background subtraction. As such, this issue will be discussed further in section 4.3.3.

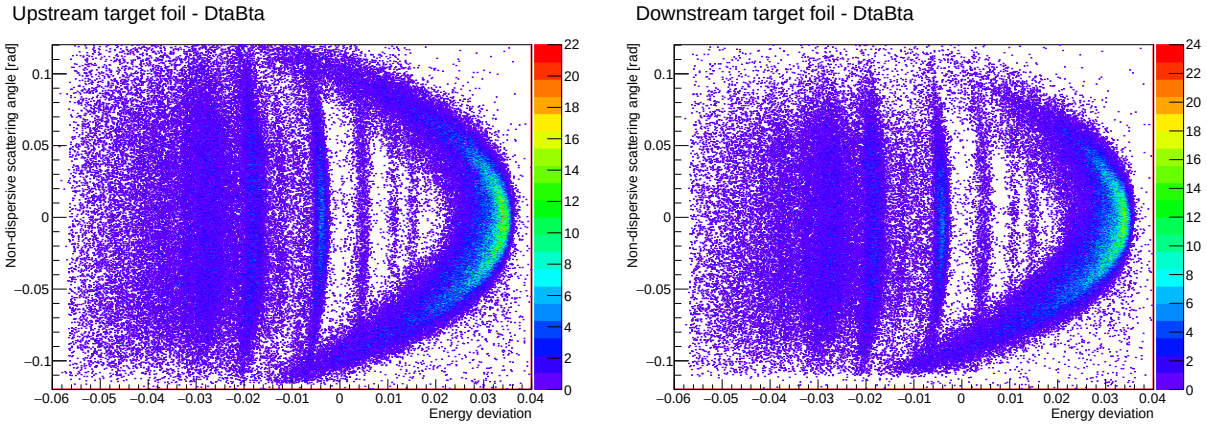

Figure 4.16: Plot of the scattering angle versus scattered energy at the target position for the upstream target foil. For the upstream foil, on left, the hydrogen kinematic line appears complete for both positive and negative scattering angles. For the downstream foil, the hydrogen kinematic line shows the loss of events for positive scattering angles, indicating a difference in the S800 acceptance when compared to the upstream foil.

4.3 Missing Mass Calculation

The excitation energy spectrum was found via a missing mass calculation, as the residual nucleus from the charge-exchange reaction was never measured. Conservation of energy and momentum were applied to the incoming energy and momentum of the projectile and the outgoing energy and momentum of the ejectile. From this, any leftover energy in the calculation was used to excite the residual nucleus. Combining this energy and momentum with the mass of the residual nucleus, m_r, the excitation energy spectrum was generated, following the expression:

$$E_x = \sqrt{E^2_{\text{missing}} - P^2_{\text{missing}}} - m_r \tag{4.1}$$

The kinematics of the missing mass calculation took into account the masses of the initial and final particles in the reaction, leading to slight differences in the position and energy spectra, depending on which target nucleus was specified. Hydrogen kinematics refers to the case in which the incoming triton interacts with a hydrogen nucleus in the target, yielding a ^{3}He ejectile and a neutron residual. Similarly, carbon kinematics refers to an interaction with a ^{12}C nucleus, yielding a ^{12}B residual, nitrogen kinematics refers to an interaction with a ^{14}N nucleus, yielding a ^{14}C residual, and krypton kinematics refers to an interaction with a ^{86}Kr nucleus, yielding a ^{86}Br residual.

The ways in which incoming tritons could interact with these nuclei are shown in figure 4.17. The left-hand figure illustrates the case of the empty target cell, which consists of two kapton windows, containing mostly ^{12}C, ^{14}N, ^{16}O and ^{1}H. Because the center of the target was at vacuum when the cell was empty, reactions could only occur in the upstream (interaction A) or downstream (interaction B) target windows. After the triton interacted with one of the windows, a ^{3}He ejectile was produced, which continued into the spectrometer.

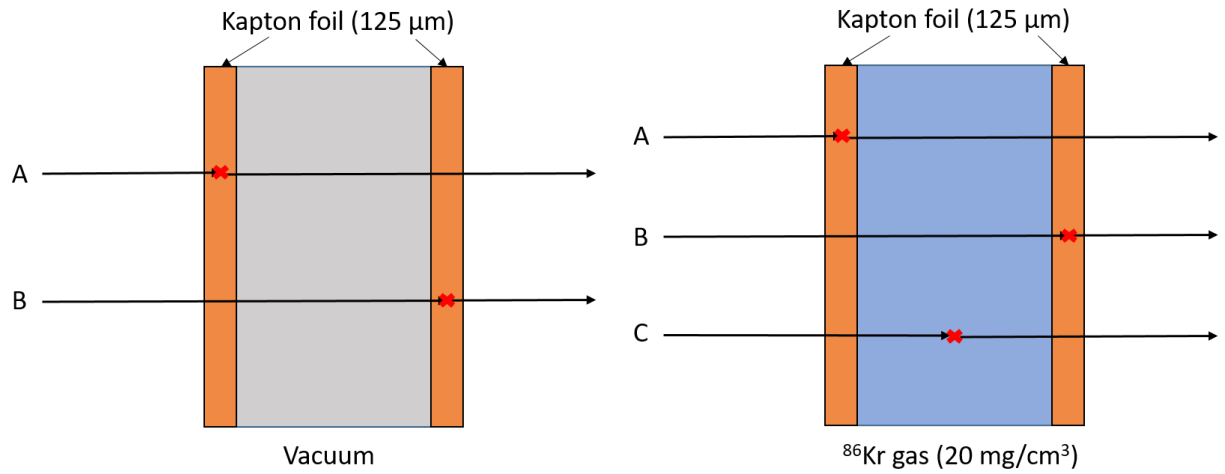

Figure 4.17: A diagram of the possible interaction with the empty target cell (left) and krypton target cell (right). With the center of the cell at vacuum, incoming tritons could interact with either the upstream (A) or downstream (B) kapton target windows. However, when the target is filled with ^{86}Kr gas. interactions may also occur in the center of the target. The thicknesses of the targets are not to scale.

When the target cell was filled with ^{86}Kr gas, as is shown on the right in figure 4.17, interactions could still occur on the target windows (A and B as described previously), but the tritons could also interact with the target gas (interaction C).

Interactions described in the case of the empty cell accounted for the peaks found in the excitation energy spectrum, shown in figure 4.18. Carbon kinematics were used to generate the spectrum, placing reactions on ^{12}C that yielded ^{12}B in its ground state at 0 MeV. Contributions from other charge-exchange reactions appear in the spectrum, based on their reaction Q-value. Table 4.1 shows the Q-values for the most common target nuclei in this analysis. For the case of carbon kinematics, the difference between the chosen nucleus' Q-value and ^{12}C Q-value yields the energy at which the reaction products begin to appear in the excitation energy spectrum.

Reactions on hydrogen (blue) and nitrogen (green) begin to appear at large negative excitation energies, because their reaction Q-values are smaller in magnitude than the ^{12}C

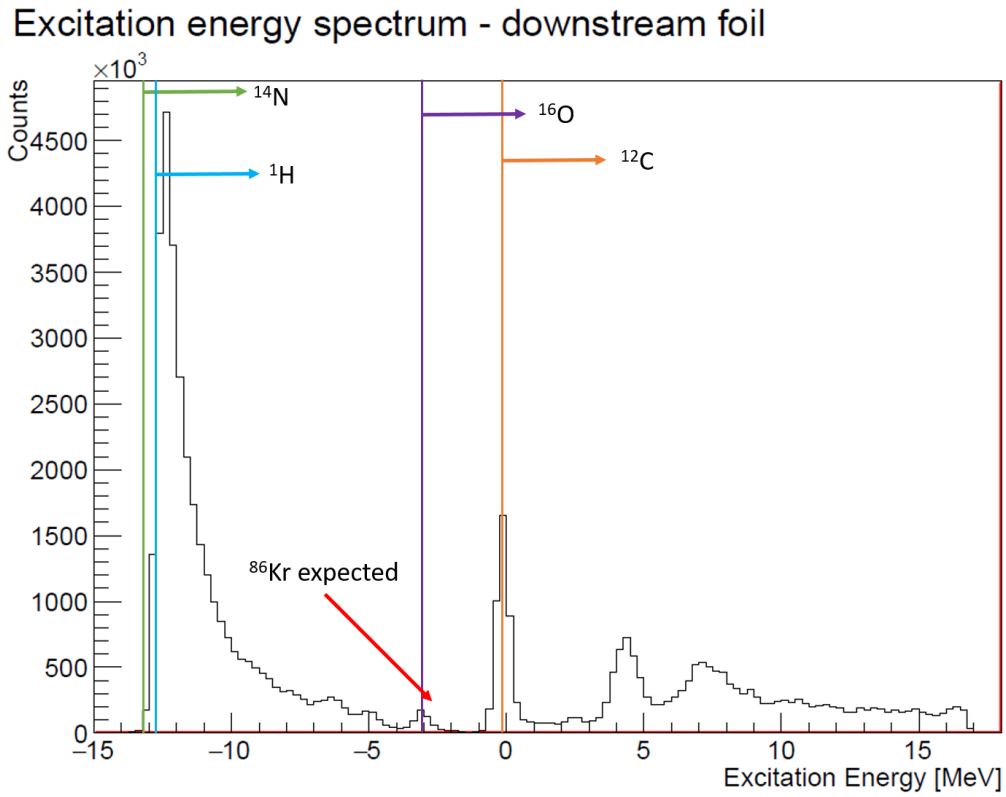

Figure 4.18: Excitation energy spectrum for the downstream target foil. This spectrum uses carbon kinematics, meaning that the peak at 0 MeV represents reactions on ^{12}C that yield ^{12}B in its ground state. The energies at which reactions on various target window nuclei begin to appear are shown. If ^{86}Kr were present, those reactions would appear at approximately -2.5 MeV in this plot.

Table 4.1: Ground state Q-value of $(t,^3\mathrm{He})$ reactions on krypton and background nuclei.

	Q-value (MeV)
^{14}N	-0.138
^{1}H	-0.764
^{86}Kr	-7.609
^{16}O	-10.402
^{12}C	-13.35

reaction Q-value. Alternatively, reactions on carbon (orange) and oxygen (purple) enter the spectrum closer to 0 MeV, because their Q-values are of similar magnitude. If the complete cell were being examined and ^{86}Kr were present in the system, those reactions would be expected to appear at approximately -2.5 MeV in figure 4.18.

Each of the kinematics settings were useful for different parts of the analysis. Because hydrogen nuclei are light, the kinematics were extremely sensitive to small changes in the scattering angle, energy and position in the focal plane. Therefore, this setting was used when determining corrections to the drift velocity in the CRDCs (section 4.2.3) and to the scattering angles (section 4.2.4).

Carbon kinematics were used because ^{12}C has been studied extensively by the charge-exchange group, and its properties and cross section are well-known. As such, the carbon cross section was used to ensure that all angular, positional and energy corrections were applied to the data appropriately. Additionally, because carbon and hydrogen were present in all data sets, due to the kapton windows of the target cell, these contributions were used to normalize the data, as will be discussed in section 4.3.2. Finally, the krypton kinematics setting was used to examine events of a triton interacting with the ^{86}Kr nucleus and yielding a residual nucleus of ^{86}Br, which was the measurement of interest, and will be discussed in more detail in sections 4.4.2 and 4.4.3.

4.3.1 Target Energy Loss

Using the fragment separator software, LISE++ [130], estimates for the energy loss experienced by tritons and ^{3}He particles as they passed through the target were obtained. In order to simplify the calculation, the interaction between the beam and the target were assumed to occur in the center of the target windows, and gas cell, when it was filled.

For the empty cell data, two scenarios for energy loss were possible. The first was the case in which the incoming triton interacted with the upstream target foil (interaction A in figure 4.17). In the first half of the first target foil, the energy loss was calculated based on a triton passing through the kapton. Then, for the last half of the upstream target window

and the entire downstream target window, the energy loss was calculated based on a ^{3}He particle moving through the target. Summing the energy loss contributions for the incoming and outgoing particles, the total energy loss for this scenario was equal to approximately 0.72 MeV.

The other scenario was the case in which the beam interaction occured in the downstream target foil (interaction B in figure 4.17). In the first target window and half of the second target window, the energy loss was calculated based on a triton moving through the kapton. After the interaction, for the final half of the downstream target foil, the energy loss was calculated based on a ^{3}He particle moving through the foil. Because energy loss within the target was dependent on the mass of the particle moving through it, this scenario produced less energy loss than the first, because much of the path was traveled by the triton. Again, summing the energy loss contribution for the incoming and outgoing particles, the total energy loss for this scenario was equal to approximately 0.39 MeV. Determining the difference in energy loss between the two scenarios yielded a value of 330 keV for the difference in the energy loss associated with the empty cell data.

A similar exercise was performed for the krypton target cell, but it was necessary to include an additional source of energy loss, as the tritons and ^{3}He particles passed through ^{86}Kr gas instead of vacuum, causing them to lose more energy as they traveled through the target. In order to obtain the energy resolution for the krypton data, the energy losses yielded from interactions A and B were used. With the addition of the krypton gas, the energy loss associated with the interaction in the upstream target window and in the downstream target window were equal to 1.06 MeV and 0.47 MeV, respectively. From these values, the difference in the energy loss associated with the data obtained from the filled krypton cell was 590 keV.

It is also important to obtain a measure of the energy resolution for the experiment. The

^{12}C peak present at 0 MeV in figure 4.18 was used to determine that the energy resolution for the carbon events was approximately 575 keV (FWHM) in the range 0 MeV $\leq$ E$_x$ $\leq$ 20 MeV. For the krypton events the calculation of the energy resolution was more difficult, because there were no obvious ^{86}Kr peaks in the excitation energy spectrum, so that simply measuring the width of the distribution was not possible. Instead, the coincidence data were used; by gating on known ^{86}Be γ-rays an excitation energy spectrum for ^{86}Kr events was obtained (see section 4.7 for the details of this process). The energy resolution for the krypton data was approximately 400 keV (FWHM) in the range 0 MeV $\leq$ E$_x$ $\leq$ 5 MeV.

4.3.2 Cross Section Calculation

The cross section of a reaction is a measure of the likelihood of the reaction occurring at a particular excitation energy. In order to convert the cross section from counts measured in the detector to the proper units of a differential cross section, the acceptance and geometry of the system were taken into account. The expression for the cross section for the ^{86}Kr(t,^{3}He+γ) experiment is as follows:

$$\frac{d\sigma}{d\Omega} = \frac{Y}{N_b N_t d\Omega \epsilon_1}. \tag{4.2}$$

Here, Y is the absolute yield of the reaction of interest, N_b is the number of particles in the beam, N_t is the number of particles in the target, dΩ is the solid angle and ϵ_1 is the acceptance of the S800 for a particular target position, scattering energy and scattering angle bin from the acceptance matrix. The solid angle, which describes the area subtended by the cone formed by the azimuthal scattering angle, is given by $d\Omega = \sin\theta d\theta d\phi$. For small scattering angles, there are no limitations on the polar angle, ϕ. However, as the scattering angle increases, some events begin to be blocked from entering the spectrometer,

leading to restrictions on the polar angle; the loss of these events is taken into account with the acceptance correction, detailed in section 4.2.5. Angular bins for the cross section were chosen to be 1 degree in the center of mass frame.

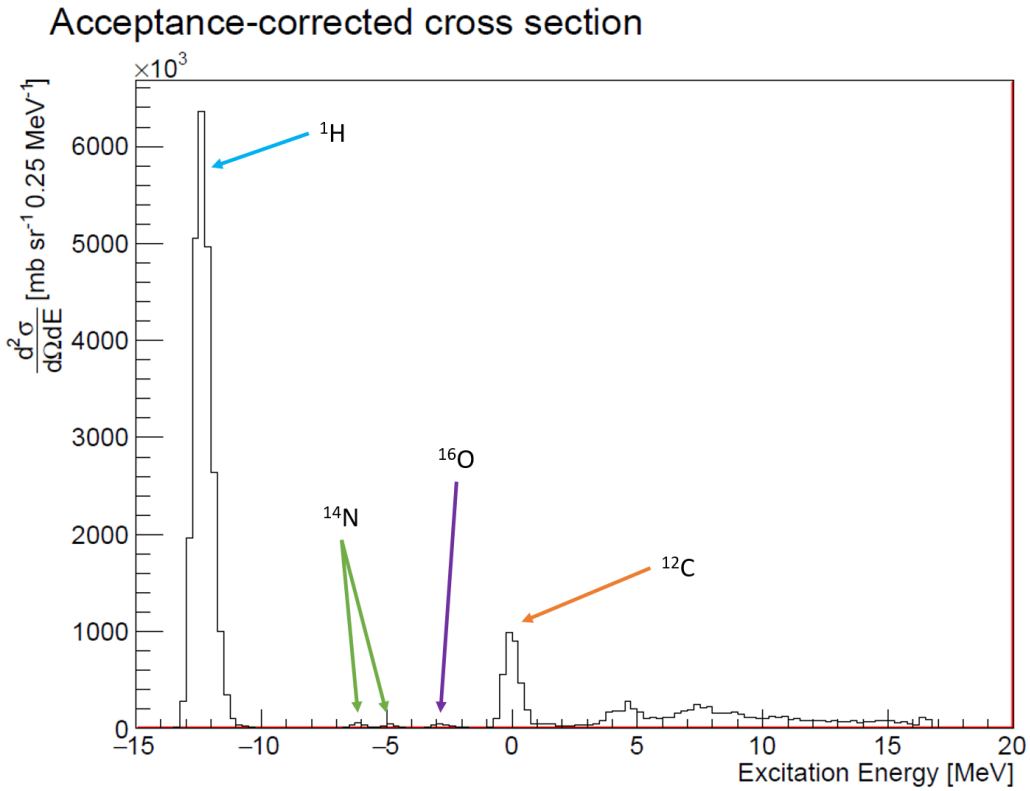

Figure 4.19: Cross section for reactions on the empty target cell for the 0 to 1 degree angular bin, corrected for the acceptance of the spectrometer. Reactions on the carbon ground state sit at 0 MeV, due to the use of carbon kinematics in this calculation. The contribution from hydrogen reactions are at negative excitation energies. These contributions need to be subtracted from the krypton data in order to see the underlying reactions of interest.

The cross section for the empty target cell in carbon kinematics for an angular range of 0 to 1 degrees is shown in figure 4.19; all contributions to this spectrum come from reactions on nuclei in the target windows. The large hydrogen peak appears at negative excitation energies because the Q-value for reactions on hydrogen is much smaller than the Q-value for reactions on carbon. At higher excitation energies, the peaks correspond to reactions

on carbon, oxygen and nitrogen, which were also present in the target windows. Because the signals from reactions on hydrogen and carbon were strong, it was necessary to subtract these and other target window reaction contributions from the krypton data set in order to observe the cross section of reactions on ^{86}Kr.

4.3.3 Carbon Angular Distribution

After the cross section calculation was finalized, it was possible to extract an angular distribution from the data. Initially, the angular distribution of the carbon ground-state peak was examined because the carbon data were used to normalize the remainder of the data and to obtain an estimate of the beam intensity. It was possible to obtain reasonable cross section measurements up to about 6 degrees in the center of mass frame, at which point the carbon and hydrogen peaks began to overlap, as was illustrated in figure 4.16.

The angular distribution for the carbon data from the empty cell runs is shown in figure 4.20, along with a comparison to a DWBA calculation and ^{12}C experimental data from previous experiments [116, 131]. A scaling factor was applied here, which is equivalent to the luminosity, $\frac{1}{N_b N_t}$, from equation 4.2. Using this normalization factor, the average beam intensity, N_b, for the experiment was extracted and found to be approximately 5×10^6 particles per second, which is the typical intensity for a triton beam at the NSCL.

Because, as mentioned previously (figure 4.16), the target cell was thick, it was necessary to examine the angular distributions from both the upstream and downstream target windows, in order to determine whether the acceptance was treated properly for each of the target windows. The extracted angular distributions for both foils is shown in figure 4.21. Prior to the acceptance corrections, with increasing scattering angle, the angular distribution from the downstream window was less than the angular distribution from the upstream win-

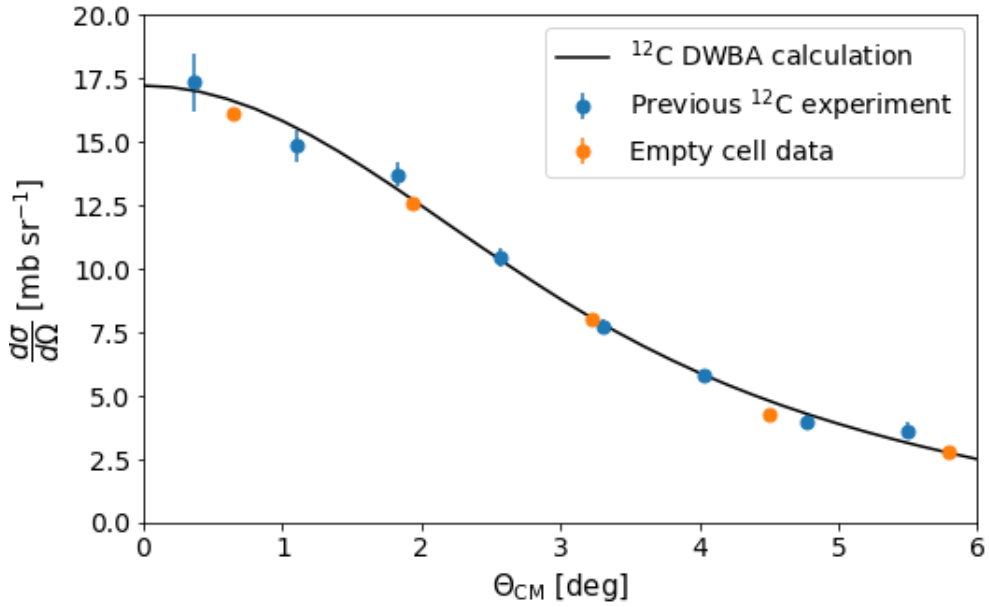

Figure 4.20: A comparison the angular distribution of the carbon ground state with past experimental data. The agreement between the blue points (past experiment [116, 131]) and the orange points (current data) indicates that the calibrations and corrections applied to the data have been successful in replicating this known angular distribution.

dow by about 25%. This phenomenon was due to events from the upstream target window having a larger acceptance than those from the downstream window, as was mentioned in section 4.2.5.

The downstream target window, which had a smaller acceptance, had fewer events successfully entering the spectrometer, causing a smaller yield to be measured. To correct this, the ratio between the cross section from the downstream and upstream windows was taken for each angular bin, quantifying the magnitude of the asymmetry; it was found that the effect became more pronounced with increasing scattering angle. Then, a scaling factor was applied to each angular bin of the downstream cross section, such that the asymmetry was corrected, and the ratio between the upstream and downstream angular distributions was equal to 1. With the asymmetry taken into account in the data processing, the angular dis-

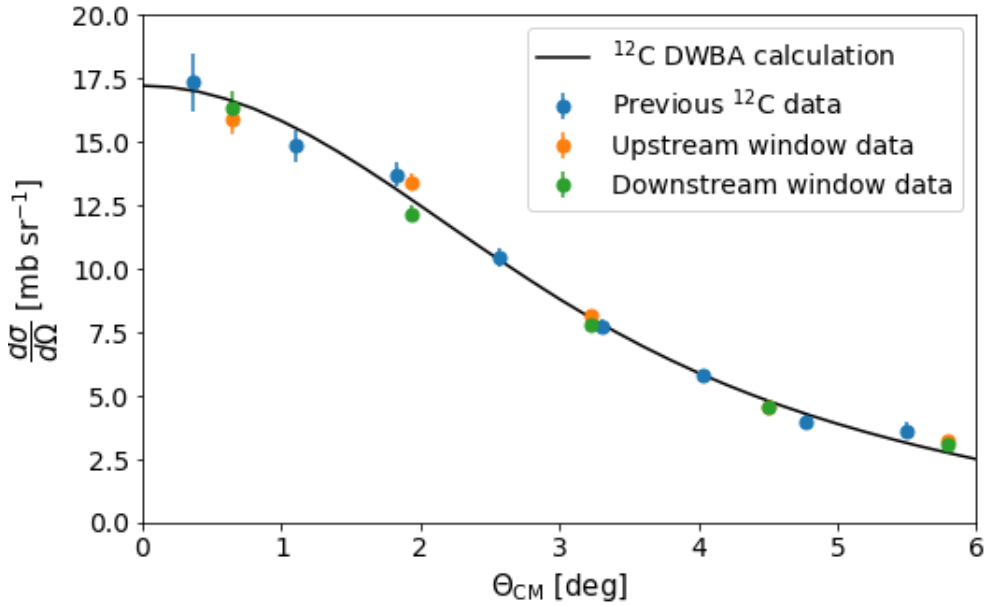

Figure 4.21: A comparison the angular distribution of the carbon ground state, derived from the upstream (orange points) and downstream (green points) target foils. After correcting for the difference in the acceptance for each target window, both contributions match the previously-extracted ^{12}C angular distribution [131, 116].

tributions from each target window were consistent with the ^{12}C angular distribution from previous experiments, indicating that the corrections and calibrations for these experimental data were reasonable.

4.3.4 Nitrogen Angular Distribution

Also present in the data set were charge-exchange reactions on ^{14}N. As marked in figure 4.19, these events mainly appeared at small negative excitation energies in carbon kinematics. Zooming in on the excitation energy spectrum, the ^{14}N events are shown in the top plot in figure 4.22. The events of interest appear in the peaks at 7 MeV and 8.5 MeV; the third peak shown in the figure is composed of events on ^{16}O.

Following the same procedure as the ^{12}C analysis, and angular distribution was extracted

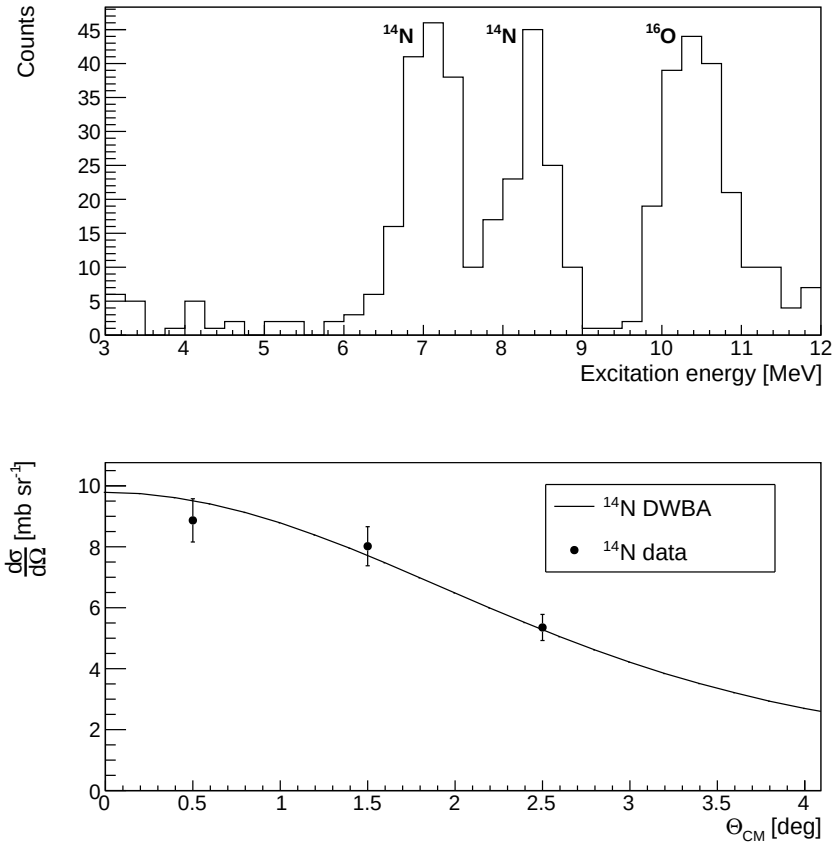

Figure 4.22: Excitation energy spectrum from the empty cell data, zoomed in on the region containing ^{14}N events. The ^{14}N events of interest are in the peaks at 7 MeV and 8.5 MeV. The third peak on the right is composed of ^{16}O events.

for the ^{14}N data, and is shown in the bottom plot of figure 4.22. Comparing the extracted angular distribution to the DWBA calculation (black line), it is clear that there is good agreement between the shape of the experimental distribution and the theoretical result. Using the well-known proportionality between the charge-exchange cross section and the Gamow-Teller strength, as presented in equation 3.19, the strength distribution for the ^{14}N events was extracted. The DWBA calculation was used to extrapolate the experimental angular distribution to $\Theta = 0$, and the unit cross section, $\widehat{\sigma}$, was obtained using the empirical expression dependent on the mass number (equation 4.7).

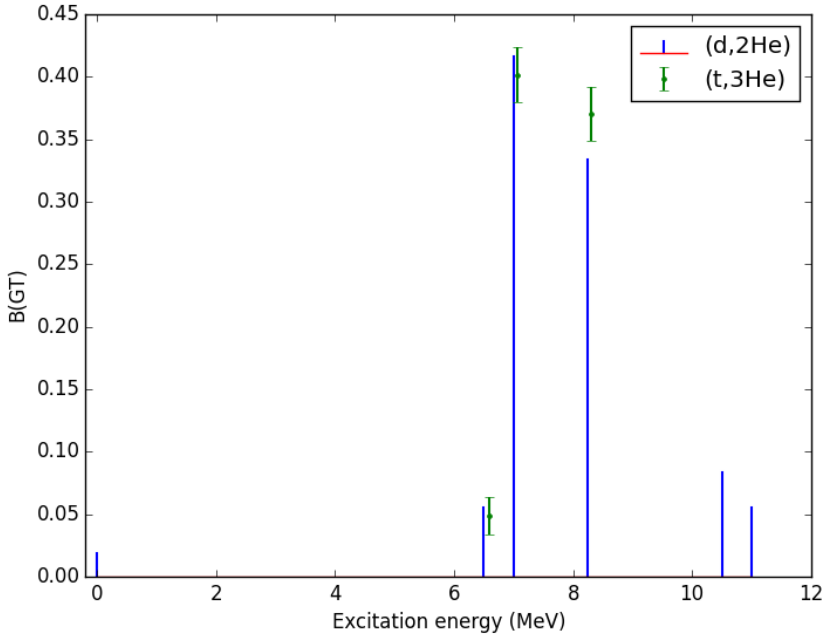

Figure 4.23: ^{14}N Gamow-Teller strength distribution, compared to experimental (d,^{2}He) data [132]. No error bars were presented with the (d,^{2}He) data.

Figure 4.23 shows the calculated Gamow-Teller strength distribution (green points). Also shown in blue is a previous measurement of the ^{14}N Gamow-Teller strength using the (d,^{2}He) reaction [132]. It is shown that there is good agreement between the experimental data from this work, and from the (d,^{2}He) experiment. Such a result indicates that the current calibrations and experimental analysis are reasonable up to this point, as both the ^{14}N data, here, and the ^{12}C data in section 4.3.3, match previously published results, within experimental uncertainties.

4.4 Target Window Event Subtraction

The experimental data runs intended to measure events on ^{86}Kr also contained events from the kapton target windows. Because the krypton signal was weak, however, it was hidden

underneath the extraneous events from hydrogen, carbon, nitrogen and oxygen. The Q-values for all expected reactions are presented in table 4.1. The energies of the lowest-lying states for ^{12}B, ^{14}C and ^{16}N are shown in tables 4.2, 4.3 and 4.4, respectively. The energies are also converted to the excitation energy in ^{86}Br, in order to determine where those states would appear when analyzing the spectrum using krypton kinematics. Because the ^{86}Kr signal was expected to appear at approximately 2.5 MeV, it is clear that mainly events from ^{14}N and ^{16}O were located at the same energy as the krypton.

Table 4.2: Location of states in ^{12}B [133], converted to ^{86}Br excitation energy.

	Excitation energy in ^{12}B [MeV]	Excitation energy in ^{86}Br [MeV]
0	0.0	5.74

Table 4.3: Location of states in ^{14}C [134], converted to ^{86}Br excitation energy.

	Excitation energy in ^{14}C [MeV]	Excitation energy in ^{86}Br [MeV]
0	0.0	-7.48
1	6.09	-1.38
2	6.59	-0.89
3	6.73	-0.75
4	7.01	-0.47
5	7.34	-0.14
6	8.31	0.84
7	9.75	2.27
8	9.80	2.32
9	10.43	2.95
10	10.45	2.97
11	10.50	3.02
12	10.74	3.26
13	11.31	3.83
14	11.40	3.92
15	11.50	4.02
16	11.67	4.19
17	11.73	4.25
18	11.90	4.42
19	12.58	5.11

Table 4.4: Location of states in ^{16}N [135], converted to ^{86}Br excitation energy.

	Excitation energy in ^{16}N [MeV]	Excitation energy in ^{86}Br [MeV]
0	0.0	2.81
1	0.12	2.93
2	0.30	3.10
3	0.40	3.20
4	3.34	6.14

Although it was unfortunate that the target window events were numerous compared to the krypton signal, the background spectrum was uniform across all data runs, so it was a simpler process to normalize and subtract it away. During the beam time, it was determined that simply taking data using the empty gas cell would be insufficient to model the background signal, due to the thickness of the target and the uncertainties in the energy loss in the target windows. Therefore, additional data sets were taken, one set with only the upstream target window present, and one set with only the downstream target window in place, for use in developing a model of the target window events.

4.4.1 Empty Cell Subtraction

By combining the single-target-window data sets, it was possible to reconstruct the target window event spectrum and to subtract it from the krypton data set. This method was first tested with the empty cell data to verify that it would work as expected. The average energy loss of a triton or ^{3}He passing through a target foil caused a shift in the location of the cross section peak. Calculated for both of the target windows, the shift was applied to each of the foils respectively, in order to align the spectrum with the empty cell data. Additionally, the scattering angle and excitation energy were smeared for each target window spectrum, to account for energy straggling and differences in the energy resolution.

The equation for the smeared excitation energy is given by the following expression:

$$Ex_{\text{smeared}} = E_x + A\sigma_E + \Delta E \tag{4.3}$$

where σ_E is the energy straggling due to the target foil, ΔE is the energy loss in the foil, and A is a random number generated from a gaussian distribution. A similar expression was used to smear the scattering angle:

$$\Theta_{\text{smeared}} = \Theta + B\sigma_\Theta \tag{4.4}$$

where σ_Θ is the angular straggling imparted upon the particle traveling through the target foil, and B is another random number generated from a gaussian distribution. The energy loss and energy straggling values necessary for the analysis were determined based on figure 4.17, along with the energy loss discussion presented in section 4.3.1. A compilation of energy loss and angular smearing values used for both the empty cell and krypton cell subtractions, generated by the fragment separation software, LISE++ [130], is found in table 4.5.

Table 4.5: Energy loss and angular smearing values for the empty cell and krypton cell subtraction analysis. ΔE represents the energy loss correction between the two target foils. σ_E represents the energy loss correction due to straggling within the target foils. σ_Θ is the scattering angle smearing due to the target foils.

	Reaction in:	ΔE (MeV)	σ_E (MeV)	σ_Θ (mrad)
Empty cell	Upstream foil	0.443	0.0598	0.658
	Downstream foil	0.111	0.0294	0.329
Krypton cell	Upstream foil	0.7787	0.0993	1.480
	Downstream foil	0.1949	0.0496	0.741

After these modifications were applied, a composite cross section was generated by summing the cross sections for the upstream (red) and downstream (blue) foils. Subtracting this

constructed cross section from the empty cell cross section (black line) yielded a spectrum that was consistent with 0, as shown in the bottom plot of figure 4.24; the 1-2 degree bin is presented here, but similar results are obtained for all of the angular bins up to 4 degrees in the center of mass frame. From this comparison, it is clear that the cross section obtained from the background modeling procedure was equivalent to the empty cell cross section, within the experimental uncertainties.

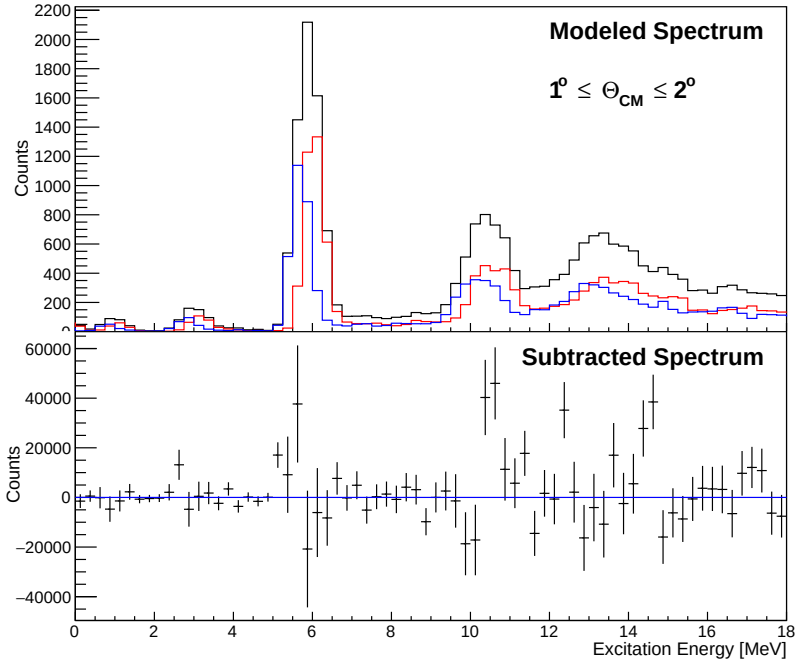

Figure 4.24: Empty cell subtraction for the 1-2 degree bin. The contributions from the upstream and down stream target windows are shown in red and blue, respectively, in the top plot. By subtracting the model spectrum from the empty cell data (black line), the bottom spectrum is obtained. The spectrum is consistent with zero (blue horizontal line) indicating that the target window events were subtracted successfully.

From the results shown in figure 4.24, it was illustrated that it was possible to perform a successful subtraction by summing the cross sections of the upstream and downstream target foils, along with a treatment of energy loss and energy straggling in the windows, in order to recreate the complete empty cell cross section. For reasons discussed in the next section,

only the data below 5 MeV were used for the krypton analysis. Referring again to tables 4.2, 4.3 and 4.4, it is apparent that, within the 5 MeV window, it was mainly events on ^{14}N that sat atop the ^{86}Kr signal. ^{12}C states do not appear until higher excitation energies and there is a gap in the ^{16}O states where the krypton signal was expected to appear.

4.4.2 Krypton Cell Subtraction

Following the technique of the empty cell subtraction, the target window events were then subtracted from the krypton data. Different energy loss parameters were used for the krypton cell subtraction because of the additional energy loss introduced by the presence of the ^{86}Kr gas. Additionally, the new parameters took into account the outward bulging of the target windows due to the internal gas pressure of the cell. Because this phenomenon introduced a position-dependent target thickness, the thickness of the ^{86}Kr portion of the target was modified until the cross section spectra from the background model matched those of the experimental data, in order to generate an accurate model of the target window events. The energy smearing parameters (equation 4.3) used for the krypton subtraction are shown in table 4.5, and were calculated using an average target thickness of 20 mg/cm^2.

The cross section for the 1-2 degree angular bin is shown in figure 4.25, for excitation energies from 0 to 20 MeV. The top figure shows krypton data (black) and the modeled target window event spectrum (red); then, the krypton cross section, obtained by subtracting the two histograms, is shown in the bottom figure. It is clear that the uncertainties in the parameters used for the subtraction procedure introduced systematic uncertainties into the subtracted spectrum. Therefore, the subtracted spectra were generated for a series of choices of the energy loss parameters, in order to estimate these systematic errors. From this study, the total systematic uncertainty for the subtraction procedure was estimated to be 25% of

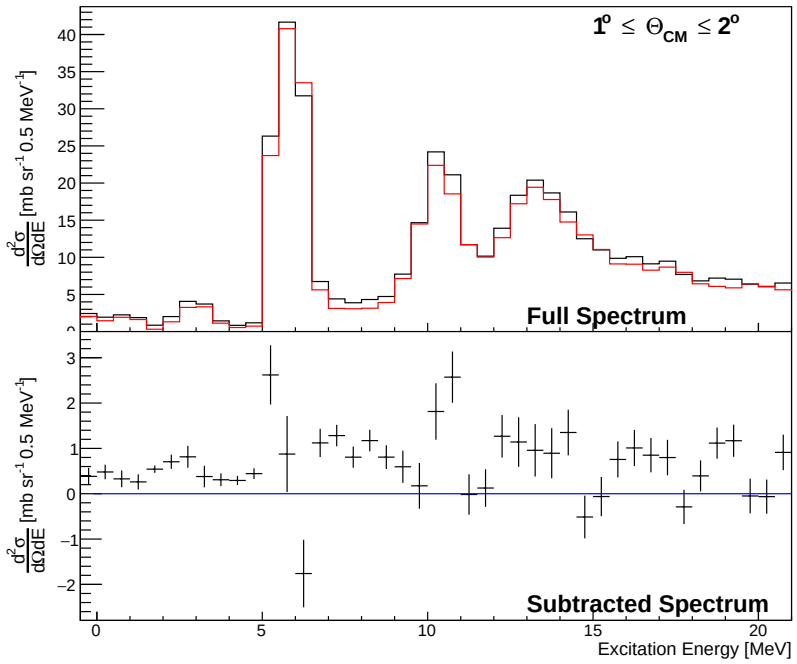

Figure 4.25: Differential cross section before (top) and after (bottom) the target window events were subtracted for the 1 to 2 degree angular bin. The bottom plot shows the extracted krypton cross section.

the total cross section, and was incorporated into the remainder of the analysis. It was concluded that above 5 MeV, the systematic errors in combination with the poor signal-to-noise ratio, and therefore, high statistical errors, made it difficult to extract reliable results for ^{86}Kr.

The absolute cross section, presented in figure 4.26 for each of the angular bins, was obtained by applying a normalization factor after the target window event subtraction. Before the subtraction, the data were corrected for the acceptance of the spectrometer, and the modeled spectra were normalized to the krypton data set using the number of counts within the hydrogen peak. To determine the overall normalization, the well-known magnitude of the ^{12}C(t,^{3}He) cross section [131] was used, because events on carbon nuclei were present across the entire data set. The scaling factor needed to match the magnitude of

the present ^{12}C cross section to the known value was extracted. Then, combining this factor with the target thickness and the molar mass of ^{86}Kr yielded the factor needed to normalize the entire krypton data set. The subtracted and normalized spectra for each of the angular bins, up 4 degrees in the center of mass frame, are shown in figure 4.26 with error bars that include both statistical and systematic uncertainties.

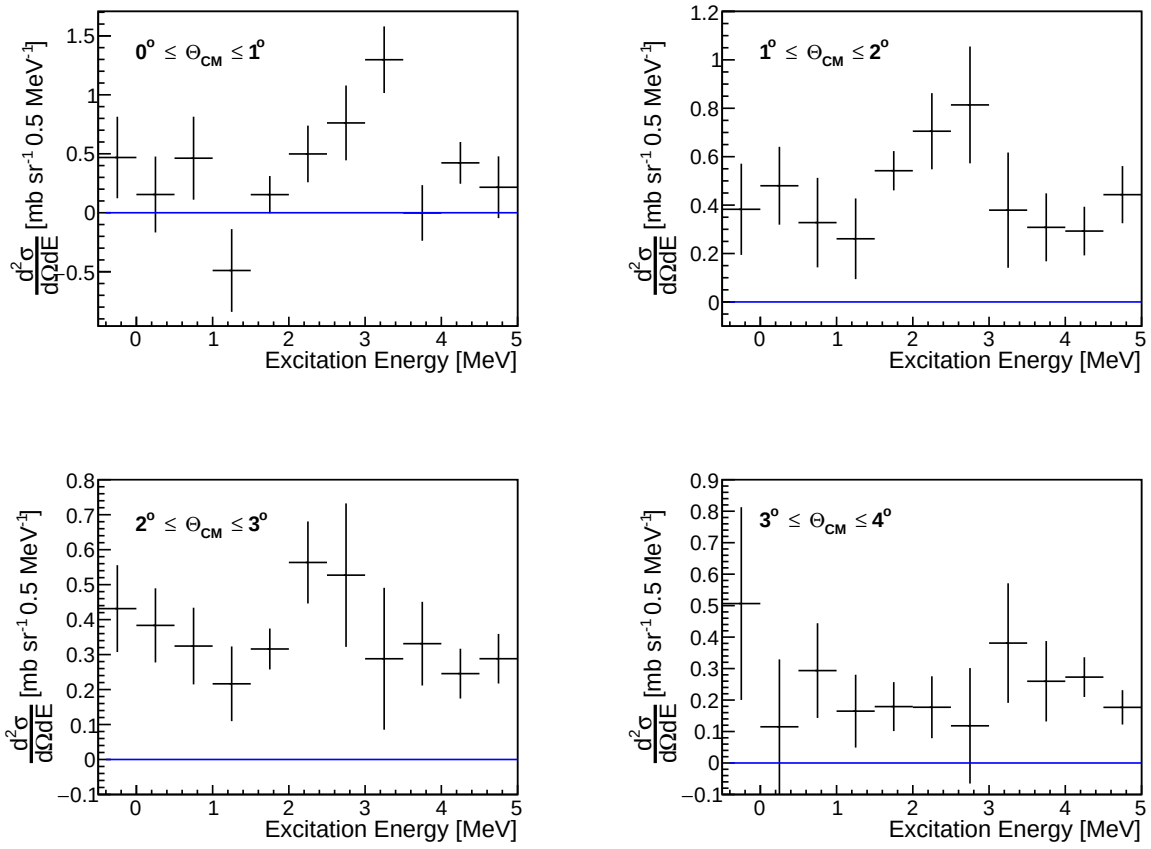

Figure 4.26: Krypton cross section with target window background events subtracted following the method detailed in section 4.4. The absolute normalization factor was obtained by comparing the carbon cross section measured in this experiment with the ^{12}C cross section obtained in previous work [131]. Scattering angles from 0 to 4 degrees in the center of mass frame are shown, as the background subtraction began to break down at larger angles. The error bars on the data are a combination of statistical and systematic uncertainties.

Target window contaminants, including ^{12}C and ^{16}O, began to appear with greater mag-

nitude at 5 MeV of excitation energy; see figure 4.18, and tables 4.2 and 4.4, for the location of the ^{12}C and ^{16}O events in krypton kinematics. The presence of these additional contributions to the cross section yielded large systematic and statistical uncertainties in the spectra after the event subtraction was completed. Therefore, as was mentioned in relation to figure 4.25, it was decided that further experimental analysis would be performed only on the data up to 5 MeV. Additionally, because the background subtraction began to break down at larger scattering angles, due to the presence of hydrogen events in the spectrum, angles above 4 degrees were also omitted from the analysis.

4.4.3 Krypton Angular Distributions

Using the normalized cross sections presented in section 4.4.2, an angular distribution was extracted for each energy bin; these spectra are shown in figure 4.27 in 0.5 MeV energy bins up to an excitation energy of 5 MeV. A Gamow-Teller transition yields a forward peaking angular distribution. Despite the large error bars shown, there are some bins that might contain a Gamow-Teller transition component, for example, the 2.5 to 3.0 MeV bin. A further examination of this possibility will be discussed in section 4.6, with the multipole decomposition analysis.

4.5 DWBA

Distorted-Wave Born Approximation (DWBA) calculations, performed using the FOLD software package [102], were initially discussed in a theory context in section 3.2. In terms of the experimental analysis, DWBA calculations had two purposes. The first was to obtain the shape of the angular distributions of the three dominant multipoles, which were then used in

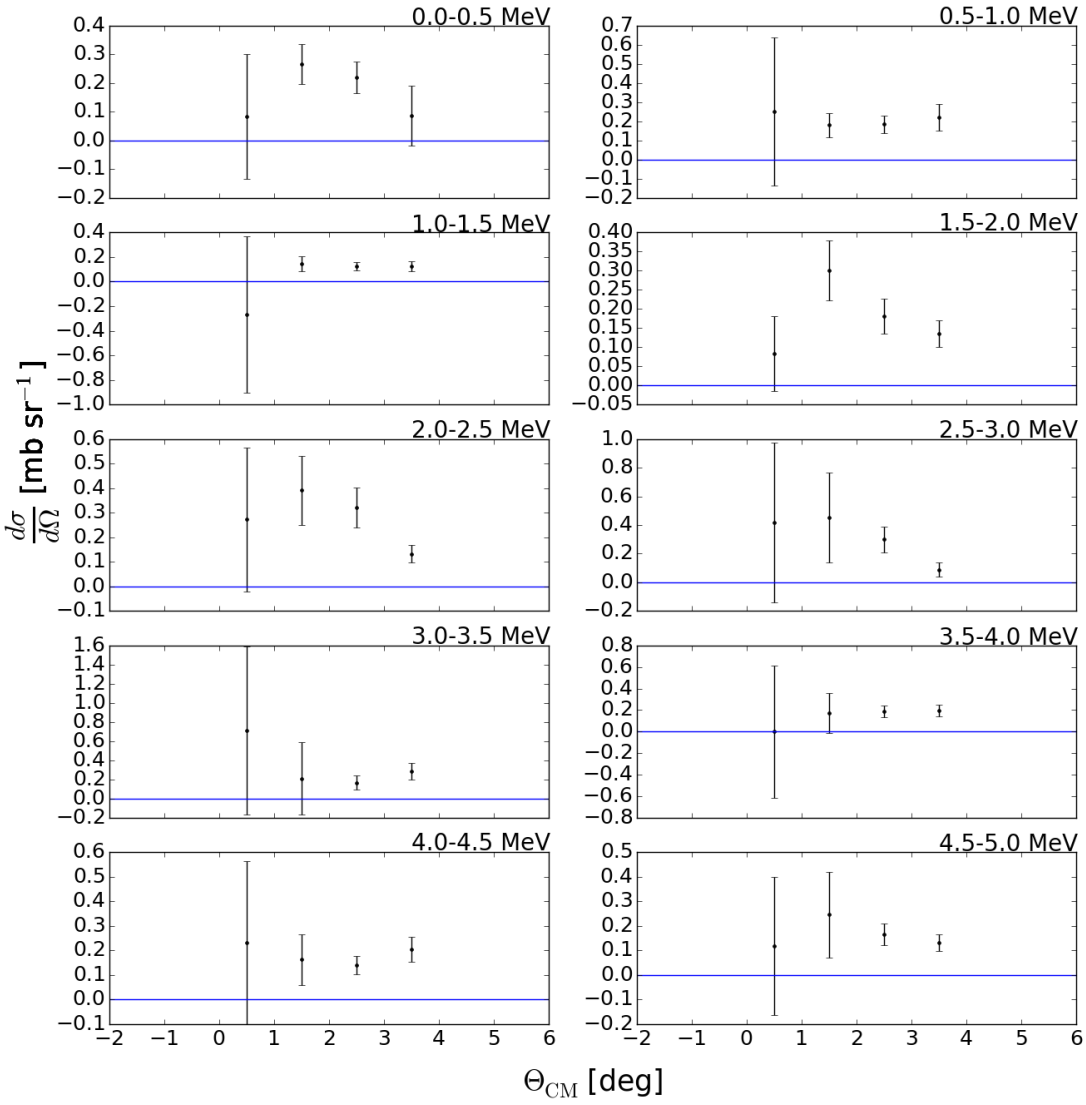

Figure 4.27: Krypton angular distributions extracted for each energy bin (0.5 MeV) up to 5 MeV. Forward peaking distributions indicated a possible Gamow-Teller component in the cross section.

the multipole decomposition analysis (section 4.6). The other use for the DWBA calculation was to extrapolate the extracted $\Delta L = 0$ cross section to zero momentum transfer (which is equivalent to $Q = 0$, $\Theta = 0$). With this extrapolated cross section, the proportionality

between the cross section and the Gamow-Teller strength distribution could be exploited (equation 3.19).

As mentioned previously, three multipole components were assumed in the krypton data: monopole, dipole and quadrupole. Although higher order multipoles could contribute, they are likely small due to the small momentum transfer involved. Additionally, their angular distributions are similar to that of the $\Delta L = 2$ component at forward scattering angles and, hence, are difficult to separate from the quadrupole component. Each of the transitions has a defining set of selection rules, which are detailed in table 4.6. Because Gamow-Teller transitions are of interest for this work, the $\Delta J = 1$ component is used for the monopole component. For the dipole components, the $\Delta J = 1$ component was chosen because 2^- transitions, on average, appear at lower excitation energies than 0^- and 1^- transitions. Moreover, because the total dipole strength scales with $2J + 1$, the 2^- component is the strongest. Finally, for the quadrupole component, the $\Delta J = 2$ component was used because it tends to be the strongest of the three possible transitions.

Table 4.6: Selection rules for monopole, dipole and quadrupole transitions.

	ΔL	ΔS	ΔJ	Parity
Monopole	0	0,1	0,1	no transfer
Dipole	1	0,1	0,1,2	transfer
Quadrupole	2	0,1	1,2,3	no transfer

The inputs to the ^{86}Kr DWBA calculation, such as the nucleon-nucleon interaction and optical potential, were detailed in section 3.2. To designate the multipole to be calculated by FOLD, one-body transition densities (OBTDs) were input based on the selection rule of the transition in question. The OBTDs for the monopole and quadrupole transitions were generated by OXBASH [115] using the SNET interaction [76]. The dipole transition, however, required a parity transfer, which could not be calculated using the aforementioned

interaction; instead a normal modes calculation, using the code NORMOD [136], was utilized to obtain the proper transition densities. With this information, the general shape of each of the multipoles was extracted, and the results are shown in figure 4.28. It is important to note that, because the shape of the angular distributions is not sensitive to the details of the microscopic input, the method used to obtain the one-body transitions densities is not of great importance.

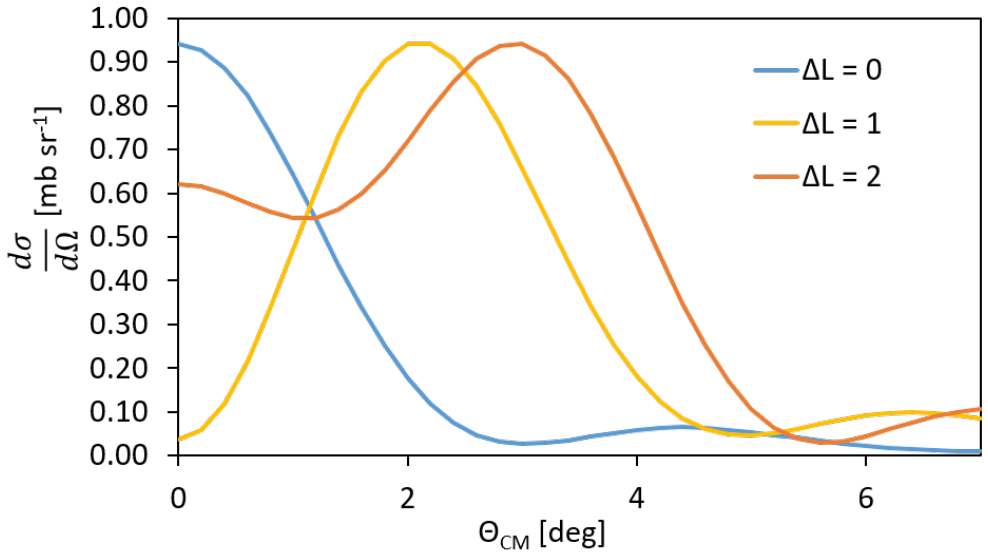

Figure 4.28: DWBA calculation results for ^{86}Kr(t,^{3}He) at 140 MeV/u. The calculation was performed using the FOLD software package [102], and shows the three most likely transitions to appear in the experimental data. The curves shown here are normalized so that their peaks have the same magnitude. The shapes of the $\Delta L = 0$ (blue), $\Delta L = 1$ (yellow) and $\Delta L = 2$ (orange) components are the important result for the analysis.

As expected, the monopole component peaks at forward scattering angles, and each progressive multipole peaks at larger angles. It was assumed that the experimental data contained a mixture of these transitions in varying proportions. Therefore, by fitting the data with a linear combination of the calculated multipoles, the components contributing to the total experimental cross section were extracted.

4.6 Multipole Decomposition Analysis

The multipole decomposition analysis (MDA) sought to determine which features of the extracted angular distributions were consistent with monopole, dipole or quadrupole transitions from the target nucleus [137, 138]. A linear combination of the multipoles was constructed with the following form:

$$\sigma_{\text{Total}} = A\sigma_{\Delta L=0} + B\sigma_{\Delta L=1} + C\sigma_{\Delta L=2} \tag{4.5}$$

where $\sigma_{\Delta L=0,1,2}$ are the cross sections obtained from the DWBA calculations (section 4.5) for the $\Delta L = 0$, 1 and 2 components, respectively. A, B, and C are the constants optimized in the MDA fitting routine, and describe the relative contributions of each of the multipoles to the total cross section. The sum of the cross sections was fit to the angular distributions from figure 4.27, and the results of the MDA fits, up to 5 MeV, are shown in figure 4.29.

From these results, it was apparent that a combination of these transitions described the cross section as it was measured. However, because the error bars on the experimental data points were large, the fitting parameters also carried large uncertainties. Nevertheless, it was possible to use the extracted fitting parameters for the monopole component to generate a Gamow-Teller strength distribution, and to place an upper limit on the strength present in ^{86}Kr.

The Gamow-Teller strength distribution was extracted using the well-established proportionality with the cross section at zero momentum transfer, discussed in section 3.3. The

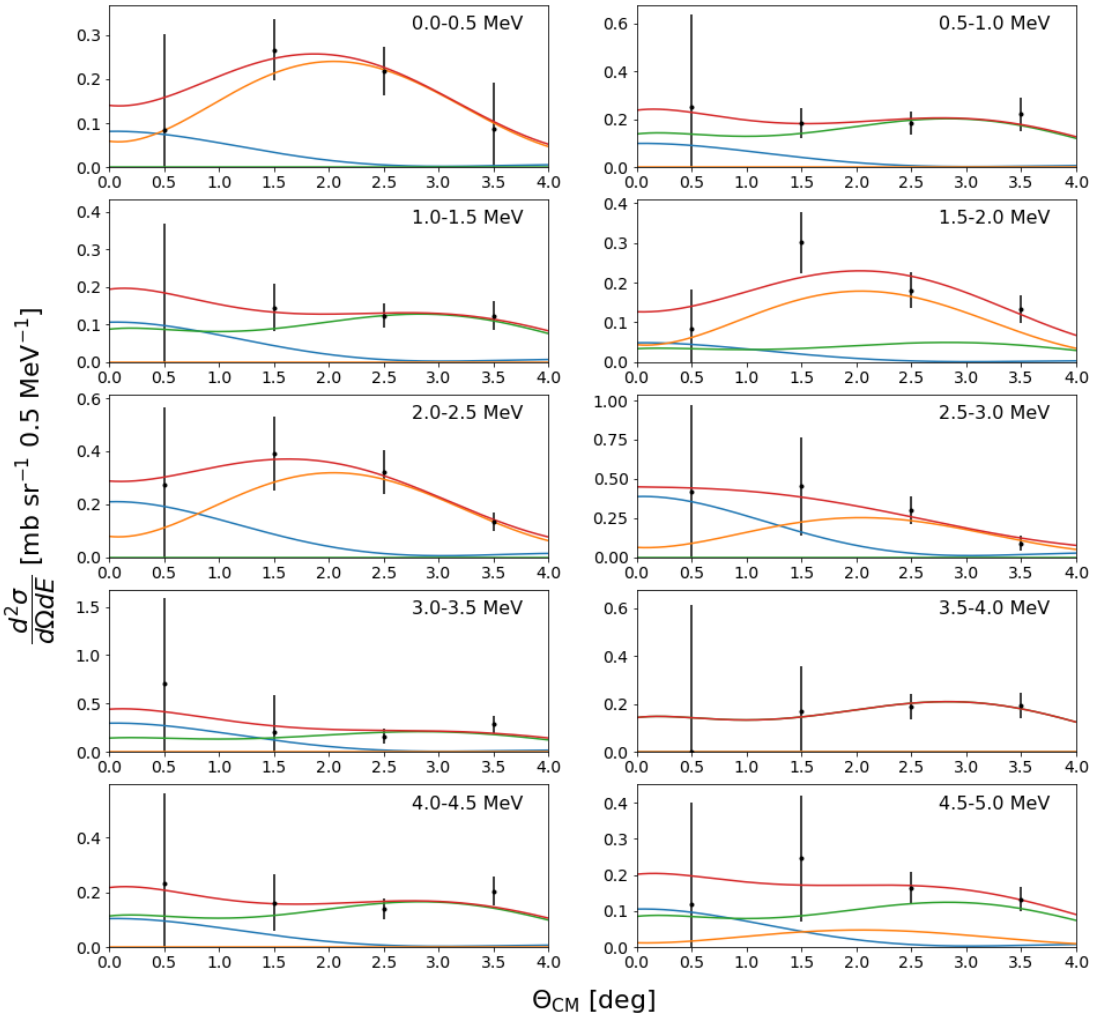

Figure 4.29: The MDA results, here, show the experimental data (black points) and the linear combination of multipoles that best fit the data in each energy bin. The total combination (red curve) is the sum of each of the components: $\Delta L = 0$ (blue), $\Delta L = 1$ (yellow) and $\Delta L = 2$ (green).

equation describing the proportionality is as follows [51]:

$$\left[\frac{d\sigma}{d\Omega}(q=0)\right]_{GT} = \widehat{\sigma}B(GT). \tag{4.6}$$

The left-hand side of the equation is the $\Delta L = 0$ component of the differential cross section, as measured in the experiment, extrapolated to zero momentum transfer ($q = 0$) by using the value of the DWBA calculation with the Q-value of the reaction set to 0 MeV, at a scattering angle of 0 degrees. On the right-hand side of the equation, $\widehat{\sigma}$ is the unit cross section, and is determined empirically using the following expression [12, 51, 116, 117, 118]:

$$\widehat{\sigma} = 109 \times A^{-0.65} \tag{4.7}$$

where A is the mass number of the nucleus. For the transition from ^{86}Kr to ^{86}Br, the unit cross section is 6.03, with an uncertainty of approximately 5%. Combining the extrapolated cross section from the experiment with the unit cross section yielded the Gamow-Teller strength distribution for the ^{86}Kr(t,^{3}He) reaction, shown in figure 4.30.

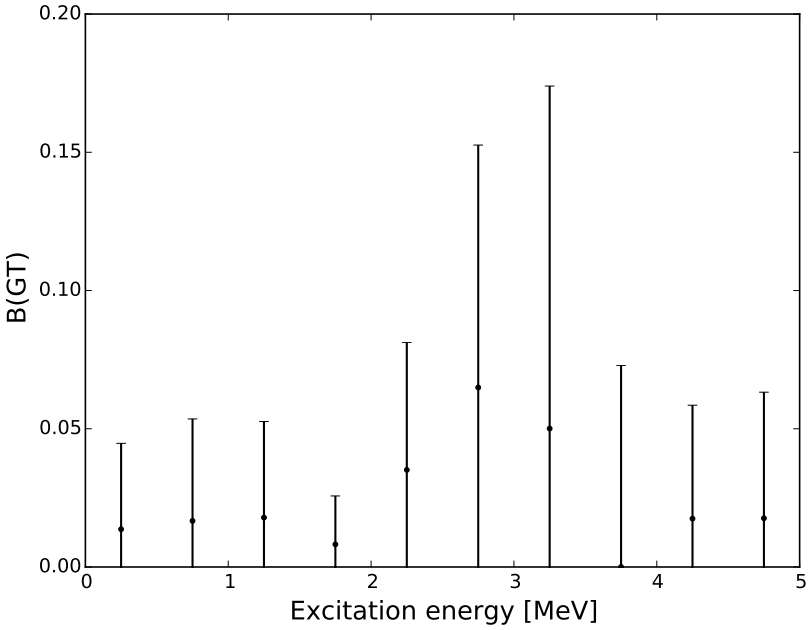

Figure 4.30: The Gamow-Teller strength distribution for ^{86}Kr extracted from the results of the MDA.

The level scheme for ^{86}Br does not indicate that there are any 1^+ states below 2.5 MeV; therefore, it is unlikely to find true Gamow-Teller strength below that energy. Examining figure 4.30, it is shown that the limit of the sensitivity of this experiment is $B(GT) \sim 0.05$. Because the data points below 2 MeV are similar in magnitude to the points above 3.5 MeV, the strength at the higher excitation energies is also unlikely to be Gamow-Teller. It is important to note that the error bars on all of the points are large due to the statistical and systematic uncertainties present in the experimental data. As such, it is possible only to set an upper limit on the Gamow-Teller strength. Analysis of the γ-ray data, discussed in section 4.7, provides stricter limits on the strength that was observed in this experiment.

4.7 Gamma-Ray Analysis

Because of the systematic uncertainties in the experiment, as discussed in the previous section, it was only possible to obtain an upper limit on the Gamow-Teller strength for ^{86}Kr from the singles data. In an effort to improve this limit, the coincidence data from GRETINA and the S800 were used, as the γ-detection array was capable of measuring weak transitions with high precision, without subtracting away the target window events.

The decay spectrum of ^{86}Br, the residual nucleus of the ^{86}Kr(t,^{3}He) reaction, is partially known, though spin and parity assignments are not available for all of the recorded levels [139]. It was expected that some Gamow-Teller strength would be observed at 2.45 MeV and 2.67 MeV, which are the locations of two known 1^+ states in ^{86}Br. However, none of the γ-rays associated with de-excitations from those states was observed. Analyzing the remainder of the γ-ray spectrum, known lines from the target window reaction residuals, such as decays of ^{12}B, ^{14}C and ^{16}N, or lines from ^{85}Br, which occur when the excitation

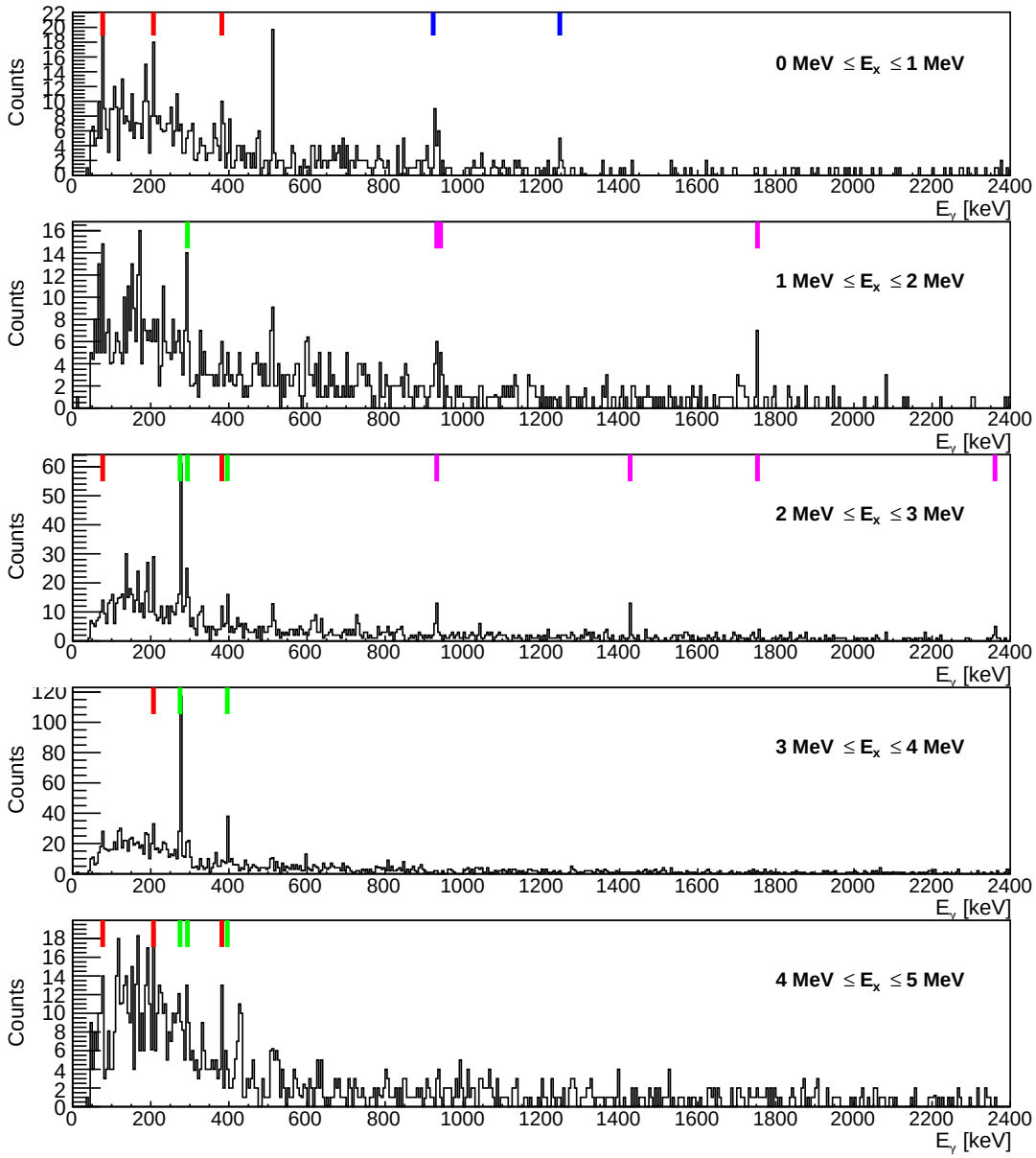

Figure 4.31: The γ decay spectra for each excitation energy bin. The γ-lines associated with marked at the top of each plot: ^{86}Br in red, ^{14}C in blue, ^{16}N in green, and lines associated with no known nucleus in magenta. The peak at 511 keV in the top three panels originates from electron-positron annihilation.

energy is greater than the single neutron separation energy at 5.128 MeV, were identified and excluded from the analysis. The γ-decay spectra for each 1 MeV excitation energy bin are shown in figure 4.31: γ-lines associated with known lines in ^{86}Br are marked in red,

lines from ^{14}C are marked in blue, lines from ^{16}N are marked in green, and lines that are not associated with any known nucleus (and, thus, are assumed to originate from ^{86}Br) are marked in magenta.

Several weak lines from ^{86}Br were observed, as well as γ-rays not measured and recorded in the Nuclear Data Sheets [139]. The γ-ray spectra obtained from the krypton coincidence data set were examined in close detail in 1 MeV excitation energy bins. Some lines were only visible at specific excitation energies, while others appeared throughout the excitation energy spectrum. Each of the observed peaks was compared to known γ-ray spectra of ^{12}B, ^{14}C and ^{16}N, the residuals from reactions on target window nuclei. Lines in the krypton spectrum that were known to originate from a target window residual were disregarded as background events, while any other peaks were noted for further analysis. The final list of γ-rays that were either identified from the ^{86}Br decay scheme, or those that were not identified in any other spectrum, are compiled in the first column of table 4.7. The assumption was made that the γ-lines listed here originated from the de-excitation of ^{86}Br, so that they could be further studied in the search for weak Gamow-Teller strength.

The general steps of the analysis are listed here; more details concerning each of the states are presented below. The E_γ spectrum, zoomed in on each γ-line, is shown in the top plot in figures 4.32 through 4.41. A gate with a width of 5 keV was made around the γ-line, and the excitation energy spectrum of the particles associated with that γ-ray was extracted. These excitation energy spectra, deduced from the $(t,^3\mathrm{He})$ reaction data, are shown in the bottom left plots in figures 4.32 through 4.41. Finally, a gate was placed on the excitation energy, encompassing the largest peak in the spectrum, typically with a width on the order of 1.5 MeV.

The data were re-processed, including both the cuts on E_γ and the excitation energy,

Table 4.7: γ-rays from de-excitations of ^{86}Br. These lines appear in the γ spectrum from the krypton data set, and are not associated with de-excitations of the residual nuclei from reactions on the target windows, for example ^{12}B, ^{14}C or ^{16}N. Also listed are the J^π assignments for each state, when known (tentative assignments are given in parentheses), the excitation energy of events associated with each γ-ray, as determined from the (t,^{3}He) data, and the type of transition, determined from examining the shape of the calculated angular distribution.

E_γ (keV)	J^π	E_x (MeV)	Transition
77	(4^-)	$\sim$0.0	$\Delta L \geq 1$
207	$(1^-,2^-)$	peak 1: $\sim$3.0	$\Delta L \geq 1$
		peak 2: $\sim$4.0	$\Delta L = 0$, $\Delta L = 2$
382	$(1^-,2)$	$\sim$2.5	$\Delta L = 1$
932	unknown	peak 1: $\sim$1.0	$\Delta L \geq 2$
		peak 2: $\sim$2.5	$\Delta L = 1$
942	unknown	$\sim$1.75	$\Delta L \geq 1$
1427	unknown	$\sim$2.25	$\Delta L = 1$
1753	unknown	$\sim$1.75	$\Delta L = 0$, $\Delta L = 2$
2361	unknown	$\sim$2.25	$\Delta L = 0$, $\Delta L = 2$

and using these gated spectra, the angular distribution for the events associated with each of the listed γ-lines was extracted (shown in the bottom right plots in figures 4.32 through 4.41). The efficiency of the GRETINA detector array was incorporated into the calculation of the cross section and angular distribution. The efficiency curve, presented in figure 4.8, was obtained by fitting ^{152}Eu source data taken prior to the experiment. An assumption for the type of transition that produced each γ-ray, deduced from the shape of the angular distribution, is presented for each case, and also listed in table 4.7.

77 keV: Figure 4.32 shows the 77 keV γ-ray. γ energies from 74 keV to 80 keV were selected, generating a gated excitation energy spectrum. A single peak appeared in this spectrum, just above 0 MeV. A gate on the excitation energy was made from -0.5 MeV to 1 MeV. Applying both the E_γ gate and the excitation energy gate to the data allowed for the calculation of the cross section for the events that yielded a 77 keV γ-ray. The angular distribution that was extracted from the data peaked at approximately 2.5 degrees

in the center of mass frame, indicating that the γ-rays most likely came from a dipole or a quadrupole transition.

207 keV: Figures 4.33 and 4.34 show the analysis of the 207 keV γ-ray. γ energies from 205 keV to 209 keV were selected, generating the gated excitation energy spectrum. Two peaks appeared in this spectrum: one at 3 MeV and another at approximately 4 MeV. Both of these peaks were analyzed further. First, an excitation energy gate from 2.5 MeV to 3.5 MeV was made (figure 4.33), and the angular distribution was extracted. The distribution peaked between 1.5 and 2.5 degrees in the center of mass frame, indicating that the γ-rays yielded from events in the first excitation energy peak were likely the product of a dipole or a quadrupole transition. Then, returning to the original excitation energy spectrum, a new gate was made from 3.5 MeV to 4.5 MeV (figure 4.34). The extracted angular distribution could not be associated with a particular ΔL value, indicating that these events were likely from background under the 207 keV γ-ray peak, rather than from a single state.

382 keV: Figure 4.35 shows the 382 keV γ-ray. γ energies from 380 keV to 384 keV were selected, generating the gated excitation energy spectrum with a single peak at approximately 2.5 MeV. A gate on the excitation energy from 2 MeV to 3 MeV was applied to the data. The extracted angular distribution peaked at approximately 1.5 degrees in the center of mass frame, indicating that the γ-rays yielded from these events were likely the product of a dipole transition, although a higher value of ΔL cannot be ruled out.

932 keV: Figures 4.36 and 4.37 show the analysis of the 932 keV γ-ray. γ energies from 928 keV to 933 keV were selected, and, as with the case of the 207 keV line, two peaks appeared in the gated excitation energy spectrum, at 1 MeV and 2.5 MeV, respectively. First, an excitation energy gate from 0.5 MeV to 2 MeV was made (figure 4.36), and the angular distribution was extracted. The distribution peaked beyond 1.5 degrees in the center

of mass frame, indicating that the γ-rays yielded from events in the first excitation energy peak were likely the product of a quadrupole transition. Then, returning to the original excitation energy spectrum, a new gate was made from 2 MeV to 3 MeV (figure 4.37). The extracted angular distribution peaked at approximately 1.5 degrees, indicating the γ-rays were likely the product of a dipole transition.

942 keV: Figure 4.38 shows the 942 keV γ-ray. γ energies from 941 keV to 945 keV were selected, yielding a gated excitation energy spectrum with a single peak at 1.75 MeV. Applying a gate to the excitation energy from 1 MeV to 2 MeV, the angular distribution was extracted and shown to peak between 1.5 and 2.5 degrees in the center of mass frame, indicating that the γ-rays were likely the product of a dipole, quadrupole or higher multipole transition.

1427 keV: Figure 4.39 shows the 1427 keV γ-ray. γ energies from 1420 keV to 1430 keV were selected, yielding a gated excitation energy spectrum with a single peak at 2.25 MeV. Applying a gate to the excitation energy from 1.5 MeV to 3 MeV, the angular distribution was extracted and shown to peak around 1.5 degrees in the center of mass frame, indicating that the γ-rays were likely the product of a dipole transition.

1753 keV: Figure 4.40 shows the 1753 keV γ-ray. γ energies from 1750 keV to 1755 keV were selected, yielding a gated excitation energy spectrum with a single peak at approximately 1.75 MeV. Applying a gate to the excitation energy from 1.25 MeV to 2.25 MeV, the angular distribution was extracted and seemed to peak at forward angles, indicating a potential Gamow-Teller transition. As such, the distribution associated with 1753 keV γ-ray was noted for further analysis.

2361 keV: Figure 4.41 shows the 2361 keV γ-ray. γ energies from 2359 keV to 2363 keV were selected, yielding a gated excitation energy spectrum with a single peak at ap-

proximately 2.25 MeV. Applying a gate to the excitation energy from 2 MeV to 3 MeV, the angular distribution was extracted and shown to peak at forward angles, indicating a potential Gamow-Teller transition. Therefore, the distribution associated with 2361 keV γ-ray was noted for further analysis.

Peaks appear in the excitation energy spectrum at 2.25 MeV for both the 1427 keV and 2361 keV γ-lines, indicating a potential decay from the 2361 keV state via the emission of 1427 keV and 942 keV γ-rays, within the experimental resolution. However, because excitation energy peaks corresponding to the 942 keV γ-ray do not appear in the spectra of the 2361 keV and 1427 keV lines, the possibility of this decay was ruled out.

After gating on E_γ and the excitation energy, the angular distributions were assumed to contain contributions from a single state, making the analysis cleaner. For the majority of the lines (207 keV, 382 keV, 932 keV (E_x peak 2), 942 keV, 1427 keV), peaks in the excitation energy spectrum appeared above the energy of the measured γ-ray, indicating that the γ resulted from a decay in which the residual nucleus passed through several excited states before emitting the final photon that was measured. For the cases of the 77 keV, 932 keV (E_x peak 1), 1753 keV and 2361 keV lines, the excitation energy peaked at approximately the same energy as the γ-ray, within the experimental energy resolution, indicating that the state decayed directly to the ground state of ^{86}Br, or to one of its low-lying states.

As mentioned in section 4.5, Gamow-Teller transitions are characterized by a forward-peaking angular distribution. Therefore, for an MDA fit, the distributions would be fit with either a $\Delta L = 0 + \Delta L = 2$ linear combination, or with a $\Delta L = 1$ curve, described by equation 4.5. Those distributions that were flat or that peaked at backward angles were assumed to not be Gamow-Teller transitions and were, therefore, discarded from the remainder of the analysis. As described previously, of the γ-rays listed in table 4.7, only two of them had

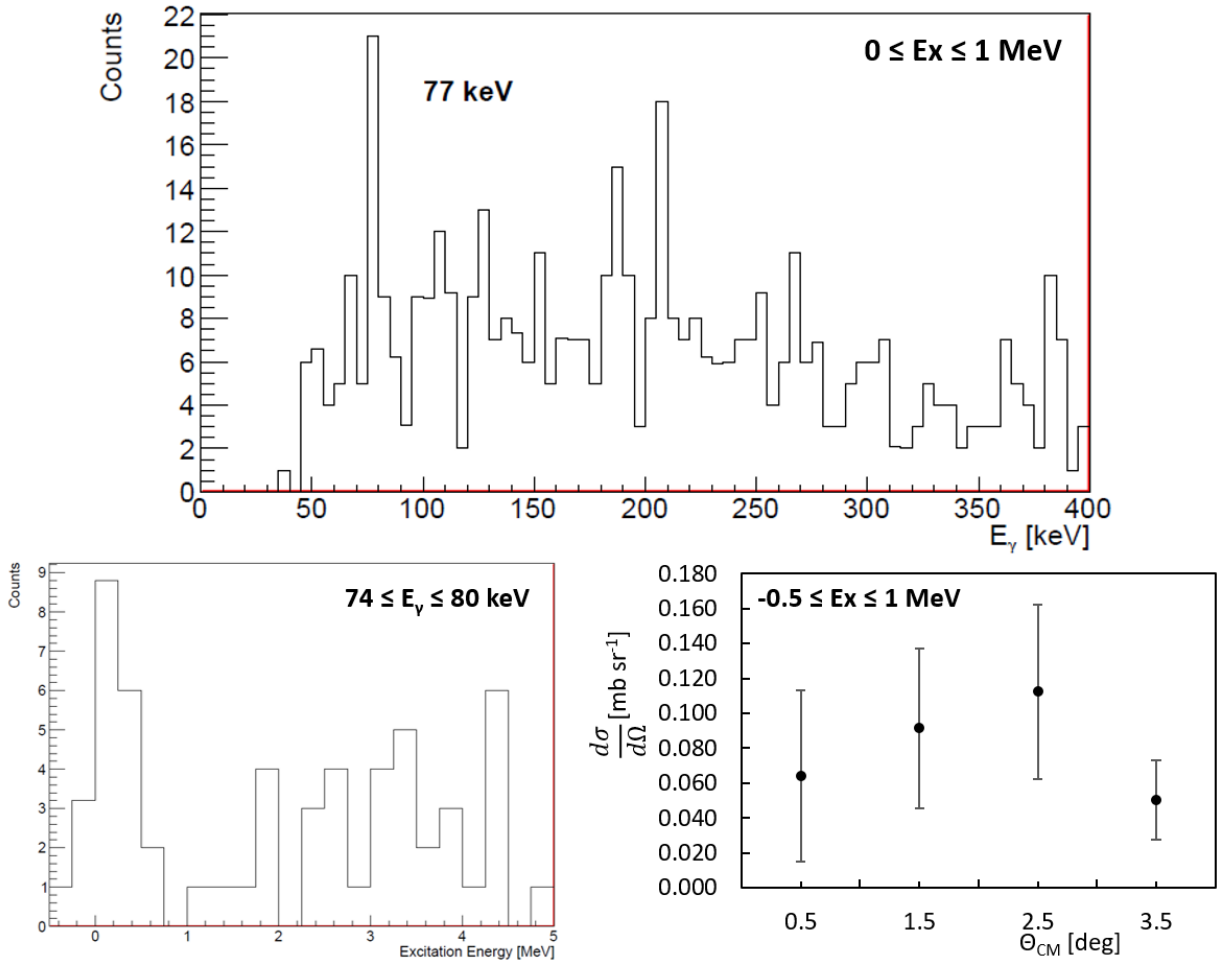

Figure 4.32: $E_\gamma = 77$ keV. A gate on E_γ was made from 74 keV to 80 keV. One peak appeared in the resulting gated excitation energy spectrum. For the peak at $E_x = 0$ MeV, a gate was made from -0.5 MeV to 1 MeV and the angular distribution found in the bottom right of the figure was extracted. Because the angular distribution does not appear to peak at forward angles, a further MDA was not performed on this angular distribution.

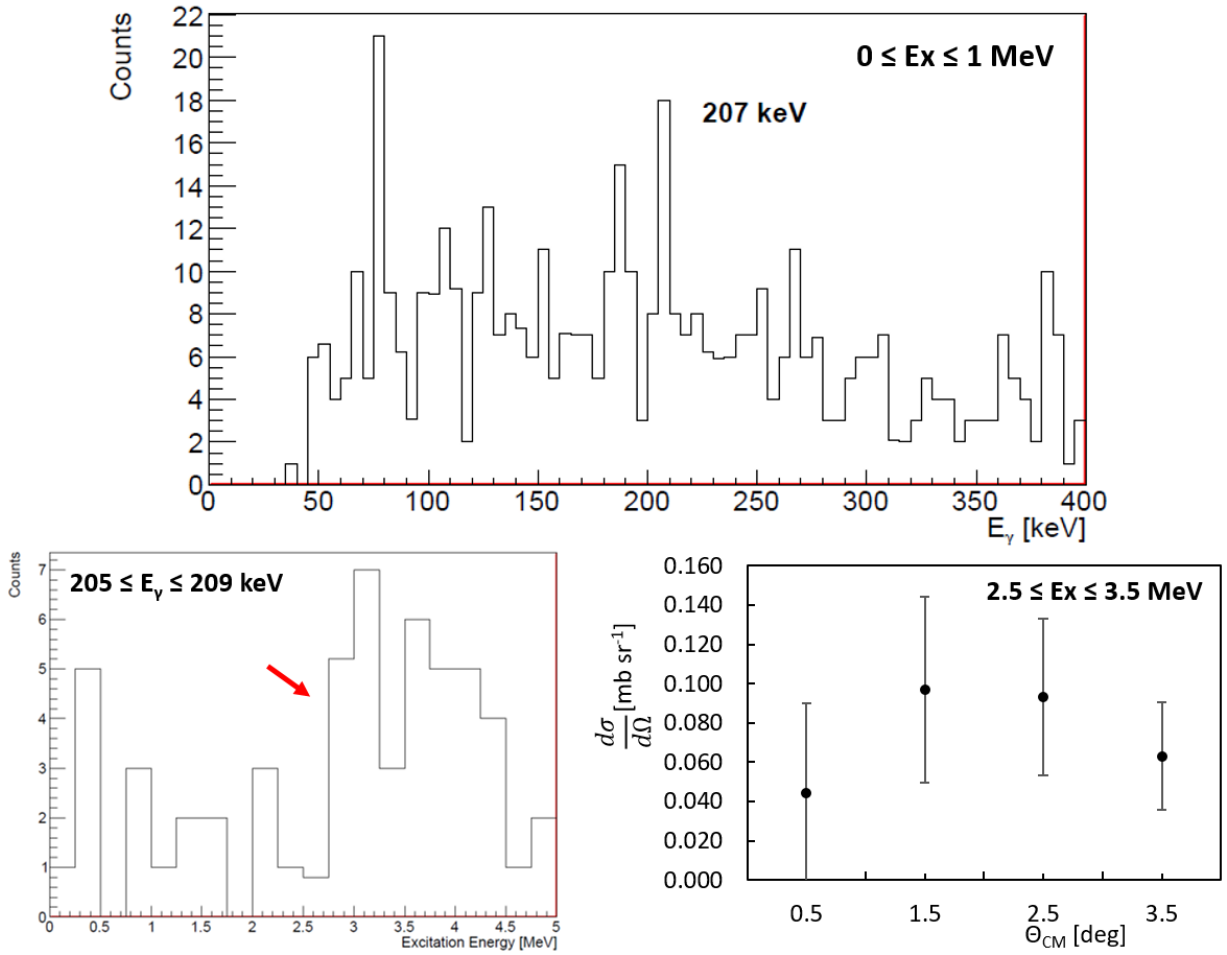

Figure 4.33: $E_\gamma = 207$ keV. A gate on E_γ was made from 205 keV to 209 keV. Two peaks appeared in the resulting gated excitation energy spectrum. For the first peak, at $E_x = 3$ MeV, a gate was made from 2.5 MeV to 3.5 MeV and the angular distribution found in the bottom right of the figure was extracted. Because the angular distribution does not appear to peak at forward angles, a further MDA was not performed on this angular distribution.

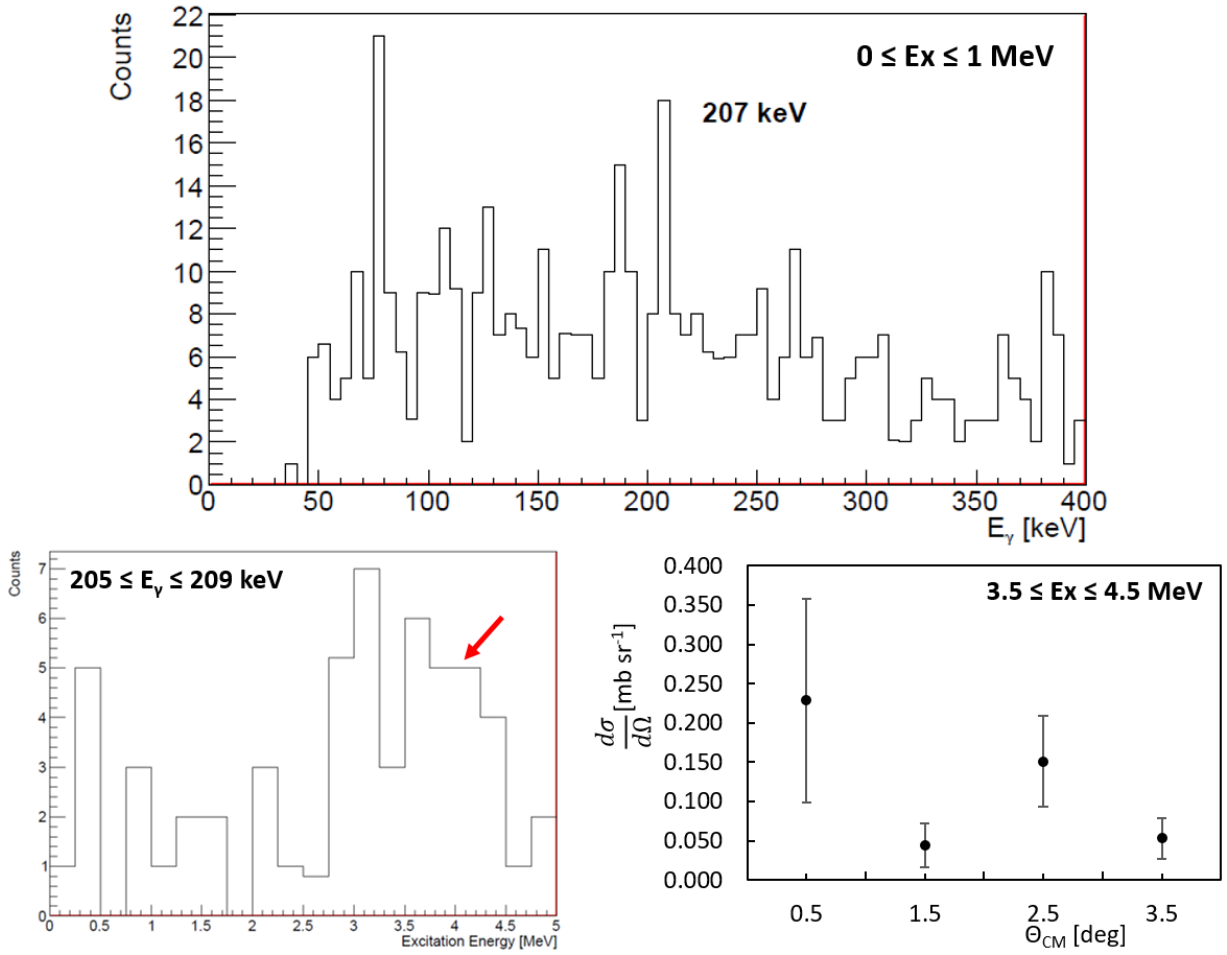

Figure 4.34: $E_\gamma = 207$ keV. A gate on E_γ was made from 205 keV to 209 keV. Two peaks appeared in the resulting gated excitation energy spectrum. For the first peak, at $E_x = 4$ MeV, a gate was made from 3.5 MeV to 4.5 MeV and the angular distribution found in the bottom right of the figure was extracted. Because the angular distribution appears to peak at forward angles, a further MDA was performed on this angular distribution.

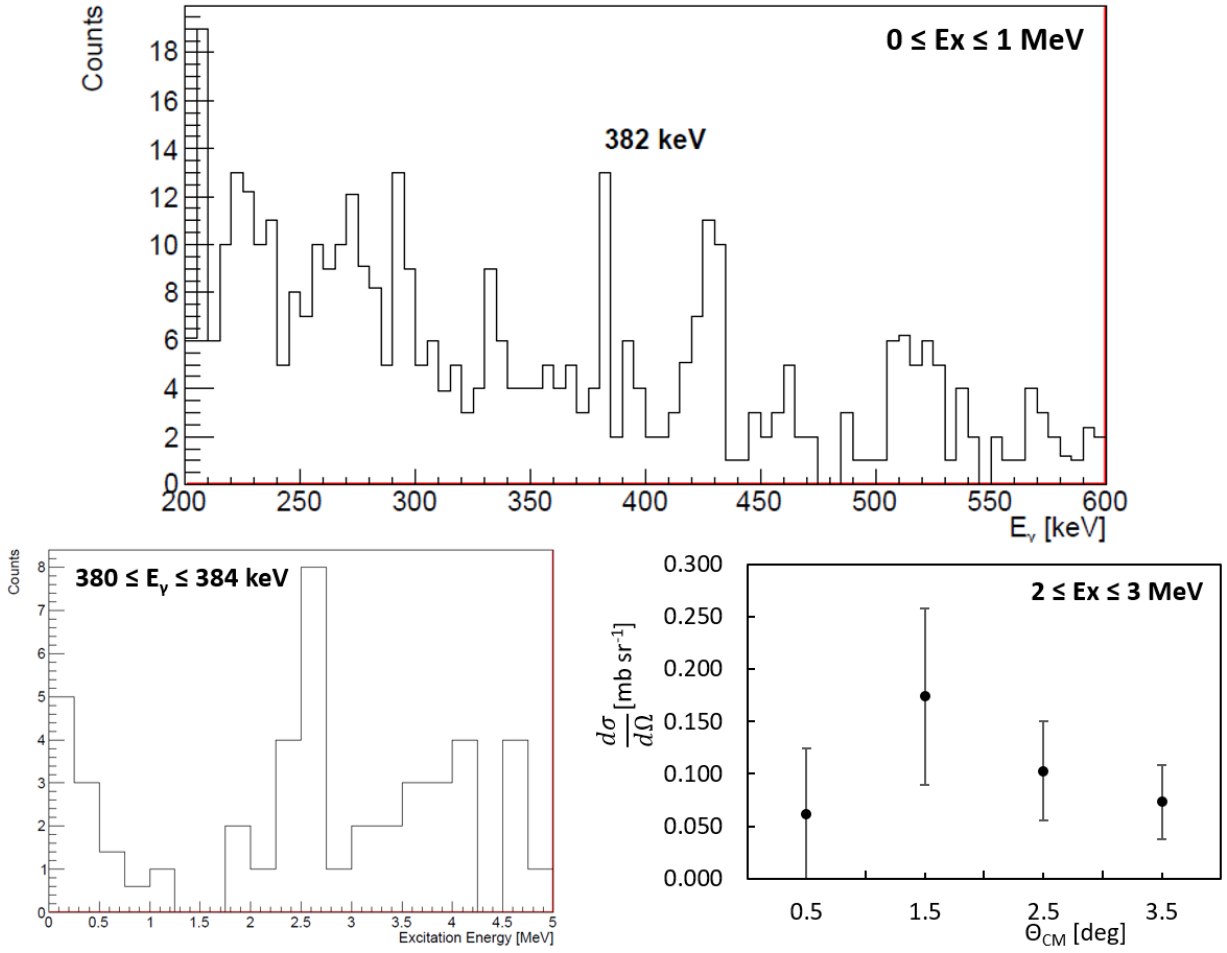

Figure 4.35: $E_\gamma = 382$ keV. A gate on E_γ was made from 380 keV to 384 keV. Two peaks appeared in the resulting gated excitation energy spectrum. For the peak at $E_x = 2.5$ MeV, a gate was made from 2 MeV to 3 MeV and the angular distribution found in the bottom right of the figure was extracted. Because the angular distribution does not appear to peak at forward angles, a further MDA was not performed on this angular distribution.

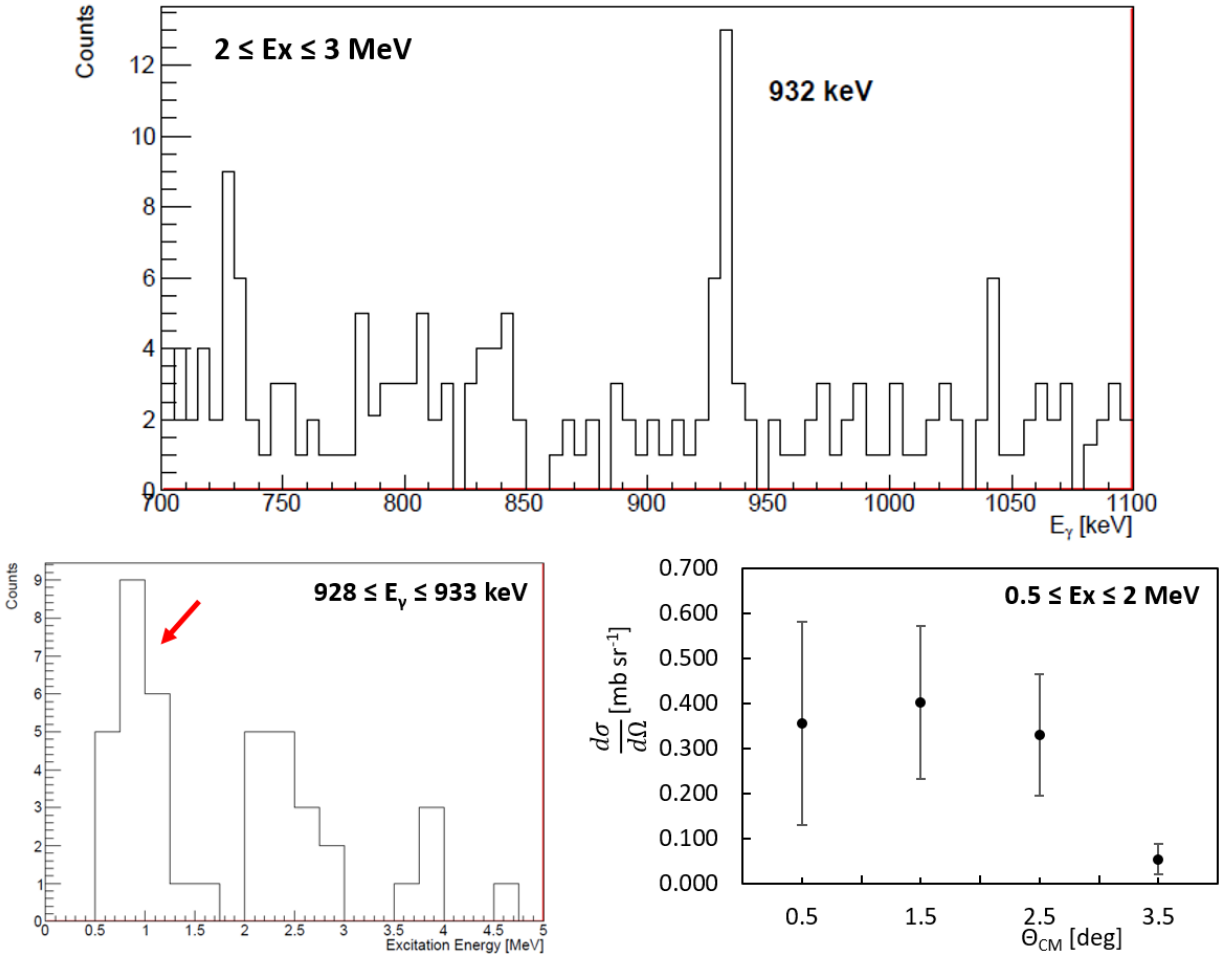

Figure 4.36: $E_\gamma = 932$ keV. A gate on E_γ was made from 928 keV to 933 keV. Two peaks appeared in the resulting gated excitation energy spectrum. For the first peak, at $E_x = 1$ MeV, a gate was made from 0.5 MeV to 2 MeV and the angular distribution found in the bottom right of the figure was extracted. Because the angular distribution does not appear to peak at forward angles, a further MDA was not performed on this angular distribution.

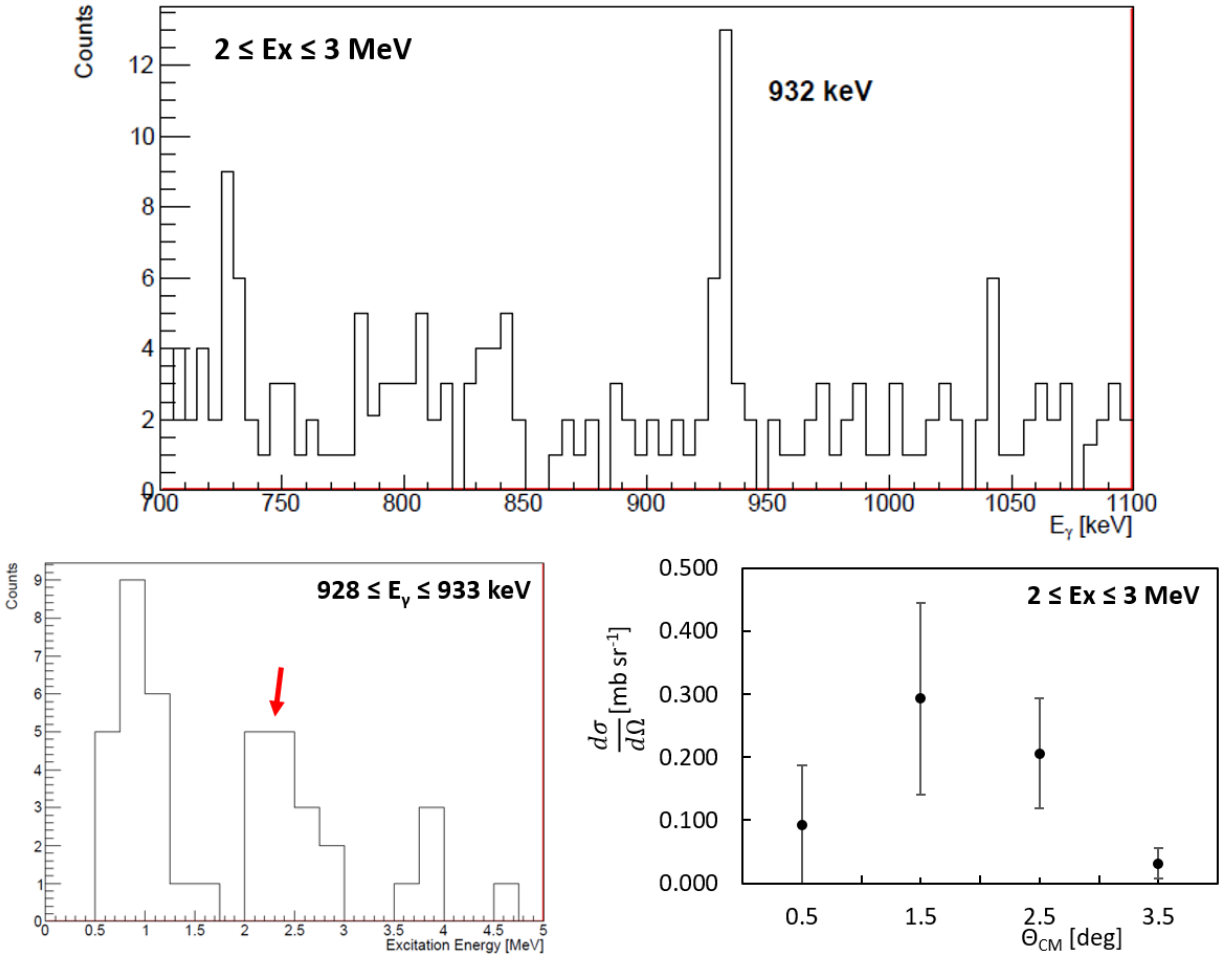

Figure 4.37: $E_\gamma = 932$ keV. A gate on E_γ was made from 928 keV to 933 keV. Two peaks appeared in the resulting gated excitation energy spectrum. For the second peak, at $E_x = 2.5$ MeV, a gate was made from 2 MeV to 3 MeV and the angular distribution found in the bottom right of the figure was extracted. Because the angular distribution does not appear to peak at forward angles, a further MDA was not performed on this angular distribution.

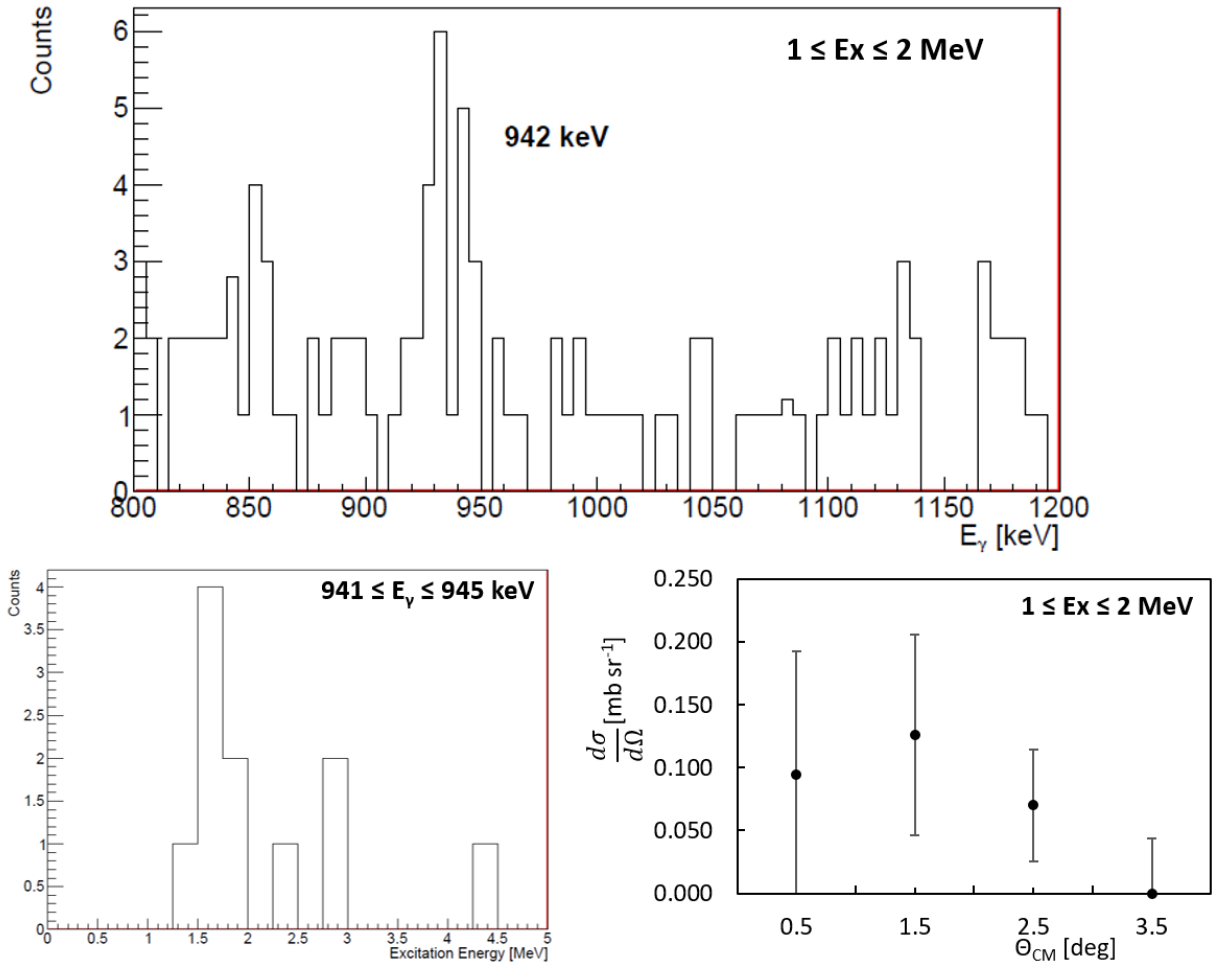

Figure 4.38: $E_\gamma = 942$ keV. A gate on E_γ was made from 941 keV to 945 keV. One peak appeared in the resulting gated excitation energy spectrum. For the peak at approximately $E_x = 1.5$ MeV, a gate was made from 1 MeV to 2 MeV and the angular distribution found in the bottom right of the figure was extracted. Because the angular distribution does not appear to peak at forward angles, a further MDA was not performed on this angular distribution.

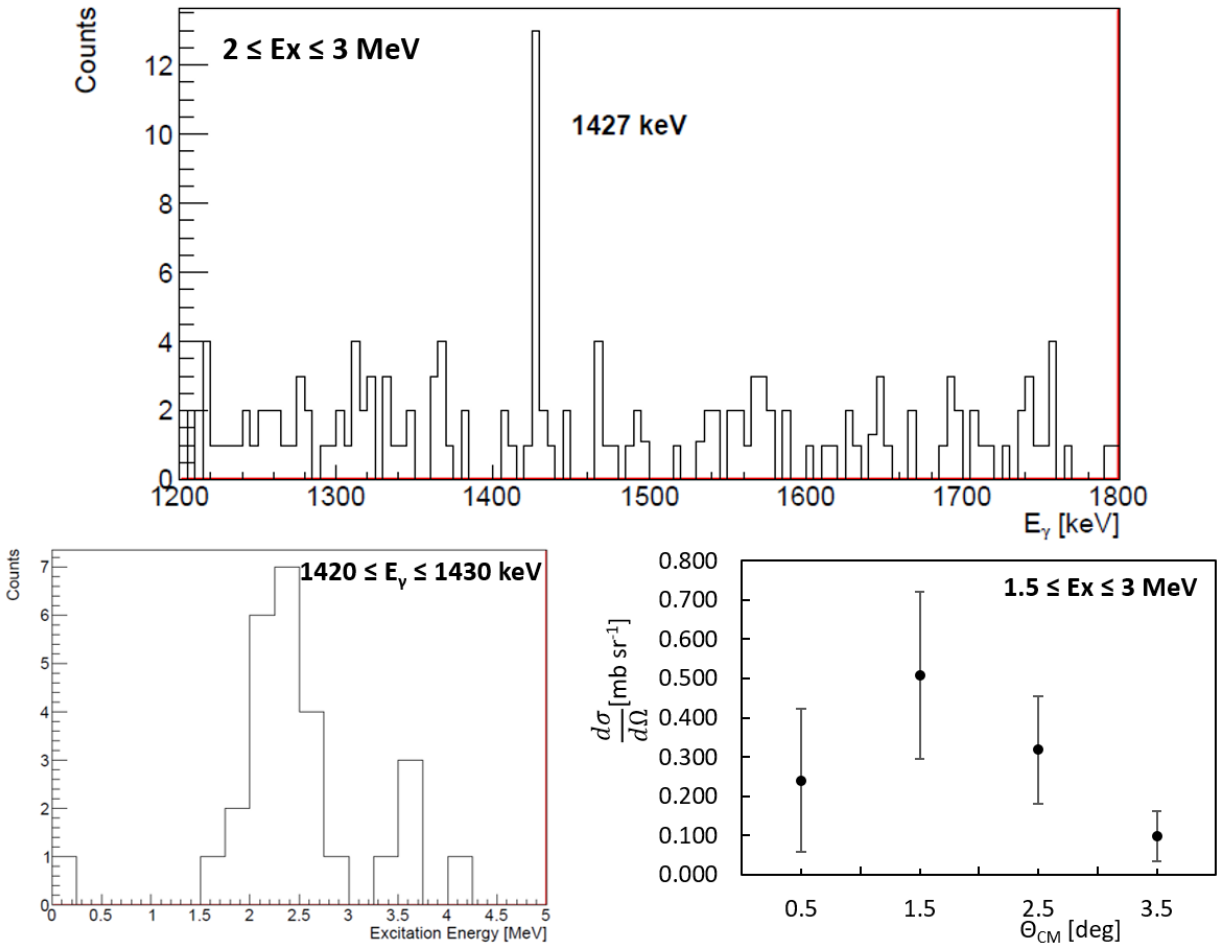

Figure 4.39: $E_\gamma = 1427$ keV. A gate on E_γ was made from 1420 keV to 1430 keV. One peak appeared in the resulting gated excitation energy spectrum. For the peak at approximately $E_x = 2.3$ MeV, a gate was made from 1.5 MeV to 3 MeV and the angular distribution found in the bottom right of the figure was extracted. Because the angular distribution does not appear to peak at forward angles, a further MDA was not performed on this angular distribution.

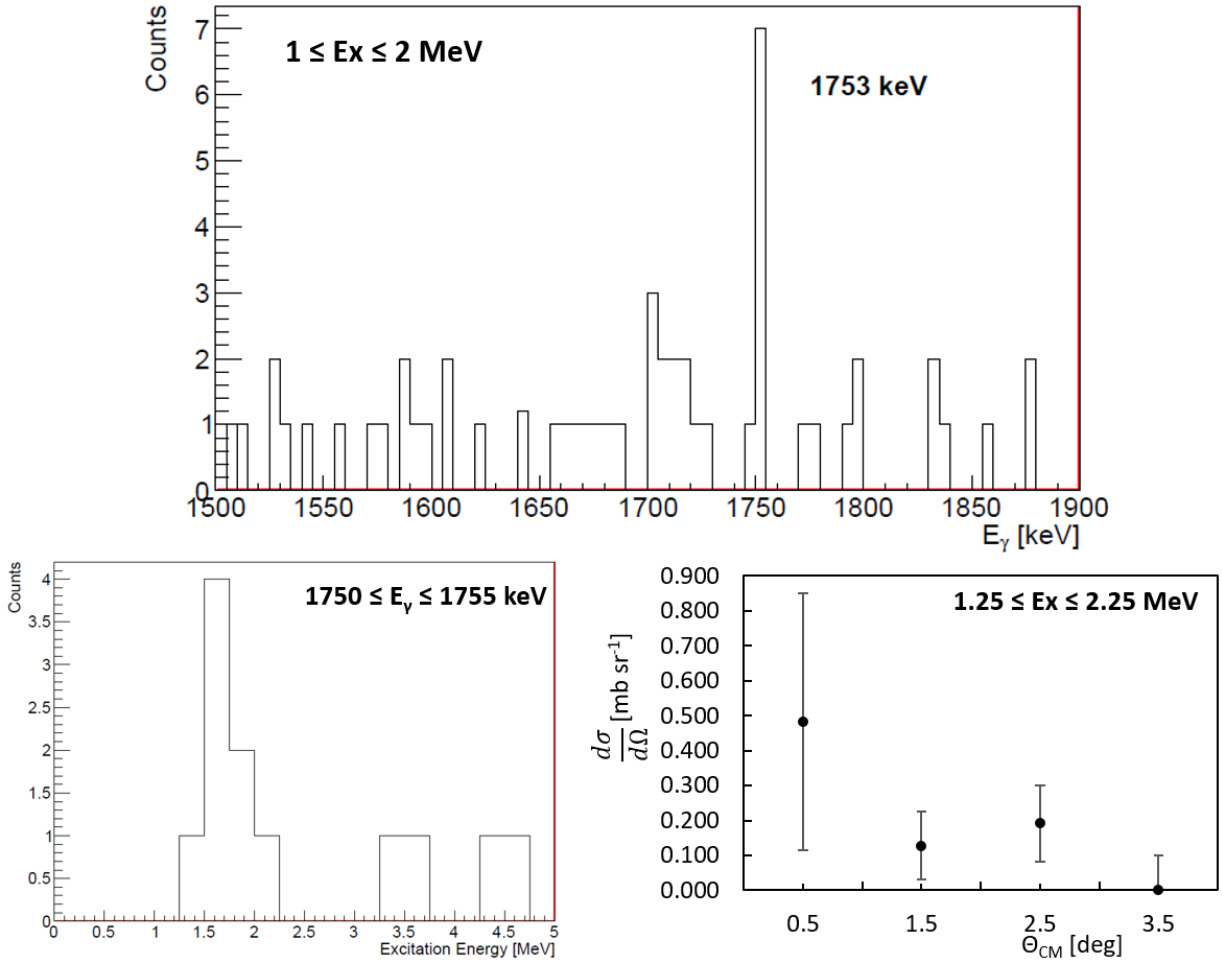

Figure 4.40: $E_\gamma = 1753$ keV. A gate on E_γ was made from 1750 keV to 1755 keV. One peak appeared in the resulting gated excitation energy spectrum. For the peak at approximately $E_x = 1.7$ MeV, a gate was made from 1.25 MeV to 2.25 MeV and the angular distribution found in the bottom right of the figure was extracted. Because the angular distribution appears to peak at forward angles, a further MDA was performed on this angular distribution.

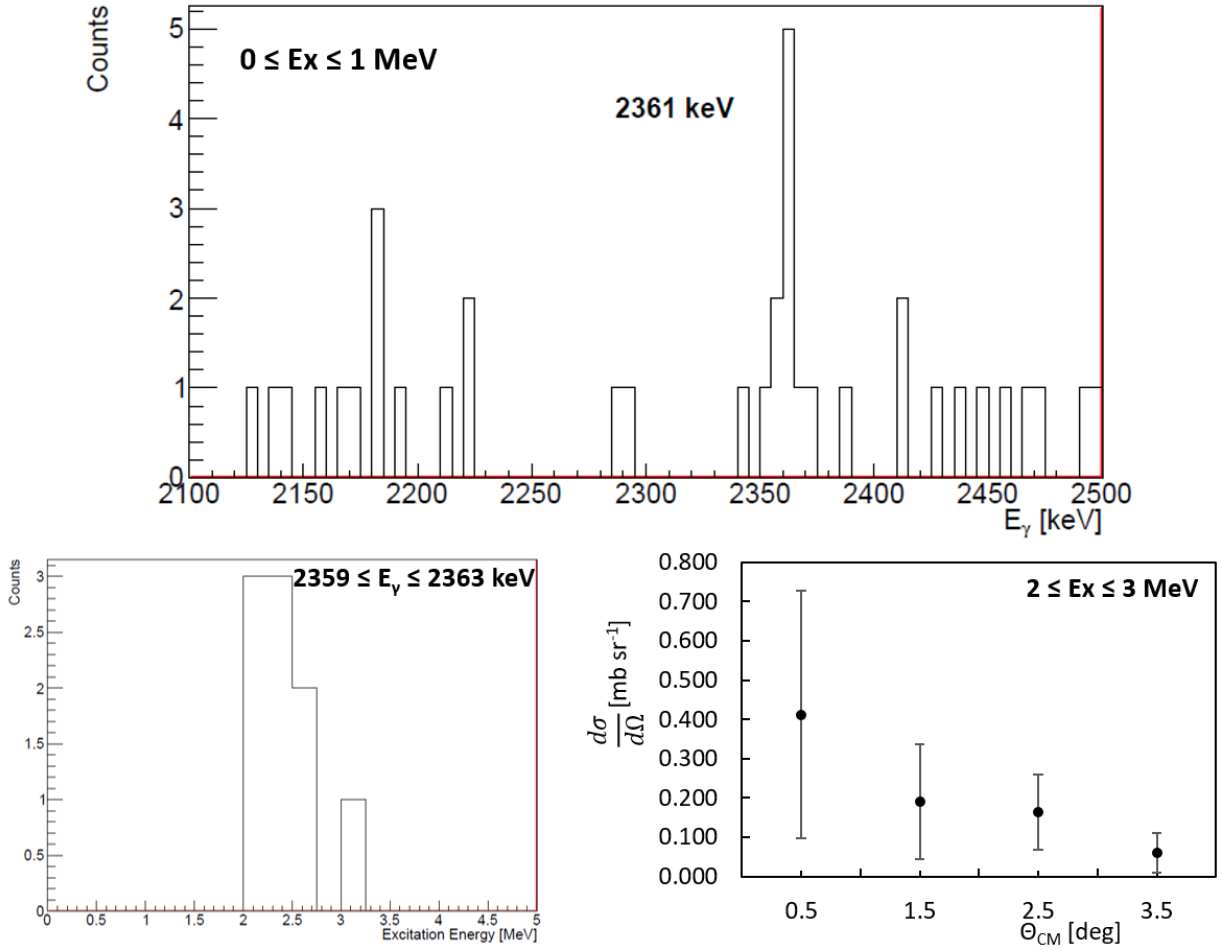

Figure 4.41: $E_\gamma = 2361$ keV. A gate on E_γ was made from 2359 keV to 2363 keV. One peak appeared in the resulting gated excitation energy spectrum. For the peak at approximately $E_x = 2.3$ MeV, a gate was made from 2 MeV to 3 MeV and the angular distribution found in the bottom right of the figure was extracted. Because the angular distribution appears to peak at forward angles, a further MDA was performed on this angular distribution.

corresponding angular distributions that could have a $\Delta L = 0$ contribution: 1753 keV and 2361 keV.

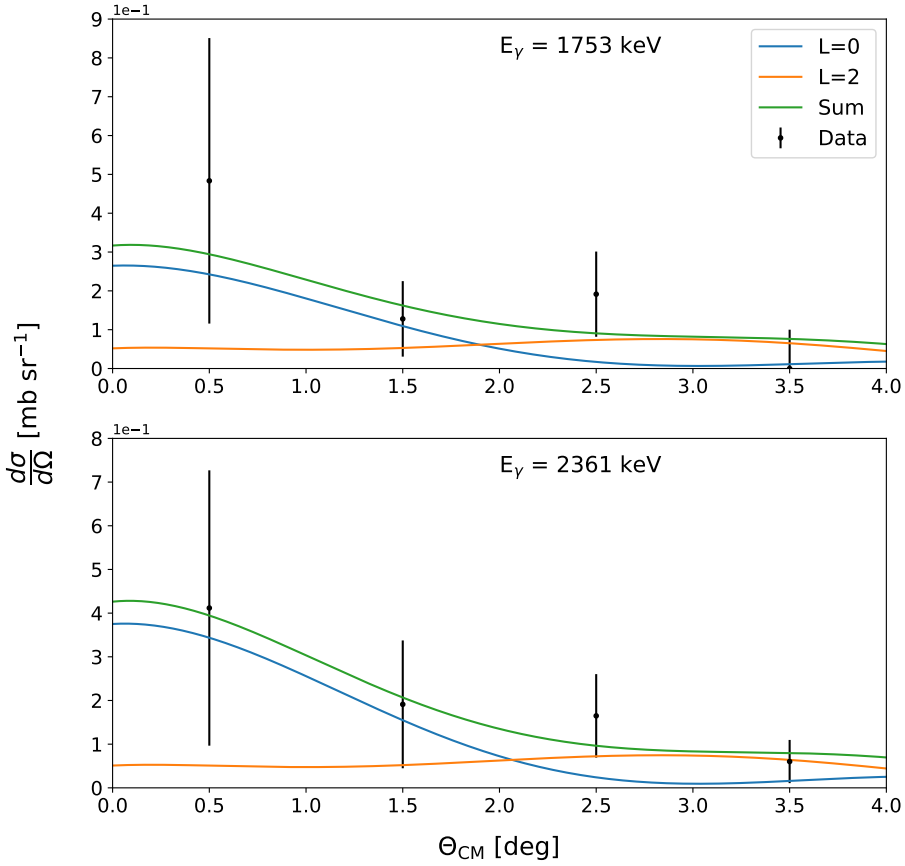

Figure 4.42: Multipole decomposition analysis results for the γ-gated angular distributions. Because of the reduced number of experimental data points, only the $\Delta L = 0$ (yellow) and $\Delta L = 2$ (green) were used in the fitting procedure. The small contributions of the monopole in these fits provide a stricter upper limit on the ^{86}Kr strength compared to the result presented in figure 4.30.

An MDA was performed on the angular distributions associated with the 1753 keV and 2361 keV lines, the results of which are shown in figure 4.42. Both cases showed a small $\Delta L = 0$ component, although, as with the case of the singles data, the fitting parameters carried significant uncertainties, due to the large statistical uncertainties present in the data.

Using the $\Delta L = 0$ component, and the method discussed in section 4.6, the Gamow-Teller strength was extracted for each transition; these values are shown in table 4.8.

Table 4.8: Gamow-Teller strength associated with observed γ-rays from GRETINA. Due to the uncertainties associated with the measurement, these extracted values provide only an upper limit for the strength from ^{86}Kr.

E_γ	$B(GT)$
1753 keV	0.045 ± 0.043
2361 keV	0.063 ± 0.046

As with the previously presented results in this chapter, the extracted Gamow-Teller strength was weak. This γ-ray analysis presented an opportunity to verify the result from the initial singles analysis, and to further constrain the upper limit of the ^{86}Kr Gamow-Teller strength. The extracted strength distribution is an interesting result in and of itself, providing insight into the structure and behavior of ^{86}Kr, and other nuclei like it. However, further analysis and interpretation in the context of astrophysical phenomena tie these experimental results to the larger goal of understanding and improving the nuclear physics inputs for core-collapse supernova simulations.

Chapter 5

Weak-Rates

5.1 B(GT) Comparison

One of the goals of the ^{86}Kr(t,^{3}He+γ) experiment was to obtain data for validating and benchmarking theoretical models. The experimental Gamow-Teller distributions that were extracted (sections 4.6 and 4.7) are compiled in figure 5.1, with the result from the singles MDA shown as black points and the result from the γ-ray analysis shown by the green points. As noted in chapter 4, both data sets provide only upper limits for the Gamow-Teller strength of ^{86}Kr, due to significant statistical and systematic uncertainties. Also shown in figure 5.1 are two theoretical calculations to compare with the experimental results. For a better visual comparison, a plot omitting the upper limit obtained from the singles MDA is shown in figure 5.2.

Comparing the Gamow-Teller strength distribution derived from the singles data to the known ^{86}Br level scheme, it is possible to obtain draw a conclusion about the sensitivity of the ^{86}Kr experiment. Because there is no known 1^{+} state below 2.5 MeV in ^{86}Br, it is unlikely that there is Gamow-Teller strength below this energy. Because of this, it appears that a strength of 0.05 is the limit to the experimental sensitivity. Examining the rest of the singles spectrum in figure 5.1, above approximately 3.5 MeV, the extracted strength is at the 0.05 level. Again, because of the sensitivity limit, it is difficult to determine whether

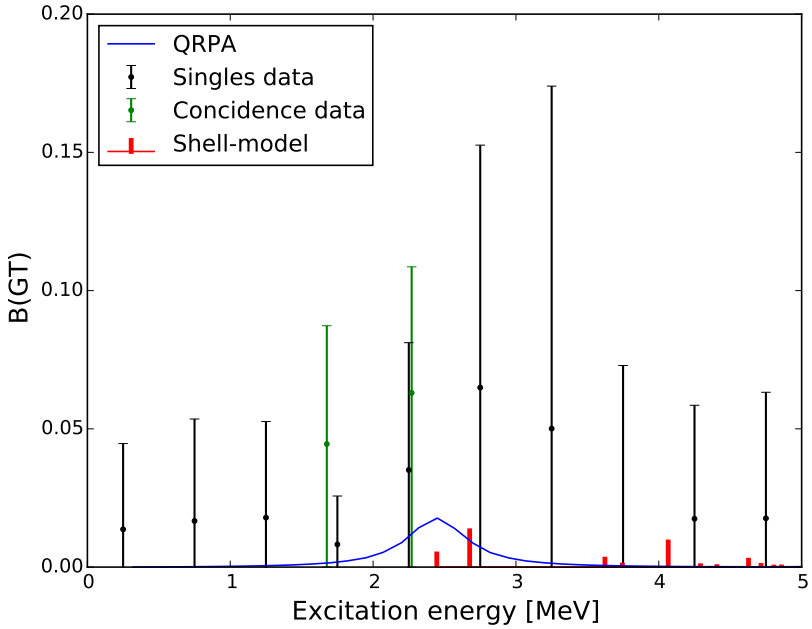

Figure 5.1: Gamow-Teller strength distribution obtained from theoretical calculations and experimental results. The black points indicate the upper limit obtained from analysis of the singles data; the green points are the upper limit from the γ-ray analysis. Also shown: a shell-model calculation (red) using the jj44pna interaction [78] and a QRPA calculation (blue) [84].

there is strength at excitation energies above 3.5 MeV.

The first theoretical calculation shown is a shell-model calculation (red) performed in NUSHELLX [79], within the SNE model space [75, 76] using the jj44pna interaction [78]. A ^{78}Ni core was assumed for the calculation, with a valence space of ($0f_{5/2}$, $1p_{3/2}$, $1p_{1/2}$, $0g_{9/2}$) for protons, and ($0g_{7/2}$, $1d_{5/2}$, $1d_{3/2}$, $2s_{1/2}$, $0h_{11/2}$) for neutrons. Because the model space was truncated, it was necessary to apply a hindrance factor to the result of the calculation. This hindrance factor, $\frac{1}{h}$, is a combination of two factors, h_{high} and $h_{\text{c.p.}}$, in the following form:

$$\frac{1}{h} = \frac{1}{h_{\text{high}}} \times \frac{1}{h_{\text{c.p.}}}. \tag{5.1}$$

h_{high} was first mentioned in section 2.2.3 and is associated with the mixing of two-particle

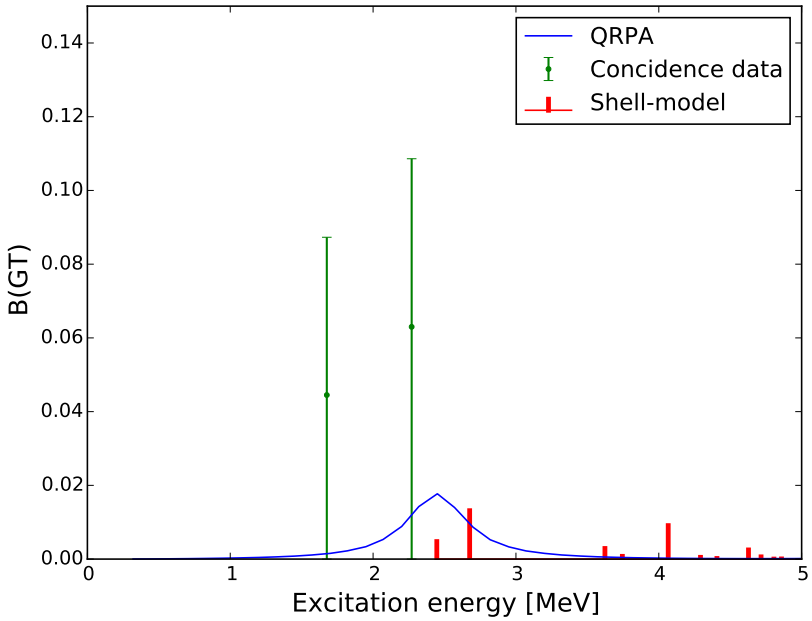

Figure 5.2: Gamow-Teller strength distribution obtained from theoretical calculations and experimental results. To better compare the theoretical models and the experimental upper limit for the strength, the result of the singles analysis is omitted here.

two-hole states with oscillator energies of $2\hbar\omega$ and greater. It is the typical scaling factor applied to calculated Gamow-Teller strength distributions and accounts for the well-known quenching of the Gamow-Teller transition strength [80, 81]. $h_{\text{c.p.}}$ takes into account the core polarization of the $0g$ orbital, describing the mixing of the $0g_{9/2}$ and $0g_{7/2}$ orbitals [140]. It is necessary to include this additional factor because of the truncation of the model space used in the shell-model calculation. With these two contributions, the total hindrance factor applied to the calculated Gamow-Teller strength distribution was 1/9.

The second calculation shown in figure 5.2 is a quasiparticle random-phase approximation (QRPA) calculation (blue). It was performed using the axially-deformed Skyrme Finite Amplitude Method (FAM) [141, 142], with the Skyrme functional and single-particle space from reference [143]. The width of the states in the QRPA calculation was set to 0.59 MeV

(FWHM). For both of the theoretical models, the first peak in the strength distribution was placed at the excitation energy of the first 1^+ state in ^{86}Br, 2.446 MeV. Therefore, it follows that both distributions peak at approximately the same excitation energy. Comparing these theoretical results to the strength extracted from the coincidence data, it is apparent that they are both within the experimental error bars, and thus, are consistent with the experimental result.

Examining the summed strength up to 5 MeV, both the shell-model calculation and the QRPA calculation yielded reasonably close results: 0.035 for the shell-model calculation and 0.024 for the QRPA calculation. The cumulative strength obtained from the coincidence data was 0.108 ± 0.063. Therefore, while the cumulative Gamow-Teller strength up to 5 MeV obtained from the theoretical models is less than the magnitude of the strength extracted from the γ-ray analysis, they still fell within the calculated experimental uncertainties.

5.2 Electron-Capture Rates

Using the Gamow-Teller strengths calculated in sections 4.6 and 4.7, as well as the theoretical calculations shown in section 5.1, it was possible to calculate electron-capture rates for a variety of stellar densities and temperatures. These calculations were performed using the ECRATES code [44, 144, 145, 146], which takes the reaction Q-value, excitation energy and Gamow-Teller strength distribution as inputs. The calculation yielded electron-capture rates for the nucleus of interest as a function of density and temperature; the grid used in this work is the same as that of the LMP table mentioned in section 2.2 [56, 69].

The results of several electron-capture rate calculations, at a temperature of 10 GK and as a function of stellar density, are shown in figure 5.3. The central temperature of a star

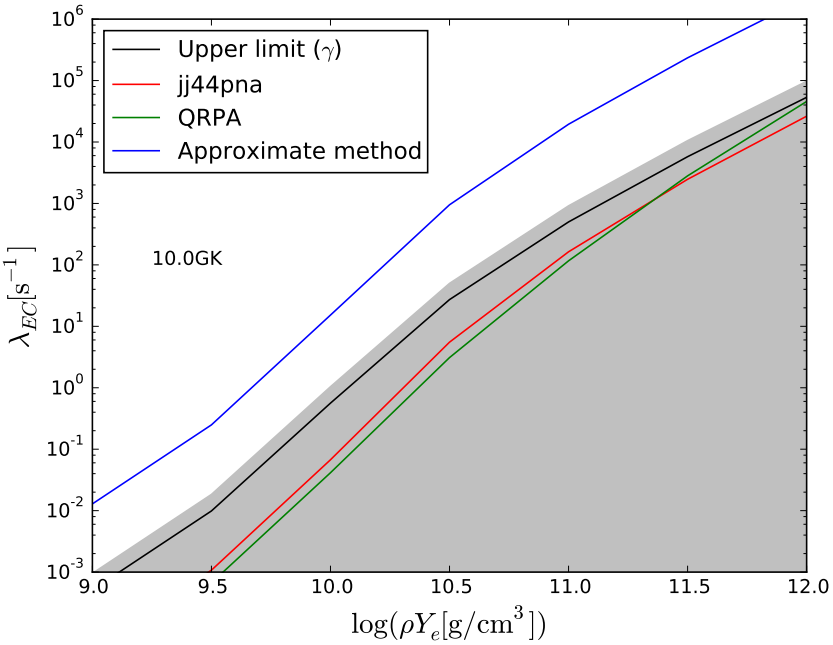

Figure 5.3: A comparison of the experimentally-determined electron-capture rates, at 10 GK over the range of stellar densities relevant for the late stages of core collapse, for ^{86}Kr and several theoretical models.

during the late stages of collapse just prior to core bounce ranges from 9 GK to 11 GK [9]; at the same time, the central density increases from 10^9 gm/cm^3 to 10^{12} gm/cm^3 during the period of deleptonization until neutrino trapping. In the figure, the black solid line and the gray shaded region represent the electron-capture rates that are associated with Gamow-Teller strength determined from the γ-ray analysis in section 4.7; this is the most stringent upper limit placed on the strength and, by extension, the electron-capture rates. Also shown are the rates determined from strength distributions from the jj44pna shell-model calculation with a ^{78}Ni core (red) [79, 78], QRPA calculation (green) [84] and the approximate method implemented in NuLib (blue) [1, 2, 47].

Both the shell-model calculation and the QRPA calculation were consistent with the experimental result, as they fell within the experimental error band for all stellar densities.

The rates obtained from the approximate method from section 2.2 were the most inaccurate, overestimating the electron-capture rates by about two orders of magnitude. Results illustrating the overestimation of electron-capture rates by the approximate method have also been shown for the case of ^{88}Sr [94]. A ^{88}Sr(t,^{3}He) experiment was performed, as part of the same experimental campaign as the ^{86}Kr experiment, and a Gamow-Teller strength distribution was extracted; the electron-capture rates calculated from the distribution were also smaller than those rates provided by the approximate method by approximately two orders of magnitude [94].

Because it is known that the approximate method accounts for the electron-capture rates for a large number of nuclei in astrophysical simulations, see figure 2.1, it is likely that it also overestimates the rates for those nuclei, particularly the ones encompassed by the high-sensitivity region. The approximate method does not account for Pauli-blocking effects, which suppress the Gamow-Teller strength of increasingly neutron-rich nuclei, leading to the rate overestimation seen in the cases of ^{88}Sr and ^{86}Kr. Conversely, in high-temperature stellar environments, low-lying states in parent nuclei can be thermally populated, and shell orbits that were previously Pauli-blocked at $T = 0$ can become partially unblocked [54], allowing electron-capture reactions to take place on these excited states [53]. These effects are also neglected in the approximate method, so that the effect of thermal unblocking and excited state transitions is uncertain. As noted in figure 2.6, including thermal unblocking and excited state transitions to the rates, as with the case of the LMSH table, can cause large variations in the electron-capture rates, as compared to the approximated rates. As such, it was necessary to perform further theoretical calculations to obtain better electron-capture rate tables for use in core-collapse supernova simulations.

The slope of the electron-capture rate curves, as a function of stellar density, are governed

by equation 2.5. For ^{86}Kr, it is clear that the electron capture rates are sensitive to changes in the density, because the electron-capture reaction Q-value is close to the Fermi energy. Such a correlation occurs due to the location of the Fermi surface in relation to states in the Gamow-Teller strength distribution. As the stellar density increases, the Fermi surface moves to higher excitation energies, and allows more Gamow-Teller transitions to be included in the electron-capture rate calculation. Therefore, small changes in the stellar density can lead to significant increases in the electron-capture rate, as is shown in the case of ^{86}Kr in figure 5.3.

As was discussed in section 2.2.3, figure 2.5 presents the Gamow-Teller strength distribution for ^{86}Kr, as obtained from the QRPA calculation discussed in section 5.1. It was shown that, with increasing stellar density, the derived electron-capture rates remained sensitive to the details of the Gamow-Teller strength distribution at higher excitation energies. Because the other nuclei in the high-sensitivity region have large, negative Q-values, similar to ^{86}Kr, it is likely that their electron-capture rates exhibit the same behavior. This is an important feature, because the highest stellar densities occur during the late stages of stellar core-collapse, when nuclei in the high-sensitivity region have the largest effect on the dynamics of the supernova [9]. Such a conclusion highlights the need for theoretical predictions of the details of the strength distribution in order to obtain high-quality electron-capture rates, as opposed to merely replicating the cumulative Gamow-Teller strength of the nucleus.

In summary, at the lower stellar densities, for nuclei in the high-sensitivity region, the details of the Gamow-Teller strength distribution at low excitation energies have a significant effect on the calculated electron-capture rates. As the stellar density increases, as shown in figure 2.5, the details of the strength distribution continue to influence the calculated rates. Such behavior is different from previous assumptions that, at high stellar densities, the

total Gamow-Teller strength becomes more important than the way in which the strength is distributed. For neutron-rich nuclei with large negative Q-values, which are important in the study of core-collapse supernovae, it has now been shown that the electron-capture rates are sensitive to both the details of the Gamow-Teller strength distribution, as well as the magnitude of the strength. Therefore, theoretical models are needed to accurately reproduce all aspects of the strength distribution for use in electron-capture rate calculations, and further studies of the high-sensitivity region.

5.3 High-Sensitivity Region Rates

Because the high-sensitivity region has been determined to have a significant effect on the behavior of the late stages of stellar core collapse [9, 10, 11], it was chosen as the target for the development of a new electron-capture rate table. In the original weak-rate library, the rates for that region were predominately obtained via the approximate method, which overestimates the electron-capture rates for heavy, neutron-rich nuclei. However, because the nuclei in this region are influential of the progression of stellar core-collapse, such inaccuracies in the rates lead to large uncertainties in the simulation. Therefore, the electron-capture rates for the 74 high-sensitivity region nuclei [10], as well as ^{86}Kr, ^{88}Sr, ^{90}Zr and ^{93}Nb, were calculated, in an attempt to obtain more accurate inputs for astrophysical simulations. The chosen nuclei are marked in dark green in figure 2.1.

The Gamow-Teller strength distributions used in the electron-capture rate calculations were obtained from QRPA calculations, which were performed in collaboration with Evan Ney from the University of North Carolina at Chapel Hill, using the same parameters as described in section 5.1 [84]. Whereas previous theoretical calculations determined the ex-

citation energy scale of the distribution based on the location of the first Gamow-Teller transition, typically obtained from experimental data, this was not possible for these calculations. Many of the nuclei lacked comprehensive information of the level structure, including excitation energy, spin and parity. Therefore, an estimate of the energy of the first Gamow-Teller transition, as well as the spin of the ground state of the daughter nucleus and the Q-value of the reaction, were obtained from a Hartree-Fock-Bogoliubov (HFB) calculation, which was performed to provide inputs to the final QRPA calculation [84]. In order to obtain the most accurate electron-capture rates, the parent spin and Q-value were set to the experimentally-determined values where they were available, and the theoretical estimates were used in the cases where no spin assignments existed.

The electron-capture rate calculations were performed following the same methods described in section 5.2, using the ECRATES code [44, 144, 145, 146], and then were compiled into a single table to be added to the weak-rate library [71]. Finally, to determine the effect of these rates on the late stages of core-collapse, a new simulation was performed with the addition of the updated rates. This simulation was run using the NuLib [72] and GR1D codes [72, 73] with the same parameters described in section 2.3. The resulting lepton fraction from this simulation is shown in figure 5.4.

The dashed black line shows the status of the weak-rate library prior to any changes in the approximate method or addition of new rates [10]; the green line shows the weak-rate library with the addition of the isospin-dependent approximate method [2] and updated pf-shell rate calculations [33]. Finally, the blue line shows the result of the simulation with the weak-rate library in its current state, with the added high-sensitivity region rate table. For comparison, there are two simulations from the original sensitivity study, discussed in section 2.3, illustrating the cases in which the electron-capture rates of the diamond-region

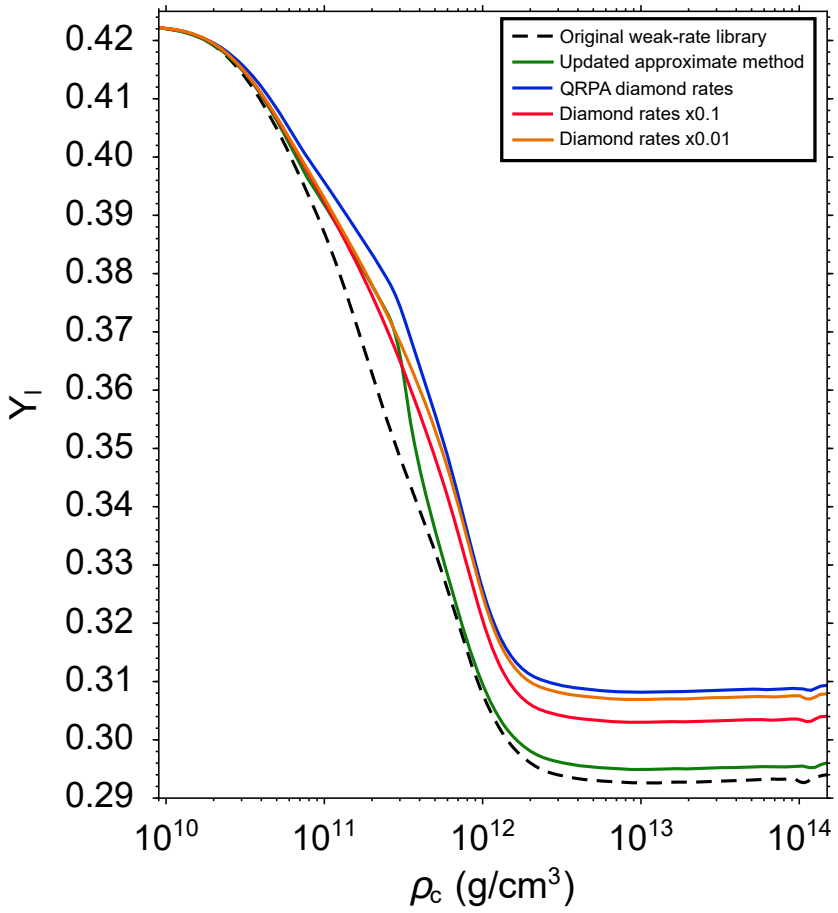

Figure 5.4: Plot of the lepton fraction versus core density during deleptonization and neutrino trapping. The results from the original weak-rate library (black dashed line), the weak-rate library with an updated approximate method (green) and the weak-rate library with the new high-sensitivity region rates (blue) are compared.

nuclei were scaled by a factor of 0.1 (red line) and by a factor of 0.01 (orange line) [10].

Introducing more accurate electron-capture rates to the simulation had a significant effect on the final lepton fraction after 10^{12} g/cm^3. Comparing the blue and green lines, the weak-rate library without the updated rates (green line) attained a final lepton fraction of 0.294, while the weak-rate library including the new rates (blue line) reached a final lepton fraction of 0.312. This constituted a 15% variation in the lepton fraction with the addition of more accurate rates for 78 nuclei. It is also possible to compare the results of the newest simulation

to the sensitivity study that motivated this work, and it is found that the final lepton fraction for this work (blue) is comparable to the case in which the rates in the diamond region were scaled by a factor of 0.01 (orange).

With the addition of the newly-calculated electron-capture rates for the high-sensitivity region nuclei, the core-collapse supernova simulation now provides a more reliable description of the dynamics of the event. Examinations of the lepton fraction during the late stages of stellar core-collapse illustrated that the electron-capture rates for these nuclei were overestimated by approximately 2 orders of magnitude, on average. By introducing a dedicated table of rates, rather than relying on the approximate method for this region, the dynamics of the simulation were changed significantly. Now, with improved nuclear physics inputs, all astrophysical simulations that rely on NuLib and the weak-rate library will yield more accurate results, leading to a better understanding of core-collapse supernovae, and astrophysical phenomena, in general.

Chapter 6

Conclusions and Outlook

The evolution of core-collapse supernovae is highly sensitive to electron-captures on medium-heavy nuclei. In the previous sensitivity study, as discussed in chapter 2, a region of neutron-rich nuclei surrounding the $N = 50$ shell-closure was found to have a significant effect on the dynamics of the late stages of stellar core-collapse [9, 11]. A set of 74 nuclei, above ^{78}Ni were chosen and their electron-capture rates were scaled in a series of simulations. It was found that, in changing the rates in the simulation by a factor of 0.1, the rates in the high-sensitivity region were responsible for half of the total variation in dynamics of the supernova, compared to the thousands of other nuclei contributing [10]. Because the method used for estimating electron-capture rates in this high-sensitivity region was thought to yield overestimated rates, it was clear that a more in-depth study of these nuclei was needed.

While it would be preferable to obtain Gamow-Teller strengths and electron-capture rates for all of these nuclei using experimental data, such as charge-exchange reaction measurements, this is not feasible because it is not time-efficient to perform high-quality experiments on a group of more than 70 nuclei. Additionally, experimental data cannot provide all of the necessary information, such as transitions from excited states [53], or thermal unblocking effects [54], which become relevant at high stellar temperatures. Instead, it is necessary to rely on theoretical models to provide accurate Gamow-Teller strength distributions for use in electron-capture rate calculations.

These theoretical calculations must be validated and benchmarked by experimental data to ensure the models provide accurate rates that can be used in the astrophysical simulations. Experiments also guide theory development, finding those models in need of improvement. An experimental campaign was performed on nuclei lying near the high-sensitivity region, including ^{86}Kr, which was studied with the (t,^{3}He+γ) reaction. This nucleus was chosen because it is the most neutron-rich stable nucleus on the $N = 50$ shell closure, and is as close to the high-sensitivity region for core-collapse supernovae as can be studied with current experimental facilities. The ^{86}Kr experiment was challenging because of the use of a gas target, which introduced target window events into all of the data sets. In order extract the signal of interest, a careful background subtraction was performed, introducing significant systematic uncertainties into the calculated ^{86}Kr(t,^{3}He) cross section.

Using both the multipole decomposition analysis on the singles data and an analysis of the measured γ-rays, an upper limit for the Gamow-Teller strength was extracted for ^{86}Kr up to an excitation energy of 5 MeV. In the analysis of the coincidence data, γ-rays associated with the two known 1^+ states in ^{86}Br were not observed, leading to a broader search for Gamow-Teller transitions. To that end, several new γ-lines were identified in ^{86}Br, two of which were found to potentially have some Gamow-Teller strength associated with them. For both the singles and coincidence data, the systematic and statistical uncertainties present in the extraction of the strength distribution yielded a Gamow-Teller strength that was consistent with zero.

The experimental data analyzed in this work provided new information about the Gamow-Teller strength of ^{86}Kr, indicating that it is heavily suppressed due to Pauli-blocking in the nucleus. Such a conclusion translated to electron-capture rates that were different from those rates originally used in the core-collapse supernova simulation. The simulations were

performed using inputs from the weak-rate library, which includes a number of weak-rate tables covering the valley of stability and lighter-mass nuclei. For neutron-rich, heavy nuclei, the weak-rate library uses an approximate method for calculating the weak rates, assuming a single Gamow-Teller peak instead of a strength distribution. It was shown, in previous sensitivity studies, that this approximation likely overestimates the electron-capture rates for neutron-rich, heavy nuclei, and the experimental results from the ^{86}Kr experiment confirmed an overestimation of the rates by approximately two orders of magnitude.

Because of this result, it was clear that different theoretical models were needed to obtain more accurate electron-capture rates. For this, shell-model and QRPA calculations were performed, and the subsequent Gamow-Teller strength distributions were used to derive sets of electron-capture rates. Comparing the ^{86}Kr experimental results to the theoretical calculations indicated that both models were consistent with the electron-capture rates for the range of densities relevant to the late stages of stellar core-collapse, within the experimental uncertainties. Validating theoretical models against the experimental data opened the way to performing calculations for additional nuclei, and yielding more accurate electron-capture rates for a larger section of the chart of nuclides.

Using the QRPA method, the Gamow-Teller strength distributions and electron-capture rates were calculated for the 74 nuclei in the high-sensitivity region, as well as for ^{86}Kr, ^{88}Sr, ^{90}Zr and ^{93}Nb [84]. Compiling all of the rates into a single rate table, they were added to the weak-rate library [71] and NuLib [72], to take the place of the approximated rates. The intention of this final step was to provide more accurate nuclear physics inputs to the astrophysical simulation, both to observe the effect on the dynamics of the supernova, and to determine the extent to which the electron-capture rates in this region were changed with the new calculations. A new core-collapse supernova simulation was performed using

GR1D [72, 73], incorporating the new rate table and other updates to the weak-rate library. The results of the simulation indicated that the electron-capture rates in the high-sensitivity region were, on average, overestimated by about two orders of magnitude, which parallels the results of the ^{86}Kr experiment.

As a result of these findings, it is clear that it is important to continually develop better theoretical models for the more exotic and heavier mass regions of the chart of nuclides. Then, electron-capture rates with increased reliability will become available for use in astrophysical simulations, yielding a more accurate picture of the behavior of core-collapse supernovae, and other cataclysmic phenomena. In the era of multi-messenger astronomy, measurements of neutrino signals and gravitational waves are combined in order to obtain a more complete understanding of the astrophysical event. However, it is known that variations in electron-capture rates, especially in the high-sensitivity region, can lead to large uncertainties in the expected neutrino luminosity [9] or gravitational wave frequency [29, 30]. Therefore, it is imperative that astrophysical simulations be as accurate as possible, in order to guide and inform observations of real astronomical events.

Charge-exchange experiments at intermediate energies will continue to be influential in the development process, benchmarking theoretical models and providing insight into regions of the chart of nuclides that require further study. Experimental campaigns at the Facility for Rare Isotope Beams (FRIB) will allow charge-exchange experiments to probe heavier and more exotic nuclei with improved statistics. Performing experiments in inverse kinematics will also be important to reach more nuclei that are of astrophysical interest. New experimental methods, such as (d,^{2}He) reaction in inverse kinematics, are being developed to use the Active Target-Time Projection Chamber (AT-TPC) [147] in conjunction with the S800 spectrometer. Although this type of experiment relies on the measurement of two protons,

this probe was chosen because alternative probes present greater experimental challenges. (t,^{3}He) experiments in inverse kinematics would require a hydrogen target with significant containment measures, which would make it difficult for the ^{3}He particle to reach the detectors. The (^{7}Li,^{7}Be) probe [148] would also not be ideal because it would not populate states with high excitation energy, making the results less useful for astrophysical purposes.

Improvement to experiments in forward kinematics could also be considered. For example, in the case of the ^{86}Kr experiment, it could be possible to re-do the measurement, but with a frozen target. This would allow the target to be thinner, with the same density, and also remove the need for a background subtraction. With these steps, the statistics for the measurement would be increased, and the systematic uncertainties would be reduced, in theory providing a cleaner measurement of the ^{86}Kr Gamow-Teller strength. Knowing the difficulties of a gas target measurement for nuclei with weak Gamow-Teller strength, future charge-exchange experiments can be improved in order to obtain higher-quality data, and yielding, in turn, more accurate electron-capture rates for use in astrophysical simulations.

The synergy between nuclear physics experiments and astrophysical observations is necessary, as discoveries in one field guide the progress of the other. Sharing improved nuclear physics inputs to astronomers provides accurate simulations that can be used as a template to which observational data can be compared. In reverse, new observational data indicates the ways in which astrophysical simulations and nuclear physics data can be improved, guiding theoretical development and future experimental studies. By collaborating across disciplines, information about avenues for further study is continually uncovered, leading to a better, and more detailed, understanding of the universe.

BIBLIOGRAPHY

BIBLIOGRAPHY

[1] K. Langanke, G. Martínez-Pinedo, J. M. Sampaio, D. J. Dean, W. R. Hix, O. E. B. Messer, A. Mezzacappa, M. Liebendörfer, H.-Th. Janka, and M. Rampp. Electron capture rates on nuclei and implications for stellar core collapse. *Phys. Rev. Lett.*, 90:241102, 2003.

[2] Ad. R. Raduta, F. Gulminelli, and M. Oertel. Stellar electron capture rates on neutron-rich nuclei and their impact on stellar core collapse. *Phys. Rev. C*, 95:025805, 2017.

[3] J. L. Fisker, V. Barnard, J. Görres, K. Langanke, G. Martínez-Pinedo, and M. C. Wiescher. Shell model based reaction rates for rp-process nuclei in the mass range A=44-63. *At. Data Nucl. Data Tables*, 79:241–292, 2001.

[4] G. Bassani, N. M. Hintz, and C. D. Kavaloski. Nuclear structure information from the (p, t) reaction, $A = 46$ to $A = 70$. *Phys. Rev.*, 136:B1006–B1022, Nov 1964.

[5] D. W. Bardayan. Transfer reactions in nuclear astrophysics. *J. Phys. G*, 43(4):043001, 2016.

[6] W. P. Alford and B. M. Spicer. *Nucleon Charge-Exchange Reactions at Intermediate Energy*, pages 1–82. Springer US, Boston, MA, 2002.

[7] F. Osterfeld. Nuclear spin and isospin excitations. *Rev. Mod. Phys.*, 64:491, 1992.

[8] M. N. Harakeh and A. van der Woude. *Giant Resonances: Fundamental High-Frequency Modes of Nuclear Excitations*. Oxford University Press, New York, 2001.

[9] C. Sullivan, E. O'Connor, R. G. T. Zegers, T. Grubb, and S. M. Austin. The sensitivity of core-collapse supernovae to nuclear electron capture. *Astrophys. J.*, 816(1):44, 2016.

[10] R. Titus, C. Sullivan, R. G. T. Zegers, B. A. Brown, and B. Gao. Impact of electron-captures on nuclei near $N = 50$ on core-collapse supernovae. *J. Phys. G*, 45(1):014004, 2018.

[11] S. Furusawa, H. Nagakura, K. Sumiyoshi, C. Kato, and S. Yamada. Dependence of weak interaction rates on nuclear composition during stellar core collapse. *Phys. Rev. C*, 95, 01 2017.

[12] R. G. T. Zegers, T. Adachi, H. Akimune, Sam M. Austin, A. M. van den Berg, B. A. Brown, Y. Fujita, M. Fujiwara, S. Galès, C. J. Guess, M. N. Harakeh, H. Hashimoto, K. Hatanaka, R. Hayami, G. W. Hitt, M. E. Howard, M. Itoh, T. Kawabata, K. Kawase,

M. Kinoshita, M. Matsubara, K. Nakanishi, S. Nakayama, S. Okumura, T. Ohta, Y. Sakemi, Y. Shimbara, Y. Shimizu, C. Scholl, C. Simenel, Y. Tameshige, A. Tamii, M. Uchida, T. Yamagata, and M. Yosoi. Extraction of weak transition strengths via the (^{3}He, t) reaction at 420 MeV. *Phys. Rev. Lett.*, 99:202501, 2007.

[13] M. E. Howard, R. G. T. Zegers, Sam M. Austin, D. Bazin, B. A. Brown, A. L. Cole, B. Davids, M. Famiano, Y. Fujita, A. Gade, D. Galaviz, G. W. Hitt, M. Matos, S. D. Reitzner, C. Samanta, L. J. Schradin, Y. Shimbara, E. E. Smith, and C. Simenel. Gamow-Teller strengths in ^{24}Na using the ^{24}Mg(t,^{3}He) reaction at 115A MeV. *Phys. Rev. C*, 78:047302, Oct 2008.

[14] D. J. Morrissey, B. M. Sherrill, M. Steiner, A. Stolz, and I. Wiedenhoever. Commissioning the A1900 projectile fragment separator. *Nucl. Instr. Meth. Phys. Res. B*, 204(Supplement C):90 – 96, 2003.

[15] G. W. Hitt, S. M. Austin, D. Bazin, A. L. Cole, J. Dietrich, A. Gade, M. E. Howard, S. D. Reitzner, B. M. Sherrill, C. Simenel, E. E. Smith, J. Stetson, A. Stolz, and R. G. T. Zegers. Development of a secondary triton beam from primary ^{16,18}O beams for (t,^{3}He) experiments at intermediate energies. *Nucl. Instr. Meth. Phys. Res. A*, 566(2):264 – 269, 2006.

[16] D. Bazin, J. A. Caggiano, B. M. Sherrill, J. Yurkon, and A. Zeller. The S800 spectrograph. *Nucl. Instr. Meth. Phys. Res. B*, 204(Supplement C):629 – 633, 2003.

[17] A. L. Cole et al. Gamow-Teller strengths and electron-capture rates for pf-shell nuclei of relevance for late stellar evolution. *Phys. Rev. C*, 86:015809, 2012.

[18] R. G. T. Zegers. Measurement of weak rates for stellar evolution via the (t,^{3}He) reaction. *Nucl. Phys. A*, 787(1):329–336, 2007. Proceedings of the Ninth International Conference on Nucleus-Nucleus Collisions.

[19] G. W. Hitt, R. G. T. Zegers, Sam M. Austin, D. Bazin, A. Gade, D. Galaviz, C. J. Guess, M. Horoi, M. E. Howard, W. D. M. Rae, Y. Shimbara, E. E. Smith, and C. Tur. Gamow-Teller transitions to ^{64}Cu measured with the ^{64}Zn(t,^{3}He) reaction. *Phys. Rev. C*, 80:014313, 2009.

[20] C. Iliadis. *Nuclear physics of stars*. Wiley-VCH, Weinheim, Germany, 2015.

[21] H.-Th. Janka, K. Langanke, A. Marek, G. Martínez-Pinedo, and B. Müller. Theory of core-collapse supernovae. *Phys. Rep.*, 442(1.6):38, 2007.

[22] I. Iben Jr. and A. Renzini. Asymptotic giant branch evolution and beyond. *Annu. Rev. Astron. Astrophys.*, 21:271–342, 1983.

[23] S. Chandrasekhar. The maximum mass of ideal white dwarfs. *Astrophys. J.*, 74:81, 1931.

[24] H. A. Bethe. Supernova mechanisms. *Rev. Mod. Phys.*, 62:801–866, Oct 1990.

[25] W. D. Arnett. Neutrino trapping during gravitational collapse of stars. *Astrophys. J.*, 218:815–833, 1977.

[26] W. R. Hix, O. E. B. Messer, A. Mezzacappa, M. Liebendörfer, J. Sampaio, K. Langanke, D. J. Dean, and G. Martínez-Pinedo. Consequences of nuclear electron capture in core collapse supernovae. *Phys. Rev. Lett.*, 91:201102, 2003.

[27] C. D. Ott, E. P. O'Connor, S. Gossan, E. Abdikamalov, U. C. T. Gamma, and S. Drasco. Core-collapse supernovae, neutrinos, and gravitational waves. *Nuc. Phys. B - Proceedings Supplements*, 235-236:381 – 387, 2013. The XXV International Conference on Neutrino Physics and Astrophysics.

[28] S. M. Couch and C. D. Ott. Revival of the stalled core-collapse supernova shock triggered by precollapse asphericity in the progenitor star. *The Astrophysical Journal Letters*, 778(1):L7, 2013.

[29] H. Dimmelmeier, C. D. Ott, A. Marek, and H.-T. Janka. Gravitational wave burst signal from core collapse of rotating stars. *Phys. Rev. D*, 78:064056, Sep 2008.

[30] S. Richers, C. D. Ott, E. Abdikamalov, E. O'Connor, and C. Sullivan. Equation of state effects on gravitational waves from rotating core collapse. *Phys. Rev. D*, 95:063019, 2017.

[31] K. Nakamura, S. Horiuchi, M. Tanaka, K. Hayama, T. Takiwaki, and K. Kotake. Multimessenger signals of long-term core-collapse supernova simulations: synergetic observation strategies. *Mon. Notices Royal Astron. Soc.*, 461(3):3296–3313, 2016.

[32] G. Martínez-Pinedo, Y. H. Lam, K. Langanke, R. G. T. Zegers, and C. Sullivan. Astrophysical weak-interaction rates for selected A= 20 and A= 24 nuclei. *Phys. Rev. C*, 89:045806, 2014.

[33] T. Suzuki, H. Toki, and K. Nomoto. Electron-capture and β-decay rates for *sd*-shell nuclei in stellar environments relevant to high-density O-Ne-Mg cores. *Astrophys. J.*, 817:163, 2016.

[34] A. Heger, K. Langanke, G. Martínez-Pinedo, and S. E. Woosley. Presupernova evolution with improved rates weak-interaction. *Astrophys. J.*, 560:307, 2001.

[35] A. Heger, K. Langanke, G. Martínez-Pinedo, and S. E. Woosley. Presupernova collapse models with improved weak-interaction rates. *Phys. Rev. Lett.*, 86:1678, 2001.

[36] H. A. Bethe, G. E. Brown, J. Applegate, and J. M. Lattimer. Equation of state in the gravitational collapse of stars. *Nucl. Phys. A*, 324(2):487, 1979.

[37] F. Brachwitz et al. The role of electron captures in Chandrasekhar-mass models for type Ia supernovae. *Astrophys. J.*, 536:934, 2000.

[38] K. Iwamoto, F. Brachwitz, K. Nomoto, N. Kishimoto, H. Umeda, W. R. Hix, and F. Thielemann. Nucleosynthesis in Chandrasekhar mass models for type Ia supernovae and constraints on progenitor systems and burning-front propagation. *Astrophys. J. Supp.*, 125:439, 1999.

[39] K. Mori, M. A. Famiano, T. Kajino, T. Suzuki, J. Hidaka, M. Honma, K. Iwamoto, K. Nomoto, and T. Otsuka. Impact of Gamow-Teller strengths on explosive type Ia supernovae nucleosynthesis. *Astrophys. J.*, 833:179, 2016.

[40] R. G. T. Zegers, E. F. Brown, H. Akimune, Sam M. Austin, A. M. van den Berg, B. A. Brown, D. A. Chamulak, Y. Fujita, M. Fujiwara, S. Galès, M. N. Harakeh, H. Hashimoto, R. Hayami, G. W. Hitt, M. Itoh, T. Kawabata, K. Kawase, M. Kinoshita, K. Nakanishi, S. Nakayama, S. Okumura, Y. Shimbara, M. Uchida, H. Ueno, T. Yamagata, and M. Yosoi. Gamow-Teller strength for the analog transitions to the first $t = 1/2, J^\pi = 3/2^-$ states in ^{13}C and ^{13}N and the implications for type Ia supernovae. *Phys. Rev. C*, 77:024307, 2008.

[41] S. Gupta, E. F. Brown, H. Schatz, P. Möller, and K. Kratz. Heating in the accreted neutron star ocean: Implications for superburst ignition. *Astrophys. J.*, 662:1188, 2007.

[42] H. Schatz et al. *Nature*, 505:12757, 2013.

[43] S. Goriely, A. Bauswein, O. Just, E. Pllumbi, and H.-Th. Janka. Impact of weak interactions of free nucleons on the r-process in dynamical ejecta from neutron star mergers. *Monthly Notices of the Royal Astronomical Society*, 452(4):3894, 2015.

[44] G. M. Fuller, W. A. Fowler, and M. J. Newman. *Astrophys. J.*, 42:447, 1980.

[45] G. M. Fuller, W. A. Fowler, and M. J. Newman. *Astrophys. J.*, 252:715, 1982.

[46] G. M. Fuller, W. A. Fowler, and M. J. Newman. *Astrophys. J.*, 48:279, 1982.

[47] G. M. Fuller, W. A. Fowler, and M. J. Newman. *Astrophys. J.*, 293:1, 1985.

[48] S. Noji, R. G. T. Zegers, Sam M. Austin, T. Baugher, D. Bazin, B. A. Brown, C. M. Campbell, A. L. Cole, H. J. Doster, A. Gade, C. J. Guess, S. Gupta, G. W. Hitt, C. Langer, S. Lipschutz, E. Lunderberg, R. Meharchand, Z. Meisel, G. Perdikakis, J. Pereira, F. Recchia, H. Schatz, M. Scott, S. R. Stroberg, C. Sullivan, L. Valdez, C. Walz, D. Weisshaar, S. J. Williams, and K. Wimmer. β^+ Gamow-Teller transition

strengths from ^{46}Ti and stellar electron-capture rates. *Phys. Rev. Lett.*, 112:252501, 2014.

[49] S. Noji, R. G. T. Zegers, Sam M. Austin, T. Baugher, D. Bazin, B. A. Brown, C. M. Campbell, A. L. Cole, H. J. Doster, A. Gade, C. J. Guess, S. Gupta, G. W. Hitt, C. Langer, S. Lipschutz, E. Lunderberg, R. Meharchand, Z. Meisel, G. Perdikakis, J. Pereira, F. Recchia, H. Schatz, M. Scott, S. R. Stroberg, C. Sullivan, L. Valdez, C. Walz, D. Weisshaar, S. J. Williams, and K. Wimmer. Gamow-Teller transitions to ^{45}Ca via the ^{45}Sc(t,^{3}He + γ) reaction at 115 MeV/u and its application to stellar electron-capture rates. *Phys. Rev. C*, 92:024312, 2015.

[50] M. Scott, Y. Shimbara, Sam M. Austin, D. Bazin, B. A. Brown, J. M. Deaven, Y. Fujita, C. J. Guess, S. Gupta, G. W. Hitt, D. Koeppe, R. Meharchand, M. Nagashima, G. Perdikakis, A. Prinke, M. Sasano, C. Sullivan, L. Valdez, and R. G. T. Zegers. Gamow-Teller transition strengths from ^{56}Fe extracted from the ^{56}Fe(t,^{3}He) reaction. *Phys. Rev. C*, 90:025801, 2014.

[51] T. N. Taddeucci, C. A. Goulding, T. A. Carey, R. C. Byrd, C. D. Goodman, C. Gaarde, J. Larsen, D. Horen, J. Rapaport, and E. Sugarbaker. The (p, n) reaction as a probe of beta decay strength. *Nucl. Phys. A*, 469(1):125, 1987.

[52] R. G. T. Zegers, H. Akimune, Sam M. Austin, D. Bazin, A. M.van den Berg, G. P. A. Berg, B. A. Brown, J. Brown, A. L. Cole, I. Daito, Y. Fujita, M. Fujiwara, S. Galès, M. N. Harakeh, H. Hashimoto, R. Hayami, G. W. Hitt, M. E. Howard, M. Itoh, J. Jänecke, T. Kawabata, K. Kawase, M. Kinoshita, T. Nakamura, K. Nakanishi, S. Nakayama, S. Okumura, W. A. Richter, D. A. Roberts, B. M. Sherrill, Y. Shimbara, M. Steiner, M. Uchida, H. Ueno, T. Yamagata, and M. Yosoi. The (t,^{3}He) and (^{3}He, t) reactions as probes of Gamow-Teller strength. *Phys. Rev. C*, 74:024309, 2006.

[53] K. Langanke and G. Martínez-Pinedo. Shell-model calculations of stellar weak interaction rates: II. weak rates for nuclei in the mass range A= 45 − 65 in supernovae environments. *Nucl. Phys. A*, 673(1):481, 2000.

[54] K. Langanke, E. Kolbe, and D. J. Dean. Unblocking of the Gamow-Teller strength in stellar electron capture on neutron-rich germanium isotopes. *Phys. Rev. C*, 63:032801, 2001.

[55] T. Oda, M. Hino, K. Muto, M. Takahara, and K. Sato. Rate tables for the weak processes of *sd*-shell nuclei in stellar matter. *At. Data Nucl. Data Tables*, 56(2):231, 1994.

[56] K. Langanke and G. Martínez-Pinedo. *At. Data Nucl. Data Tables*, 79:146, 2001.

[57] A. Poves, J. Sánchez-Solano, E. Caurier, and F. Nowacki. Shell model study of the isobaric chains A = 50, A = 51 and A = 52. *Nucl. Phys.*, A694:157, 2001.

[58] M. Honma, T. Otsuka, B. A. Brown, and T. Mizusaki. Effective interaction for pf-shell nuclei. *Phys. Rev. C*, 65:061301(R), 2002.

[59] M. Honma, T. Otsuka, B. A. Brown, and T. Mizusaki. New effective interaction for pf-shell nuclei and its implications for the stability of the N=Z= 28 closed core. *Phys. Rev. C*, 69:034335, 2004.

[60] M. Honma, T. Otsuka, B. A. Brown, and T. Mizusaki. Shell-model description of neutron-rich pf-shell nuclei with a new effective interaction GXPF1. *Eur. Phys. J. A*, 25:299, 2005.

[61] A. Juodagalvis and D. J. Dean. Gamow-Teller gt_+ distributions in nuclei with mass A= $90 - 97$. *Phys. Rev. C*, 72:024306, 2005.

[62] P. Möller, J. R. Nix, W. D. Myers, and W. J. Swiatecki. *At. Data Nucl. Data Tables*, 59:185, 1995.

[63] J.-U. Nabi and H. V. Klapdor-Kleingrothaus. *At. Data Nucl. Data Tables*, 88:237, 2004.

[64] N. Paar, G. Colò, E. Khan, and D. Vretenar. Calculation of stellar electron-capture cross sections on nuclei based on microscopic Skyrme functionals. *Phys. Rev. C*, 80:055801, 2009.

[65] A. A. Dzhioev, A. I. Vdovin, V. Yu. Ponomarev, J. Wambach, K. Langanke, and G. Martínez-Pinedo. Gamow-Teller strength distributions at finite temperatures and electron capture in stellar environments. *Phys. Rev. C*, 81:015804, 2010.

[66] Y. F. Niu, N. Paar, D. Vretenar, and J. Meng. Stellar electron-capture rates calculated with the finite-temperature relativistic random-phase approximation. *Phys. Rev. C*, 83:045807, 2011.

[67] D. J. Dean, K. Langanke, L. Chatterjee, P. B. Radha, and M. R. Strayer. Electron capture on iron group nuclei. *Phys. Rev. C*, 58:536, 1998.

[68] A. Juodagalvis, K. Langanke, W.R. Hix, G. Martínez-Pinedo, and J.M. Sampaio. Improved estimate of electron capture rates on nuclei during stellar core collapse. *Nucl. Phys. A*, 848(3):454, 2010.

[69] K. Langanke and G. Martínez-Pinedo. Nuclear weak-interaction processes in stars. *Rev. Mod. Phys.*, 75:819, 2003.

[70] J. Pruet and G. M. Fuller. Estimates of stellar weak interaction rates for nuclei in the mass range A = 65-80. *Astrophys. J. Supp.*, 149(1):189, 2003.

[71] C. Sullivan. weakrates: Weak-rate library (ApJ release). *Zenodo*, 2015. http://OPTdoi.org/10.5281/zenodo.33788.

[72] E. O'Connor. An open-source neutrino radiation hydrodynamics code for core-collapse supernovae. *Astrophys. J. Supp.*, 219(2):24, 2015.

[73] E. O'Connor and C. D. Ott. A new open-source code for spherically symmetric stellar collapse to neutron stars and black holes. *Classical and Quantum Gravity*, 27(11):114103, 2010.

[74] A. Holt, T. Engeland, M. Hjorth-Jensen, and E. Osnes. Application of realistic effective interactions to the structure of the Zr isotopes. *Phys. Rev. C*, 61:064318, 2000.

[75] M. Lipoglavšek, C. Baktash, M. P. Carpenter, D. J. Dean, T. Engeland, C. Fahlander, M. Hjorth-Jensen, R. V. F. Janssens, A. Likar, J. Nyberg, E. Osnes, S. D. Paul, A. Piechaczek, D. C. Radford, D. Rudolph, D. Seweryniak, D. G. Sarantites, M. Vencelj, and C.-H. Yu. ^{100}Sn core excitations in ^{102}In. *Phys. Rev. C*, 65:021302, 2002.

[76] B. A. Brown and K. Rykaczewski. Gamow-Teller strength in the region of ^{100}Sn. *Phys. Rev. C*, 50:R2270, 1994.

[77] M. H. Macfarlane. Gamow-Teller sum rules and ground-state correlations. *Phys. Lett. B*, 182(3):265, 1986.

[78] A. F. Lisetskiy, B. A. Brown, M. Horoi, and H. Grawe. New $t = 1$ effective interactions for the $f_{5/2}\ p_{3/2}\ p_{1/2}\ g_{9/2}$ model space: Implications for valence-mirror symmetry and seniority isomers. *Phys. Rev. C*, 70:044314, Oct 2004.

[79] B. A. Brown, W. D. M. Rae, E. McDonald, and M. Horoi. "NuShellX@MSU". NSCL Report No. MSUCL-1289-2004., 2004.

[80] C. Gaarde et al. *Nucl. Phys.*, A369:258, 1981.

[81] C. Gaarde. In R. A. Broglia, G. B. Hagemann, and B. Herskind, editors, *Proc. Niels Bohr Centennial Conference on Nuclear Structure, Copenhagen*, page 449c. North-Holland, Amsterdam, 1985.

[82] B. A. Brown and B. H. Wildenthal. *Annu. Rev. Nucl. Part. Sci.*, 38:29, 1988.

[83] G. Martínez-Pinedo, A. Poves, E. Caurier, and A. P. Zuker. Effective g_A in the pf shell. *Phys. Rev. C*, 53:R2602, 1996.

[84] E. Ney. Private communication.

[85] A. Juodagalvis, J. M. Sampaio, K. Langanke, and W. R. Hix. Extended pool of electron-capture rates for core-collapse supernovae simulations. *J. Phys. G*, 35(1):014031, 2008.

[86] S. E. Woosley and T. A. Weaver. *Ap. J. S*, 101:181, 1995.

[87] A. W. Steiner, M. Hempel, and T. Fischer. Core-collapse supernova equations of state based on neutron star observations. *Astrophys. J.*, 774(1):17, 2013.

[88] M. Hempel and J. Schaffner-Bielich. A statistical model for a complete supernova equation of state. *Nucl. Phys. A*, 837(3):210, 2010.

[89] H. Dohmann, C. Bäumer, D. Frekers, E.-W. Grewe, M. N. Harakeh, S. Hollstein, H. Johansson, L. Popescu, S. Rakers, D. Savran, H. Simon, J. H. Thies, A. M. van den Berg, H. J. Wörtche, and A. Zilges. The $(d, {}^2\mathrm{He})$ reaction on ^{96}Mo and the double-β decay matrix elements for ^{96}Zr. *Phys. Rev. C*, 78:041602, 2008.

[90] K. J. Raywood et al. *Phys. Rev. C*, 41:2836, 1990.

[91] H. Sakai and K. Sato. *Nucl. Phys.*, A731:105, 2004.

[92] K. Yako et al. *Phys. Lett.*, B615:193, 2005.

[93] K. Miki, R. G. T. Zegers, Sam M. Austin, D. Bazin, B. A. Brown, A. C. Dombos, R. K. Grzywacz, M. N. Harakeh, E. Kwan, S. N. Liddick, S. Lipschutz, E. Litvinova, M. Madurga, M. T. Mustonen, W. J. Ong, S. V. Paulauskas, G. Perdikakis, J. Pereira, W. A. Peters, C. Robin, M. Scott, A. Spyrou, C. Sullivan, and R. Titus. Isovector excitations in ^{100}Nb and their decays by neutron emission studied via the reaction at 115 MeV/u. *Phys. Lett. B*, 769:339, 2017.

[94] J. C. Zamora, R. G. T. Zegers, S. M. Austin, D. Bazin, B. A. Brown, P. Bender, H. L. Crawford, J. Engel, A. Falduto, A. Gade, P. Gastis, B. Gao, T. Ginter, C. J. Guess, S. Lipschutz, B. Longfellow, A. O. Macchiavelli, K. Miki, E. Ney, S. Noji, J. Pereira, J. Schmitt, C. Sullivan, R. Titus, and D. Weisshaar. Experimental constraint on stellar electron-capture rates from the ^{88}Sr$(t,{}^3\mathrm{He}{+}\gamma)^{88}$Rb reaction at 115 MeV/$u$. *Phys. Rev. C*, submitted.

[95] B. Gao et al. in preparation.

[96] K. Ikeda, S. Fujii, and J.I. Fujita. The (p, n) reactions and beta decays. *Phys. Lett.*, 3(6):271, 1963.

[97] B. D. Anderson, N. Tamimi, A. R. Baldwin, M. Elaasar, R. Madey, D. M. Manley, M. Mostajabodda'vati, J. W. Watson, W. M. Zhang, and C. C. Foster. Gamow-Teller

strength in the (p, n) reaction at 136 MeV on ^{20}Ne, ^{24}Mg, and ^{28}Si. *Phys. Rev. C*, 43:50–58, Jan 1991.

[98] C. J. Guess. *The $^{150}Sm(t,^3He)^{150}Pm^*$ and $^{150}Nd(^3He,t)^{150}Pm^*$ Reaction and Applications for 2ν and 0ν Double Beta Decay.* PhD thesis, Michigan State University, 2010.

[99] R. G. T. Zegers, B. A. Brown, G. Colò, H. Sakai, and M. Sasano. The response of nuclei in charge-exchange reactions. unpublished, 2017.

[100] P. F. A. Klinkenberg. Tables of nuclear shell structure. *Rev. Mod. Phys.*, 24:63–73, 1952.

[101] K. Sieja, F. Nowacki, K. Langanke, and G. Martínez-Pinedo. Shell model description of zirconium isotopes. *Phys. Rev. C*, 79:064310, Jun 2009.

[102] J. Cook and J. A. Carr. computer program FOLD, florida state university (unpublished). based on F. Petrovich and D. Stanley, Nucl. Phys. A275, 487 (1977), modified as described in J. Cook et al., Phys. Rev. C 30, 1538 (1984) and R. G. T. Zegers, S. Fracasso and G. Colò (2006), unpublished.

[103] F. Petrovich and D. Stanley. Microscopic interpretation of ^{7}Li+^{24}Mg inelastic scattering at 34 MeV. *Nucl. Phys. A*, 275(2):487 – 508, 1977.

[104] V. A. Madsen. A formalism for direct inelastic scattering and charge exchange. *Nucl. Phys.*, 80(1):177 – 197, 1966.

[105] R. G. T. Zegers. *Search for isovector giant monopole resonances.* PhD thesis, University of Groningen, 1972.

[106] W. G. Love and M. A. Franey. Effective nucleon-nucleon interaction for scattering at intermediate energies. *Phys. Rev. C*, 24:1073, 1981.

[107] M. A. Franey and W. G. Love. Nucleon-nucleon t-matrix interaction for scattering at intermediate energies. *Phys. Rev. C*, 31:488, 1985.

[108] W. G. Love, K. Nakayama, and M. A. Franey. Isovector couplings for nucleon charge-exchange reactions at intermediate energies. *Phys. Rev. Lett.*, 59:1401–1404, Sep 1987.

[109] R. G. T. Zegers, H. Akimune, S. M. Austin, D. Bazin, A. M.van den Berg, G. P. A. Berg, B. A. Brown, J. Brown, A. L. Cole, I. Daito, Y. Fujita, M. Fujiwara, S. Galès, M. N. Harakeh, H. Hashimoto, R. Hayami, G. W. Hitt, M. E. Howard, M. Itoh, J. Jänecke, T. Kawabata, K. Kawase, M. Kinoshita, T. Nakamura, K. Nakanishi, S. Nakayama, S. Okumura, W. A. Richter, D. A. Roberts, B. M. Sherrill, Y. Shimbara, M. Steiner,

M. Uchida, H. Ueno, T. Yamagata, and M. Yosoi. The (t,^{3}He) and (^{3}He, t) reactions as probes of Gamow-Teller strength. *Phys. Rev. C*, 74:024309, 2006.

[110] T. Udagawa, A. Schulte, and F. Osterfeld. Antisymmetric distorted wave impulse approximation calculations for composite particle scattering. *Nucl. Phys. A*, 474(1):131, 1987.

[111] F. Petrovich, H. McManus, V. A. Madsen, and J. Atkinson. Finite-nucleus g matrix in the microscopic description of inelastic proton scattering. *Phys. Rev. Lett.*, 22:895–899, Apr 1969.

[112] N. Willis, I. Brissaud, Y. Le Bornec, B. Tatischeff, and G. Duhamel. Elastic scattering of 217 MeV ^{3}He particles. *Nucl. Phys. A*, 204(3):454 – 464, 1973.

[113] J. Kamiya, K. Hatanaka, T. Adachi, K. Fujita, K. Hara, T. Kawabata, T. Noro, H. Sakaguchi, N. Sakamoto, Y. Sakemi, Y. Shimbara, Y. Shimizu, S. Terashima, M. Uchida, T. Wakasa, Y. Yasuda, H. P. Yoshida, and M. Yosoi. Cross section and induced polarization in ^{3}He elastic scattering at 443 MeV. *Phys. Rev. C*, 67:064612, Jun 2003.

[114] S. Y. van Der Werf, S. Brandenburg, P. Grasduk, W. A. Sterrenburg, M. N. Harakeh, M. B. Greenfield, B. A. Brown, and M. Fujiwara. The effective ^{3}He-nucleon force in a microscopic DWBA approach to the (^{3}He, t) charge-exchange reaction. *Nucl. Phys. A*, 496(2):305 – 332, 1989.

[115] B. A. Brown, A. Etchegoyen, N. S. Godwin, W. D. M. Rae, W. A. Richter, W. E. Ormand, E. K. Warburton, J. S. Winfield, L. Zhao, and C. H. Zimmerman. The Oxford-Buenos-Aires-MSU Shell-Model Code oxbash. NSCL Report No. MSUCL-1289., 2004.

[116] G. Perdikakis, R. G. T. Zegers, S. M. Austin, D. Bazin, C. Caesar, J. M. Deaven, A. Gade, D. Galaviz, G. F. Grinyer, C. J. Guess, C. Herlitzius, G. W. Hitt, M. E. Howard, R. Meharchand, S. Noji, H. Sakai, Y. Shimbara, E. E. Smith, and C. Tur. Gamow-Teller unit cross sections for (t,^{3}He) and (^{3}He,t) reactions. *Phys. Rev. C*, 83:054614, 2011.

[117] M. Sasano, H. Sakai, K. Yako, T. Wakasa, S. Asaji, K. Fujita, Y. Fujita, M. B. Greenfield, Y. Hagihara, K. Hatanaka, T. Kawabata, H. Kuboki, Y. Maeda, H. Okamura, T. Saito, Y. Sakemi, K. Sekiguchi, Y. Shimizu, Y. Takahashi, Y. Tameshige, and A. Tamii. Gamow-Teller unit cross sections of the (p, n) reaction at 198 and 297 MeV on medium-heavy nuclei. *Phys. Rev. C*, 79:024602, 2009.

[118] E.-W. Grewe, C. Bäumer, H. Dohmann, D. Frekers, M. N. Harakeh, S. Hollstein, H. Johansson, K. Langanke, G. Martínez-Pinedo, F. Nowacki, I. Petermann, L. Popescu, S. Rakers, D. Savran, K. Sieja, H. Simon, J. H. Thies, A. M. van den Berg, H. J.

Wörtche, and A. Zilges. Studies on the double-β decay nucleus ^{64}Zn using the (d,^{2}He) reaction. *Phys. Rev. C*, 77:064303, Jun 2008.

[119] H. Fujita, Y. Fujita, G. P. A Berg, A. D. Bacher, C. C. Foster, K. Hara, K. Hatanaka, T. Kawabata, T. Noro, H. Sakaguchi, Y. Shimbara, T. Shinada, E. J. Stephenson, H. Ueno, and M. Yosoi. Realization of matching conditions for high-resolution spectrometers. *Nucl. Instr. Meth. Phys. Res. A*, 484(1):17 – 26, 2002.

[120] J. Palardy, N. Ferrante, L. Riley, and R. G. T. Zegers. The Ursinus College Liquid Hydrogen Target. In *APS Division of Nuclear Physics Meeting Abstracts*, Nov 2010.

[121] K. Miki, H. Sakai, T. Uesaka, H. Baba, C. L. Bai, G. P. A. Berg, N. Fukuda, D. Kameda, T. Kawabata, S. Kawase, T. Kubo, S. Michimasa, H. Miya, S. Noji, T. Ohnishi, S. Ota, A. Saito, Y. Sasamoto, H. Sagawa, M. Sasano, S. Shimoura, H. Takeda, H. Tokieda, K. Yako, Y. Yanagisawa, and R. G. T. Zegers. Identification of the β^+ isovector spin monopole resonance via the ^{208}Pb and ^{90}Zr(t,^{3}He) reactions at 300 MeV/u. *Phys. Rev. Lett.*, 108:262503, 2012.

[122] M. Scott. *Search for the Isovector Giant Monopole Resonance via the ^{28}Si(^{10}Be,^{10}B+γ) Reaction at 100 MeV/u.* Ph.D., Michigan State University, 2015.

[123] J. Yurkon, D. Bazin, W. Benenson, D. J. Morrissey, B. M. Sherrill, D. Swan, and R. Swanson. Focal plane detector for the S800 high-resolution spectrometer. *Nucl. Instr. Meth. Phys. Res. A*, 422(1):291 – 295, 1999.

[124] W. F. Mueller, J. A. Church, T. Glasmacher, D. Gutknecht, G. Hackman, P. G. Hansen, Z. Hu, K. L. Miller, and P. Quirin. Thirty-two-fold segmented germanium detectors to identify γ-rays from intermediate-energy exotic beams. *Nucl. Instr. Meth. Phys. Res. A*, 466(3):492 – 498, 2001.

[125] S. Paschalis, I. Y. Lee, A. O. Macchiavelli, C. M. Campbell, M. Cromaz, S. Gros, J. Pavan, J. Qian, R. M. Clark, H. L. Crawford, D. Doering, P. Fallon, C. Lionberger, T. Loew, M. Petri, T. Stezelberger, S. Zimmermann, D. C. Radford, K. Lagergren, D. Weisshaar, R. Winkler, T. Glasmacher, J. T. Anderson, and C. W. Beausang. The performance of the gamma-ray energy tracking in-beam nuclear array GRETINA. *Nucl. Instr. Meth. Phys. Res. A*, 709:44 – 55, 2013.

[126] D. Weisshaar, D. Bazin, P. C. Bender, C. M. Campbell, F. Recchia, V. Bader, T. Baugher, J. Belarge, M. P. Carpenter, H. L. Crawford, M. Cromaz, B. Elman, P. Fallon, A. Forney, A. Gade, J. Harker, N. Kobayashi, C. Langer, T. Lauritsen, I. Y. Lee, A. Lemasson, B. Longfellow, E. Lunderberg, A. O. Macchiavelli, K. Miki, S. Momiyama, S. Noji, D. C. Radford, M. Scott, J. Sethi, S. R. Stroberg, C. Sullivan, R. Titus, A. Wiens, S. Williams, K. Wimmer, and S. Zhu. The performance of the γ-ray tracking array GRETINA for γ-ray spectroscopy with fast beams of rare isotopes. *Nucl. Instr. Meth. Phys. Res. A*, 847(Supplement C):187 – 198, 2017.

[127] A. Prinke. *Searching for the Origins of Fluorine: A Measurement of the $^{19}F(t,^3He)$ Reaction.* Ph.D., Michigan State University, 2012.

[128] K. Meierbachtol, D. Bazin, and D. J. Morrissey. New CsI(Na) hodoscope array for the S800 spectrograph at NSCL. *Nucl. Instr. Meth. Phys. Res. A*, 652(1):668 – 670, 2011. Symposium on Radiation Measurements and Applications (SORMA) XII 2010.

[129] K. Makino and M. Berz. COSY INFINITY version 8. *Nucl. Instr. Meth. Phys. Res. A*, 427(1):338 – 343, 1999.

[130] O. B. Tarasov and D. Bazin. Lise++: Radioactive beam production with in-flight separators. *Nucl. Instr. Meth. Phys. Res. B*, 266(19):4657 – 4664, 2008. Proceedings of the XVth International Conference on Electromagnetic Isotope Separators and Techniques Related to their Applications.

[131] C. J. Guess, R. G. T. Zegers, B. A. Brown, Sam M. Austin, D. Bazin, C. Caesar, J. M. Deaven, G. F. Grinyer, C. Herlitzius, G. W. Hitt, S. Noji, R. Meharchand, G. Perdikakis, H. Sakai, Y. Shimbara, and C. Tur. Spectroscopy of ^{13}B via the ^{13}C(t,^{3}He) reaction at 115A MeV. *Phys. Rev. C*, 80:024305, Aug 2009.

[132] A. Negret, T. Adachi, B. R. Barrett, C. Bäumer, A. M. van den Berg, G. P. A. Berg, P. von Brentano, D. Frekers, D. De Frenne, H. Fujita, K. Fujita, Y. Fujita, E.-W. Grewe, P. Haefner, M. N. Harakeh, K. Hatanaka, K. Heyde, M. Hunyadi, E. Jacobs, and L. Zamick. Gamow-Teller strengths in the A = 14 multiplet: A challenge to the shell model. *Phys. Rev. Lett.*, 97:062502, 09 2006.

[133] J. H. Kelley, J. E. Purcell, and C. G. Sheu. Energy levels of light nuclei A=12. *Nuc. Phys. A*, 968:71 – 253, 2017.

[134] F. Ajzenberg-Selove. Energy levels of light nuclei A = 13–15. *Nuc. Phys A*, 523(1):1 – 196, 1991.

[135] D. R. Tilley, H. R. Weller, and C. M. Cheves. Energy levels of light nuclei A = 16–17. *Nuc. Phys. A*, 564(1):1 – 183, 1993.

[136] S. Y. van der Werf. Computer code normod. Unpublished.

[137] B. Bonin, N. Alamanos, B. Berthier, G. Bruge, H. Faraggi, D. Legrand, J. C. Lugol, W. Mittig, L. Papineau, A. I. Yavin, D. K. Scott, M. Levine, J. Arvieux, L. Farvacque, and M. Buenerd. Response functions of ^{58}Ni, ^{116}Sn and ^{208}Pb to the excitation of intermediate-energy α-particles. *Nucl. Phys. A*, 430(2):349 – 396, 1984.

[138] M. Ichimura, H. Sakai, and T. Wakasa. *Prog. Part. Nucl. Phys.*, 56:446, 2006.

[139] A. Negret and B. Singh. Nuclear data sheets for A = 86. *Nuclear Data Sheets*, 124:1 – 156, 2015.

[140] I. S. Towner. A mass dependence in hindrance factors for favoured Gamow-Teller transitions. *Nuc. Phys. A*, 444:402–418, 1985.

[141] P. Avogadro and T. Nakatsukasa. Finite amplitude method for the quasiparticle random-phase approximation. *Phys. Rev. C*, 84:014314, Jul 2011.

[142] M. T. Mustonen, T. Shafer, Z. Zenginerler, and J. Engel. Finite-amplitude method for charge-changing transitions in axially deformed nuclei. *Phys. Rev. C*, 90:024308, Aug 2014.

[143] M. T. Mustonen and J. Engel. Global description of β^- decay in even-even nuclei with the axially-deformed skyrme finite-amplitude method. *Phys. Rev. C*, 93:014304, Jan 2016.

[144] A. D. Becerril Reyes, S. Gupta, H. Schatz, K. Kratz, and P. Möller. Electron Capture Rates for Neutron Star Crusts. In *International Symposium on Nuclear Astrophysics - Nuclei in the Cosmos - IX*, 2006.

[145] F. X. Timmes and F. Douglas Swesty. The Accuracy, Consistency, and Speed of an Electron-Positron Equation of State Based on Table Interpolation of the Helmholtz Free Energy. *Astrophys. J. Supp.*, 126(2):501, 2000.

[146] L. Valdez. Electron-captures in supernovae. Master's thesis, Michigan State University, 2012.

[147] D. Suzuki, M. Ford, D. Bazin, W. Mittig, W.G. Lynch, T. Ahn, S. Aune, E. Galyaev, A. Fritsch, J. Gilbert, F. Montes, A. Shore, J. Yurkon, J. J. Kolata, J. Browne, A. Howard, A. L. Roberts, and X. D. Tang. Prototype AT-TPC: Toward a new generation active target time projection chamber for radioactive beam experiments. *Nucl. Instr. Meth. Phys. Res. A*, 691:39 – 54, 2012.

[148] R. G. T. Zegers, R. Meharchand, Y. Shimbara, S. M. Austin, D. Bazin, B. A. Brown, C. Aa. Diget, A. Gade, C. J. Guess, M. Hausmann, G. W. Hitt, M. E. Howard, M. King, D. Miller, S. Noji, A. Signoracci, K. Starosta, C. Tur, C. Vaman, P. Voss, D. Weisshaar, and J. Yurkon. ^{34}P(^{7}Li,^{7}Be $+ \gamma$) reaction at 100A MeV in inverse kinematics. *Phys. Rev. Lett.*, 104:212504, 2010.